Lattice Gas Models and Simulations of Epitaxial Growth

Dissertation zur Erlangung des
naturwissenschaftlichen Doktorgrades
der Bayerischen Julius-Maximilians-Universität
Würzburg

vorgelegt von

Thorsten Volkmann

aus Göttingen

Institut für Theoretische Physik und Astrophysik
Bayerische Julius-Maximilians-Universität
Würzburg

Würzburg 2004

Lattice Gas Models and Simulations of Epitaxial Growth

Dissertation zur Erlangung des
naturwissenschaftlichen Doktorgrades
der Bayerischen Julius-Maximilians-Universität
Würzburg

vorgelegt von

Thorsten Volkmann

aus Göttingen

Institut für Theoretische Physik und Astrophysik
Bayerische Julius-Maximilians-Universität
Würzburg

Würzburg 2004

Eingereicht am ....
bei der Fakultät für Physik und Astronomie

Beurteilung der Dissertation:

1. Gutachter: ....
2. Gutachter: ....

Mündliche Prüfung:

1. Prüfer: ....
2. Prüfer: ....

Tag der mündlichen
Prüfung: ....

Doktorurkunde
ausgehändigt am: ....

Zusammenfassung

Diese Doktorarbeit behandelt die Modellierung und Simulation von epitaktischem Kristallwachstum, wie es beispielsweise in der Molekularstrahlepitaxie (MBE) realisiert ist. Die Grundidee besteht darin, für die Darstellung der Kristallstruktur ein Gittergasmodell zu verwenden, bei dem Atome nur diskrete Plätze eines vordefinierten Gitters besetzen können. Die Dynamik des Kristallwachstums wird mit Hilfe kinetischer Monte Carlo (KMC) Simulationen beschrieben. Der Hauptvorteil des KMC Ansatzes besteht darin, atomistische Details des Wachstums berücksichtigen zu können, und gleichzeitig die für das Kristallwachstum relevanten Zeitskalen in der Simulation zu erreichen.

Im ersten Kapitel wird zunächst das Prinzip der MBE erläutert, wobei auf wichtige Oberflächenprozesse sowie den Einfluss experimenteller Kontrollparameter eingegangen wird. Es folgt eine Darstellung wichtiger Methoden zur theoretischen Beschreibung epitaktischen Wachstums. Anschließend werden die KMC Methode und das Gittergaskonzept detailliert erläutert. Dabei werden für den Entwurf eines konkreten Gittergasmodells relevante Aspekte diskutiert, wie zum Beispiel die *solid-on-solid* Näherung der Kristallstruktur oder die Wahl einer geeigneten Gittertopologie. Ein zentraler Bestandteil jeder KMC Simulation ist die Auswahl erlaubter Ereignisse und die Berechnung der Arrhenius-Raten thermisch aktivierter Prozesse. Hierfür sind Kenntnisse über die zugehörigen Energiebarrieren erforderlich. Wir diskutieren vereinfachende Ansätze zur Näherung der Energiebarrieren, wie die sogenannte *bond counting* Methode. Abschließend wird die Umsetzung der KMC Methode in einem effizienten Simulationsalgorithmus beschrieben. In den nachfolgenden Kapiteln werden konkrete Beispiele für die Anwendung der Gittergas- und KMC Methode besprochen.

In Kapitel 2 wird ein Gittergasmodell vorgestellt, das der Beschreibung der (001) Oberfläche von II–VI Halbleitern wie z.B. CdTe oder ZnSe dient, wobei der Schwerpunkt der Betrachtungen auf CdTe liegt. Das Modell berücksichtigt u.a. die korrekte Zinkblende-Gitterstruktur sowie die relevanten Oberflächenrekonstruktionen von Cd- und Te-terminierten Oberflächen. Wir nehmen anisotrope Wechselwirkungen zwischen nächsten und übernächsten Nachbarn an der Oberfläche an, während sich Teilchen im Inneren des Kristalls isotrop anziehen. Die anisotropen Wechselwirkungen spiegeln die bekannten Eigenschaften der Oberfläche wider, wie zum Beispiel den geringen Energieunterschied zwischen der $c(2 \times 2)$ und der (2×1) Leerstellenstruktur der Cd-terminierten Oberfläche. Ein wichtiger Bestandteil des Modells ist die Einbindung zusätzlicher Te-Atome in einem schwach gebundenen Te*-Zustand. Dessen Existenz wird gestützt durch experimentell beobachtete Te-Bedeckungen von mehr als einer Monolage bei tiefen Temperaturen und hohen Te-Flüssen. Der tatsächliche Bindungsmechanismus der Te*-Atome wurde bisher nicht geklärt. Im Modell wird im Rahmen eines mean-field Ansatzes ein Te*-Reservoir mit begrenzter Kapazität angenommen.

In Kapitel 3 wird das Gittergasmodell aus dem vorherigen Kapitel zur Simulation der Atomlagenepitaxie (ALE) von CdTe verwendet. Wir untersuchen die Selbstregulierung der ALE-Wachstumsrate und zeigen, dass das Zusammenspiel der Te*-Reservoir Besetzung mit kinetischen Effekten an der Oberfläche zu zwei verschiedenen Wachs-

tumsbereichen führt. Bei hohen Temperaturen ist die Wachstumsrate auf eine halbe Lage CdTe pro ALE-Zyklus beschränkt, während bei tiefen Temperaturen eine volle Lage pro Zyklus deponiert wird. Der Übergang zwischen beiden Bereichen findet bei einer charakteristischen Temperatur statt, die im wesentlichen nur von den verwendeten Teilchenflüssen abhängt. Sowohl die Temperaturabhängigkeit der ALE-Wachstumsrate als auch die Flussabhängigkeit der charakteristischen Übergangstemperatur stimmen qualitativ gut mit experimentellen Ergebnissen für CdTe überein. Eine Abschätzung der makroskopischen Aktivierungsenergie für die Desorption schwach gebundener Te*-Atome in unserem Modell ergibt eine semiquantitative Übereinstimmung mit experimentell beobachteten Werten. Ein quantitativer Vergleich mit experimentellen Ergebnissen sollte daher möglich sein, sobald zusätzliche Daten aus Experimenten oder ab initio Rechnungen vorliegen, die zur Anpassung des Modells verwendet werden können.

In Kapitel 4 untersuchen wir anhand eines Dreikomponentensystems die Bildung von Nanostrukturen mit alternierenden Streifen während der Submonolagen-Heteroepitaxie. Dabei sind zwei unterschiedliche Mechanismen von Interesse: Trennung der Adsorbatsorten aufgrund verschieden hoher Diffusionsbarrieren, sowie der Abbau von Verspannungen durch abwechselnde Anordnung der beteiligten Materialien. KMC Simulationen eines einfach kubischen Gittergasmodells mit schwacher Bindung zwischen unterschiedlichen Adsorbatsorten zeigen, dass die Streifenbildung allein durch kinetische Effekte während des Wachstums hervorgerufen werden kann. Wir untersuchen den Einfluss mehrerer Kontrollparameter auf die Streifenbreite und finden u.a. ein Arrhenius-Verhalten für die Temperaturabhängigkeit, in Übereinstimmung mit experimentellen Untersuchungen zur Phasenseparation in binären und ternären Systemen. Kanonische Monte Carlo Simulationen bestätigen, dass die Streifenbildung ein rein kinetischer Effekt ist: unter Gleichgewichtsbedingungen beobachten wir eine nahezu vollständige Separation der Adsorbatsorten. Gleichgewichtssimulationen mit einem gitterfreien Modell, das die unterschiedlichen Teilchengrößen der beteiligten Materialien berücksichtigt, zeigen, dass die Konkurrenz zwischen Teilchenbindungen und Gitterunterschied zu einem regelmäßigen Streifenmuster mit wohldefinierter Streifenbreite führt. Unter Nichtgleichgewichtsbedingungen beobachten wir sowohl die Streifenbildung als auch die experimentell berichtete Verästelung der Adsorbatinseln. Zur genaueren Untersuchung der Verästelung wird ein erweitertes Gittergasmodell betrachtet, dessen Parameter an charakteristische Diffusionsbarrieren aus dem gitterfreien Modell angepasst wurden. Die Ergebnisse der Simulationen mit dem erweiterten Gittergas zeigen, dass eine zufriedenstellende Beschreibung im Rahmen eines Gittergasmodelles nur möglich ist, wenn langreichweitige elastische Wechselwirkungen explizit berücksichtigt werden.

Im Anhang der Arbeit werden ergänzende Themen behandelt, die im Zusammenhang mit den Gittergassimulationen aus Kapitel 4 stehen. Dies sind die Realisierung der kanonischen Monte Carlo Simulationen, die Bestimmung der Gittergaskonfigurationen minimaler Energie, sowie die Methode zur Anpassung der Gittergasparameter an die Barrieren aus den gitterfreien Simulationen.

Abstract

In this PhD thesis, we develop models for the numerical simulation of epitaxial crystal growth, as realized, e.g., in molecular beam epitaxy (MBE). The basic idea is to use a discrete lattice gas representation of the crystal structure, where atoms can occupy only predefined lattice sites, and to apply kinetic Monte Carlo (KMC) simulations for the description of the growth dynamics. The main advantage of the KMC approach is the possibility to account for atomistic details and at the same time cover MBE relevant time scales in the simulation.

In chapter 1, we first describe the principles of MBE growth, pointing out relevant physical processes at the surface and the influence of experimental control parameters. We discuss different methods that are used in the theoretical description of epitaxial growth. The underlying concepts of the kinetic Monte Carlo method and the lattice gas approach are presented in detail. Important aspects concerning the design of a lattice gas model are considered, e.g. the solid-on-solid approximation of the crystal or the choice of an appropriate lattice topology. A key element of any KMC simulation is the selection of allowed events and the evaluation of Arrhenius rates for thermally activated processes. We discuss simplifying schemes like the bond counting ansatz that are used to approximate the corresponding energy barriers if detailed knowledge about the barriers is not available. Finally, the efficient implementation of the Monte Carlo kinetics using a rejection-free algorithm is described. In the following chapters we apply the combined lattice gas and KMC approach to different situations of epitaxial growth.

In chapter 2, we present in detail a solid-on-solid lattice gas model which aims at the description of (001) surfaces of II–VI semiconductors like CdTe or ZnSe, the main focus being on CdTe. The model accounts for the correct zincblende lattice structure as well as the relevant surface reconstructions of both Cd- and Te-terminated surfaces. Particles at the crystal surface interact via anisotropic nearest and next nearest neighbor interactions, whereas interactions in the bulk are isotropic. The strengths of the anisotropic interactions reflect known properties of the surface, e.g. the small energy difference between the $c(2\times2)$ and (2×1) vacancy structures of Cd-terminated surfaces. A key element of the model is the presence of additional Te atoms in a weakly bound Te* state, which is motivated by experimental observations of Te coverages exceeding one monolayer at low temperatures and high Te fluxes. The true mechanism of binding excess Te to the surface has not been clarified yet. In our model, we use a mean-field approach assuming a Te* reservoir with limited occupation.

In chapter 3, we perform KMC simulations of atomic layer epitaxy (ALE) of CdTe, using the lattice gas model from chapter 2. We study the self-regulation of the ALE growth rate and demonstrate how the interplay of the Te* reservoir occupation with the surface kinetics results in two different regimes: at high temperatures the growth rate is limited to one half layer of CdTe per ALE cycle, whereas at low enough temperatures each cycle adds a complete layer. The temperature where the transition between the two regimes occurs depends mainly on the particle fluxes. Both the temperature dependence of the ALE growth rate and the flux dependence of the transition temperature are

in good qualitative agreement with experimental results for CdTe. Comparing the macroscopic activation energy for Te* desorption in our model with experimentally determined values we find semiquantitative agreement. Our results indicate that a quantitative match with experiments should be feasible as soon as additional data from experiments or first principles calculations are available.

In chapter 4, we study the formation of nanostructures with alternating stripes during submonolayer heteroepitaxy of two different adsorbate species on a given substrate. We evaluate the influence of two mechanisms considered in the literature: kinetic segregation due to chemically induced diffusion barriers and strain relaxation by alternating arrangement of the adsorbate species. KMC simulations of a simple cubic lattice gas with weak inter-species binding energy show that kinetic effects are sufficient to account for stripe formation during growth. The dependence of the average stripe width on several control parameters is investigated. We find, for instance, an Arrhenius temperature dependence, in agreement with experimental investigations of phase separation in binary or ternary material systems. Using canonical Monte Carlo simulations we demonstrate that the observed stripes are not stable under equilibrium conditions: the adsorbate species rather separate into very large domains. Simulations with an off-lattice model that takes the lattice misfit of the involved particle species into account show that, under equilibrium conditions, the competition between binding and strain energy results in regular stripe patterns with a well-defined width that depends on both misfit and binding energies. In KMC growth simulations, the formation of stripe patterns as well as the experimentally reported ramification of adsorbate islands are reproduced. In order to clarify the origin of the island ramification, we investigate an enhanced lattice gas model whose parameters are fitted to a set of characteristic off-lattice diffusion barriers. The simulation results show that a satisfactory explanation of experimental observations within the lattice gas framework requires a detailed incorporation of long-range elastic interactions.

In the appendix of the work we discuss supplementary topics related to the lattice gas simulations in chapter 4. These are the realization of the canonical Monte Carlo simulations, the determination of lattice gas configurations with minimum energy, and the method used for fitting the lattice gas parameters to the off-lattice barriers.

Contents

1 Modeling of Epitaxial Growth 3
- 1.1 Molecular Beam Epitaxy . . . 3
  - 1.1.1 Microscopic Processes at the Surface . . . 4
  - 1.1.2 Influence of Control Parameters . . . 6
- 1.2 Theoretical Description . . . 7
  - 1.2.1 Density Functional Theory . . . 7
  - 1.2.2 Molecular Dynamics . . . 8
  - 1.2.3 Kinetic Monte Carlo Simulations . . . 9
- 1.3 Lattice Gas Models . . . 13
  - 1.3.1 Solid-On-Solid Representation . . . 14
  - 1.3.2 Choice of the Lattice . . . 15
  - 1.3.3 Full Diffusion Models . . . 16
- 1.4 Determination of Events and Rates . . . 17
  - 1.4.1 Bond Counting . . . 18
  - 1.4.2 Kawasaki-Type Energy Barriers . . . 19
  - 1.4.3 Simplifications in the Model Design . . . 20
- 1.5 Implementation of the Monte Carlo Kinetics . . . 21
  - 1.5.1 Rejection-Free Method . . . 21
  - 1.5.2 Simulation Algorithm . . . 22
- 1.6 Summary . . . 23

2 Kinetic Model of II–VI(001) Semiconductor Surfaces 25
- 2.1 Lattice Structure of CdTe . . . 26
- 2.2 Reconstructions of CdTe(001) Surfaces . . . 27
- 2.3 Lattice Gas Model . . . 29
  - 2.3.1 Representation of the Crystal Structure . . . 29
  - 2.3.2 Energetics . . . 31
  - 2.3.3 Reservoir of Weakly Bound Te . . . 32
  - 2.3.4 Dynamics and Growth . . . 33
  - 2.3.5 The Role of Te* Atoms . . . 36
  - 2.3.6 Surface Characterization . . . 38
  - 2.3.7 Parameter Estimation . . . 39
- 2.4 Summary . . . 40

3 Growth Rates in Atomic Layer Epitaxy **43**
3.1 Analysis of the Te* Reservoir Dynamics 44
3.2 Simulation of ALE Growth 47
  3.2.1 High Temperature Regime 47
  3.2.2 Low Temperature Regime 50
  3.2.3 Growth on a Vicinal Surface 53
3.3 Summary and Outlook 55

4 Nanostructure Formation in Surface-Confined Alloys **57**
4.1 Lattice Gas Description 58
  4.1.1 Simulation Model 59
  4.1.2 Symmetric Parameter Set 60
4.2 Simulations with Symmetric Parameter Set 61
  4.2.1 Island Geometry 62
  4.2.2 Equilibrium Simulations 63
  4.2.3 Step Geometry 65
  4.2.4 Influence of the Binding Energy 66
  4.2.5 Influence of the Adsorbate Concentration 68
  4.2.6 Kinetic Instability 69
4.3 Simulations with Next Nearest Neighbor Diffusion 72
  4.3.1 Influence of the Binding Energy 72
  4.3.2 Influence of the Adsorbate Concentration 74
  4.3.3 Temperature Dependence 75
4.4 Off-Lattice Description 77
  4.4.1 Simulation Model 78
  4.4.2 Equilibrium Simulations 79
  4.4.3 Morphology under Non-Equilibrium Conditions 82
4.5 Enhanced Lattice Gas 86
4.6 Summary and Discussion 89

A Supplementary Topics **91**
A.1 Canonical Monte Carlo Simulations 91
A.2 Minimum Energy Configurations 92
A.3 Fitting of Lattice Gas Parameters 94

Bibliography **98**

Chapter 1

Modeling of Epitaxial Growth

The fabrication of modern semiconductor-based devices like computer chips, solar cells or light emitting diodes relies to a large extent on the controlled growth of high quality thin crystalline films on monocrystalline substrates. In this context epitaxial growth techniques [1] such as molecular beam epitaxy (MBE) and its variants play an important role as they allow for a very precise control of the growth conditions [2]. By means of epitaxial methods it is, for example, possible to achieve very sharp interfaces between layers of different material species in compound semiconductors.

Despite the successful application of epitaxy in the fabrication of numerous material systems, there are still many open questions concerning, for instance, the influence of atomistic processes at the crystal surface on the macroscopic growth behavior [3]. In this context, numerical simulations provide a particularly important tool for the theoretical understanding of the involved microscopic mechanisms [4–6]. In this work we focus on the computational treatment of epitaxial crystal growth by combining a discrete lattice gas representation of the crystal structure with kinetic Monte Carlo simulations for the description of the growth dynamics.

In the following section we first describe the principles of MBE growth, pointing out relevant physical processes at the crystal surface and the influence of experimental control parameters. We then introduce important methods used for the theoretical description of epitaxial growth. In the remaining part of the chapter, we discuss in detail the underlying concepts of the kinetic Monte Carlo method and the lattice gas approach used in this work.

1.1 Molecular Beam Epitaxy

In an MBE growth chamber, one or several adsorbate materials are evaporated from effusion cells and subsequently directed as thermal atomic or molecular beam onto a substrate crystal which is kept at an elevated temperature, see Fig. 1.1(left). The arriving particles arrange on the substrate and contribute to the growth of a thin epilayer. If adsorbate and substrate material are chemically identical, the term homoepitaxy is

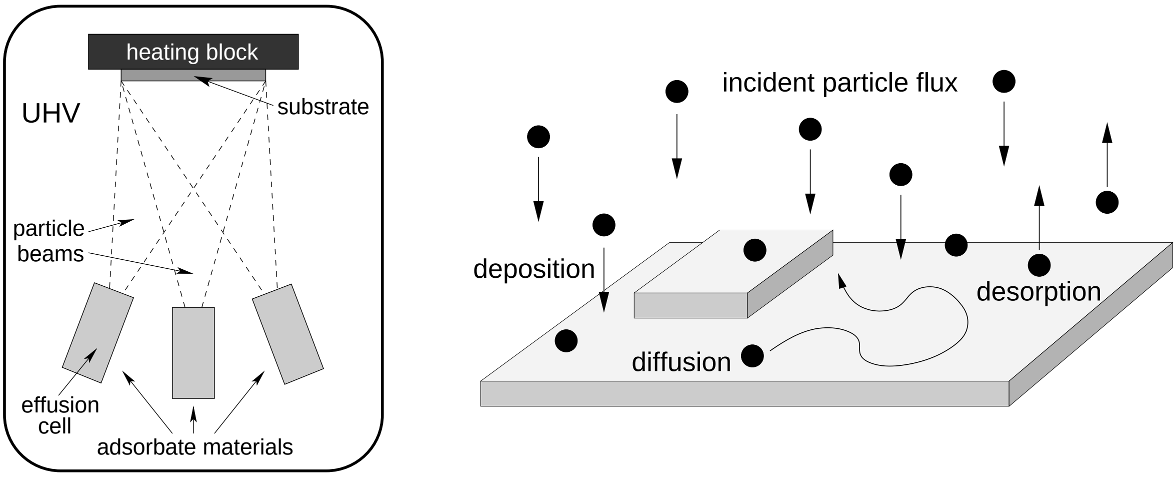

Figure 1.1: Left: Schematic illustration of an MBE growth system. Right: Schematic depiction of relevant surface processes during MBE growth.

used, whereas heteroepitaxy denotes the case when they are different. The epitaxial growth process is usually carried out under ultrahigh vacuum (UHV) conditions in order to suppress the contamination of the crystallized epilayer with unintentional impurities from the residual gas in the MBE chamber. Furthermore, the UHV environment allows for the in-situ monitoring of the growth process by, e.g., reflection high-energy electron diffraction (RHEED) measurements [2].

1.1.1 Microscopic Processes at the Surface

The morphology of the growing film is essentially determined by the interplay of three distinct microscopic processes at the crystal surface [3,6,7]: deposition of new atoms or molecules onto the surface, diffusion of adsorbed atoms (adatoms) on the surface, and desorption of atoms or molecules from the surface, see Fig. 1.1(right).

Deposition

Particles from the molecular beam impinge on the substrate with a constant flux F which is commonly measured in monolayers (ML) per second. Typical values for F range between $10^{-3}\,\mathrm{ML\,s^{-1}}$ and $1\,\mathrm{ML\,s^{-1}}$. In the modeling of MBE growth it is most frequently assumed that single atoms arrive at the surface, though in many experimental setups binary molecules or small clusters are evaporated from the effusion cells and dissociate upon arrival at the surface [2]. Atoms which approach the substrate surface are accelerated by the attractive potential of the substrate. The thus acquired kinetic energy is of the order of a few electron volts (eV) which is significantly higher than the energy of particles which are thermalized at the substrate temperature [6]. This may result in an enhanced, so-called transient mobility of the newly deposited particles until the excess energy is dissipated. The particles get trapped at energetically favorable sites with high coordination (i.e. number of neighboring atoms) which are generally close to the substrate. In simulation models this process may be accounted for by effective rules such as downward funneling [8, 9] or incorporation [10, 11]. In the latter case, the particle is moved to the site of lowest height within an incorporation radius r_{inc} around the location of deposition. Molecular dynamics simulations of condensation processes indicate that r_{inc} should be of the order of a few lattice constants [6, 12–14]. Incorporation processes may have a smoothening effect on the surface profile and thus favor layer-by-layer growth (cf. Sec. 1.1.2). At the end of the deposition process the now thermalized adatom is assumed to reside in a chemisorbed binding state with energy E_b corresponding to a local minimum in the potential energy.

Sometimes, chemisorption of the incident atom cannot be achieved immediately as there are, for example, no appropriate adsorption sites available in the vicinity of the deposition site. Nevertheless, the incoming atom may be captured in an intermediate weakly bound state close to the surface before reaching a regular adsorption site. Such weakly bound atoms play an important role in the context of epitaxial growth of compound semiconductors, cf. Chap. 3.

Diffusion

Diffusion of adsorbate particles on the surface is described as thermally activated process: due to thermal fluctuations at the surface a particle at a binding site may gain enough energy to escape the corresponding potential well and make a lateral jump to a neighboring binding site. In this hopping diffusion process, the adatom has to overcome an energy barrier (or activation energy) E_a which is given by the difference between the transition state energy E_t and the binding energy E_b at the initial site: $E_a = E_t - E_b$. The rate (probability per unit time) R of such a diffusion jump depends both on the energy barrier E_a and the substrate temperature T. Normally, this dependence is described by an Arrhenius law $R = \nu_o \exp\left[-E_a/(k_B T)\right]$ where k_B denotes Boltzmann's constant, and the prefactor ν_o is called the attempt frequency, cf. Sec. 1.2.3. In many experimental systems, the above described hopping diffusion of single adatoms constitutes the most important mechanism for mass transport on the surface. Alternatively, the migration of adatoms can sometimes be realized through the concerted movement of several atoms. In these so-called exchange-diffusion processes a diffusing adatom takes the place of an incorporated atom which then becomes the new adatom and continues the diffusion [15]. Whether a given diffusion process occurs predominantly via hopping or exchange mechanisms depends essentially on the heights of the corresponding energy barriers [6].

Desorption

Similar to surface diffusion, the desorption of adatoms can also be considered as thermally activated process. In this case the energy gain of the adatom due to thermal fluctuations is sufficient to overcome the binding energy E_b to the surface: the particle desorbs into the gas phase. The desorption rate is again given by an Arrhenius law where the activation energy E_a is simply equal to E_b. The value of the binding energy depends, e.g., on the particle species and the local geometry of the surface where the adatom sticks. In general, the binding energy increases with increasing coordination of the atom. Consequently, the desorption of free adsorbate particles is more frequent than that of particles which are incorporated in a step edge or in the flat terrace. Due to the high binding energies (typically a few eV) the desorption rate is usually small compared to the rates of deposition or surface diffusion. For many materials desorption thus can be neglected under typical MBE conditions. In the absence of a particle flux, though, desorption of adatoms becomes crucial, and a surface left in vacuum starts to sublimate with a temperature dependent sublimation rate.

1.1.2 Influence of Control Parameters

Apart from the selected adsorbate materials the most important experimental control parameters in MBE are the substrate temperature and the beam fluxes of the constituent material species. While the beam fluxes determine the rates with which new particles arrive at the surface, the substrate temperature influences the frequency of thermally activated diffusion or desorption processes: higher temperatures lead to increased particle diffusion and desorption.

In many cases, the particle fluxes and substrate temperature in MBE are adjusted such that diffusing adatoms have enough time to find favorable binding sites for incorporation before they will be overgrown or desorb from the surface. In the case of homoepitaxial growth on an initially flat substrate, high enough temperatures or low fluxes typically result in a smooth layer-by-layer growth mode, where the nucleation of new islands only starts after the previous layer has been completed [6].

In experiments, the substrate surfaces are not perfectly flat but exhibit a certain density of steps due to an unavoidable miscut of the substrate. On such a stepped (or vicinal) surface growth may proceed in a step flow mode if the temperature is high enough: in this case all atoms which are deposited onto a terrace bounded by two consecutive steps are captured by either the upper or lower step edge. Thus, island nucleation on the terraces is suppressed, and all steps move laterally with an average speed which depends on the deposition rate and the step spacing [6].

At low temperatures the reduced mobility of diffusing particles leads to frequent nucleation of new islands on the surface. Sometimes the transport of atoms between different atomic layers may be hindered by an additional energy barrier at the island edge (cf. Sec. 1.2.3). Then the formation of three-dimensional structures (mounds) on the surface can be observed. Mound formation leads to a steadily growing number of exposed atomic layers and thus to an increase of the roughness of the surface profile [6].

In the case of heteroepitaxy, the competition between strain—caused by a possible lattice-mismatch of the involved particle species—and interfacial energies leads to additional phenomena during growth like, for instance, the formation of dislocations in the crystal, or three-dimensional island growth, see e.g. [1,3,6,16,17].

1.2 Theoretical Description

The large variety of phenomena occurring during MBE growth constitutes a challenging task for a theoretical description, both under practical and fundamental aspects. From the practical viewpoint there is particular interest in understanding how the growth behavior can be influenced by material parameters or external control parameters such as temperature or particle fluxes. From the theoretical point of view, MBE growth is highly attractive as it provides an example of a system which is driven far from thermal equilibrium. In this case, no general theoretical framework like equilibrium statistical mechanics is available. Instead, new concepts may be developed and tested for their applicability in the description of growth phenomena as well as other, more general non-equilibrium systems.

In epitaxial growth, physical processes on a very wide range of length and time scales are involved. On the one hand, atomistic processes related to the adsorption or diffusion of particles operate in the nanometer and femto- to picosecond regime. On the other hand, the formation of micrometer-thick epilayers containing several thousands of atoms requires deposition times between seconds and hours. Consequently, a variety of rather different methods is currently applied in the theory, modeling and simulation in order to obtain a comprehensive picture of the growth process. They range from the detailed quantum mechanical treatment of microscopic processes to the macroscopic description in terms of stochastic differential equations or other continuum approaches, see e.g. [3,4,6,16,18].

In this work we focus on the combination of kinetic Monte Carlo simulations with discrete lattice gas models which constitutes one of the most widely used approaches in the computational treatment of epitaxial growth [18]. One advantage of this technique is, for instance, that atomistic details can be taken into account in the modeling, while at the same time the investigation of relatively large systems and long timescales is possible. In the following two sections we briefly discuss two other important methods which are used in the computational modeling of epitaxial growth, that is density functional theory and molecular dynamics. In the remaining part of this chapter we will discuss the underlying concepts of the kinetic Monte Carlo method and the lattice gas method, following the outline given by Biehl in Ref. [18].

1.2.1 Density Functional Theory

In principle, all macroscopic features evolving during growth can be traced back to the interplay of microscopic processes such as deposition, diffusion and desorption of atoms, which in turn imply the formation or breaking of chemical bonds at the surface. Consequently, a faithful description should account for the quantum mechanical nature of the electrons involved in the bonding.

In this context, density functional theory (DFT) has proved to be a very useful tool [19]. The method is based on the fact that, in principle, all information about a many-electron system can be derived from its ground state electron density by means of an appropriate density functional. Despite the enormous advantage of DFT over an explicit treatment of the many-particle Schrödinger equation the computational effort involved in the calculations is still very high and restricts the applicability of the method to relatively small systems containing only a few atoms or unit cells of periodic structures.

By means of DFT it is for example possible to calculate and compare the specific ground state energies of different surface reconstructions of a particular material system, see e.g. [20–23]. Besides the energies, also the corresponding surface structures, that is the precise positions of the atoms at the surface, are obtained by the calculations. Information about relevant surface configurations is particularly useful for the development of models which aim at the description of a specific surface or its evolution under non-equilibrium conditions, see Sec. 2.2.

For the investigation of dynamical properties during crystal growth, though, the knowledge of the ground state energies of only a few surface configurations is not sufficient. The growth behavior is essentially determined by thermally activated processes as e.g. surface diffusion of an adatom which lead from one configuration to a neighboring one. Such a transition occurs with a rate that is governed by the energy barrier which has to be overcome in the process, and an associated attempt frequency, cf. Sec. 1.2.3. In order to calculate the correct transition rate for a given process it is thus necessary to obtain reliable estimates of both parameters. Within the DFT formalism, the energy barriers of relevant diffusion processes can be determined by mapping out the potential energy surface as a function of the adatom position on the surface, see e.g. [24–27]. Using further assumptions from transition state theory (TST), also the attempt frequencies may be obtained [6, 27–29]. Thus, all the information necessary to calculate the transition rates can, in principle, be accessed within the DFT formalism. Having calculated the rates, they may then be used as input into realistic growth simulations, see e.g. [25–27, 30].

1.2.2 Molecular Dynamics

Another important method used successfully for the investigation of processes occurring in crystal growth is molecular dynamics (MD). In MD simulations the time evolution of an interacting many-particle system is modeled by numerically integrating the classical equations of motion [31]. By the use of appropriate algorithms it is possible to maintain specific physical conditions in the simulation, e.g. constant temperature or energy [31]. The forces acting between the particles are frequently derived from empirical potentials or DFT calculations [32]. The potentials used in the simulations range from simple pair-potentials of e.g. Lennard-Jones type, to highly sophisticated many-body potentials which have been fitted to reproduce certain bulk properties (e.g. lattice constants, elastic constants, cohesive energy, specific heat) of a specific material.

As molecular dynamics allows, in principle, for the description of the true dynamics of a system it is clearly a highly desirable method for the investigation of growth processes [5]. However, there are two problems which limit the practical application of

MD simulations in the context of crystal growth.

One problem concerns the reliability of the used interaction potentials [5]: pair potentials, which are attractive because of the moderate computational effort involved, have been applied with some success in the modeling of metals [33]. However, they are inadequate for the description of covalent materials where, e.g., the presence of directed bonds requires the incorporation of more complex many-body interactions [34, 35]. On the other hand, material-specific potentials which have been fitted to reproduce properties of the bulk may yield only a poor representation of surface effects as e.g. surface reconstructions.

The second, and actually more severe problem of the MD method is its restriction to short time scales. This limitation is caused by the fact that a MD simulation should account faithfully for all dynamical processes in the crystal. Consequently, the time step used in the numerical integration procedure has to be small compared to the shortest natural time scale in the system which is of the order of $10^{-13}\,$s, corresponding to the atomic vibrations in the crystal. Hence, time should be advanced in intervals of, say, $\lesssim 10^{-14}\,$s in the simulation. Under the assumption that for a moderate system size of 1000 particles about 10^6 simulation steps can be carried out by a standard MD scheme within a reasonable amount of simulation time, one arrives at a simulated physical real time of about $10^{-8}\,$s which is far away from MBE relevant time scales of seconds up to hours.

The problem with molecular dynamics is that a large part of the simulation time is actually spent for the description of collective vibrations of the crystal atoms which do not change the system configuration significantly over a relatively long period of time. The properties of a growing crystal, though, are governed essentially by *rare* thermally activated processes like the diffusion jump of an adatom on the surface, cf. Fig. 1.3. These events occur with an exponentially decreasing probability (see Sec. 1.2.3), and during the time interval covered by a typical MD simulation only a very small number of them will take place.

In conclusion, MD is currently not suitable for the description of crystal growth as the number of rare events which occur in the course of the simulation is too small. Nevertheless, MD is invaluable for the modeling of events which occur on *short* time scales or which involve the concerted movement of several atoms (e.g. exchange diffusion processes [6]). Furthermore, MD should be used for the modeling of processes which cannot be described as thermally activated, e.g. the transient mobility of deposited atoms along the surface (cf. Sec. 1.1.1).

1.2.3 Kinetic Monte Carlo Simulations

The time scale limitation of molecular dynamics can be overcome if only those processes are considered explicitly which lead to a significant change of the system configuration, whereas the fast vibrations of the atoms around their equilibrium positions are treated implicitly. This is the idea of the kinetic Monte Carlo method which is used in the simulations of the present work. In this section we will describe the basic concepts of this method.

Thermodynamic Monte Carlo

A Monte Carlo (MC) simulation is the numerical realization of a stochastic process where a system evolves over a set of configurations $\{i\}$ according to prescribed transition rates $R_{i\to j}$ for passing from configuration i to j. Monte Carlo simulations have been used extensively in *equilibrium* thermodynamics for the calculation of average values of thermodynamical quantities of interest, see e.g. [36]. In this context, a sequence of system configurations is generated such that they form a Markov chain [36] with a distribution that converges to the correct equilibrium distribution, that is the Boltzmann distribution

$$P_i = \frac{1}{Z} \exp\left(-\frac{E_i}{k_B T}\right). \tag{1.1}$$

Here, E_i denotes the energy of the system in configuration i, k_B is Boltzmann's constant and $Z = \sum_n \exp[-E_n/(k_B T)]$ is the partition function.

A reasonable MC dynamics should satisfy the condition of ergodicity which states that it should be possible to reach any system configuration from any other configuration if one waits long enough [36]. Usually, one requires in addition that the transition rates fulfill the condition of *detailed balance*,

$$R_{i\to j}\, P_i = R_{j\to i}\, P_j. \tag{1.2}$$

Then the convergence of the generated Markov chain to the equilibrium distribution P_i is guaranteed. Note that detailed balance is a sufficient but not necessary condition for the convergence [36].

By combination of Eqs. (1.2) and (1.1) the detailed balance condition reads

$$\frac{R_{i\to j}}{R_{j\to i}} = \exp\left(-\frac{E_j - E_i}{k_B T}\right). \tag{1.3}$$

One of the most widely used simulation algorithms which satisfies both the condition of ergodicity and detailed balance is the Metropolis scheme [36]. Here, a possible transition, say, from configuration i to j, is chosen at random and the corresponding energy change $\Delta E = E_j - E_i$ is calculated. If the energy of the system is lowered ($\Delta E < 0$) the transition is accepted with certainty, otherwise the transition is only accepted with probability $\exp\left[-\Delta E/(k_B T)\right]$.

In general, there is quite some freedom in the choice of the transition rates as only the ratio of the $R's$ is determined by Eq. (1.3). If one is not interested in *how* the system approaches thermal equilibrium, the actual choice does not have to reflect the real dynamic evolution of the system. In fact, in many cases the use of an "unphysical" dynamics yields a considerably faster equilibration of the system (cf. A.1).

Kinetic Monte Carlo

In contrast to thermodynamic MC simulations, the aim of kinetic Monte Carlo (KMC) simulations is to reproduce faithfully *nonequilibrium* or relaxation processes [5]. Here, the focus is on the correct time evolution of the considered system. Simulations of crystal growth are always of the kinetic type, and configurational changes now correspond to real physical processes (e.g. adatom diffusion). Consequently, the transition rates in KMC simulations of crystal growth have to reflect the physical properties of the system.

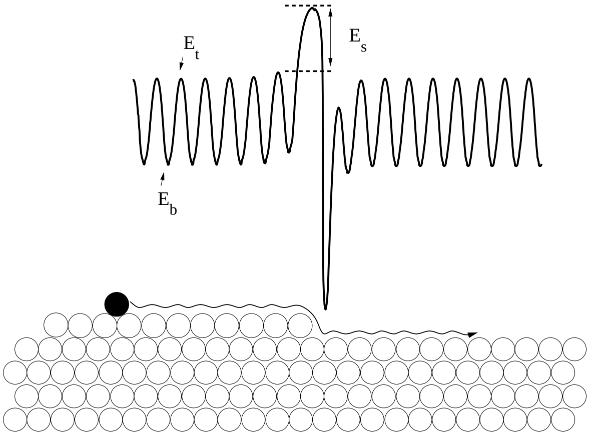

Figure 1.2: Potential energy surface (PES) for single adatom hopping diffusion on the surface of a two-dimensional Lennard-Jones crystal. E_b is the energy of a binding state, and E_t corresponds to the transition state of hopping diffusion. The Schwoebel barrier E_S hinders interlayer hops at the terrace edge. Figure courtesy of F. Much [17].

In order to illustrate the basic idea of the KMC approach, we consider as example the hopping diffusion of an adatom on the crystal surface. A simplifying interpretation of this situation is shown in Fig. 1.2: if we assume that the rest of the crystal is *frozen*, the adatom moves in a potential energy surface (PES) that results from its interactions with the other atoms. In reality, the underlying crystal rearranges and reacts to any movement of the adatom. However, as long as this does not lead to topological changes, the frozen crystal picture is essentially valid and appropriate for the following considerations. The local minima in the PES (Fig. 1.2) correspond to the relevant system configurations in the KMC approach and are termed the *binding states*. Due to thermal fluctuations, occasionally a jump from one such minimum to a neighboring one will occur. The typical waiting time for a transition is given by an *Arrhenius law* of the form $\tau = \tau_o \exp\left[E_a/(k_B T)\right]$ or

$$R = \nu_o \exp\left(-\frac{E_a}{k_B T}\right) \tag{1.4}$$

for the corresponding transition rate, respectively. The rate R decreases exponentially with the height of the energy barrier (activation energy)

$$E_a = E_t - E_b \tag{1.5}$$

which has to be overcome in the process, cf. Fig. 1.2. Here, E_b denotes the energy of the binding state, whereas E_t is the energy of the *transition state*. The energy barrier

E_a is compared with the typical thermal energy $k_B T$ in the system, i.e. the higher the temperature T the more frequent becomes the event. The preexponential factor ν_o is often referred to as the *attempt frequency.* In the Arrhenius law it is assumed to be independent of the temperature.

Figure 1.2 shows the PES for a single particle in the vicinity of a terrace edge. In the center of the upper or lower terrace, the PES is oscillatory with equivalent minima at the regular lattice sites and identical barriers. Near the edge, the shape of the PES shows some distinct features: a very deep minimum is found right at the step due to the good coordination, i.e. the interaction with many neighbors. Consequently, a particle that has attached to the upper terrace will detach with a relatively low rate as the associated energy barrier E_a is high. A second pronounced feature is the additional, so-called *Schwoebel barrier* E_S [3,4,6] for hops from the upper to the lower terrace (or vice versa). Here, the transition state corresponds to a very weak binding of the adatom and hence interlayer diffusion is hindered effectively. This can result in the formation of pronounced mounds in the course of growth, see e.g. [3,4,6]

In transition state theory (TST), the Arrhenius law for thermally activated transitions is motivated by arguing that the occupation of binding and transition states should correspond to effective thermal equilibrium situations. Following this line of thought one obtains the expression in Eq. (1.4). In principle, the value of the attempt frequency ν_o can be derived by taking into account the (vibrational) entropies, i.e. the free energies of binding and transition state. However such an evaluation can be quite involved and goes well beyond the frozen crystal approximation. Consequently, good estimates of attempt frequencies are rarely available in the literature. For this reason, in many simulations a common attempt frequency is assumed for all possible diffusion processes in the system. Commonly, values on the order of $10^{12} - 10^{13}\,\mathrm{s}^{-1}$ are chosen for ν_o, corresponding to the typical frequency of atomic vibrations in the crystal [3]. For a discussion of several approaches to the evaluation of transition rates and attempt frequencies, see e.g. [6,27,29,37,38].

The use of a single attempt frequency ν_o in the system has the advantage that the Arrhenius rates [Eq. (1.4)] immediately satisfy the detailed balance condition [Eq. (1.3)]. Consider for example two neighboring binding states i and j with binding energies E_i and E_j, respectively. Going from one binding state to the other, the system has to pass the transition state with energy E_t yielding $R_{i \to j} = \nu_o \exp[-(E_t - E_i)/(k_B T)]$ and $R_{j \to i} = \nu_o \exp[-(E_t - E_j)/(k_B T)]$ as transition rates for the forward and the backward process, respectively. Thus one recovers directly Eq. (1.3) as ν_o and the dependence on E_t cancel in the ratio of the rates. The detailed balance condition is by no means a necessary requirement for meaningful simulations, especially not in situations far from equilibrium [18]. However, it conveniently guarantees that the system—in absence of deposition and desorption— would approach the correct thermal equilibrium eventually, i.e. a Boltzmann distribution [Eq. (1.1)] of binding states [36].

Note that deposition and desorption processes in MBE models always violate the detailed balance condition [18]. Since deposition is not an activated process, the discussion of detailed balance becomes meaningless in this context. In desorption a particle

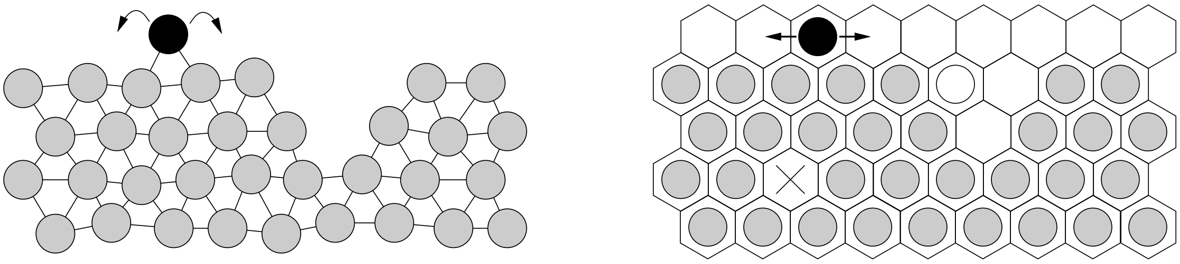

Figure 1.3: Illustration of the lattice gas representation of a two-dimensional crystal. Left: atoms in the crystal assume continuous positions. Straight lines denote nearest neighbor bonds. In an MD simulation thermal fluctuations of the whole structure may lead to a jump of the adatom (black) to a neighboring pair of surface atoms. Right: in the lattice gas approximation atoms can occupy only predefined lattice sites (indicated by the hexagonal cells). In a KMC simulation the adatom can jump to the left or right neighbor site with a given rate. The cross marks a vacancy in the bulk, and the open circle denotes an atom which forms an overhang. Both features would be forbidden under the solid-on-solid condition.

has to overcome an energy barrier E_a which is simply given by its binding energy at the surface. Hence, desorption can be implemented as activated process with a corresponding Arrhenius rate [Eq. (1.4)]. However, the process is irreversible: in an ideal MBE environment a perfect vacuum is maintained in the growth chamber and desorbed particles will be removed immediately. The situation differs significantly from a surface that may exchange particles with a surrounding vapor or melt.

1.3 Lattice Gas Models

In principle, the kinetic Monte Carlo method described in Sec. 1.2.3 can be applied to off-lattice models with continuous particle positions, see e.g. [17]. This requires the determination of the relevant energy barriers from the PES "on the fly" which can become quite involved. Therefore the vast majority of KMC studies uses additional simplifications in the simulations [18].

If the material under consideration is expected to crystallize in a regular lattice without dislocations or other defects one can use a discrete representation of the crystal where particles can occupy only predefined sites of a given lattice structure. In such *lattice gas models*, each lattice site is either empty or occupied by (at most) one atom, cf. Fig. 1.3. In a deposition process, the state of a particular lattice site changes from empty to occupied. Conversely, the desorption of an atom changes the state of a lattice site from occupied to empty. A diffusion process corresponds to a jump of an atom from one lattice site to a neighboring one. Hence, the states of both sites are exchanged, cf. Fig. 1.3.

A particular configuration of the lattice gas can, for instance, be represented by a set of integer variables $\{n_i\}$, where n_i denotes the occupation state of the i-th lattice

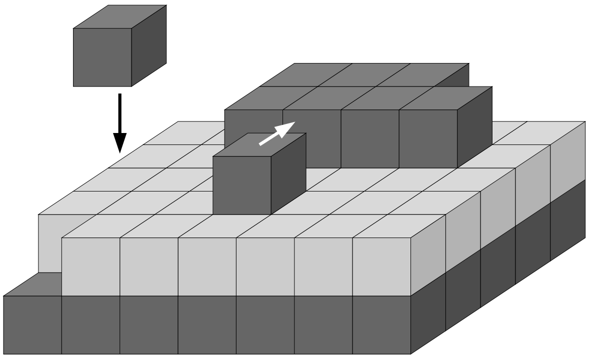

Figure 1.4: Sketch of a simple cubic solid-on-solid lattice gas model. For clarity alternating layers are colored differently. Since vacancies and overhangs are not allowed, the system configuration is fully described by an integer array which stores the height of the surface above the square substrate. The deposition of a new particle (black arrow) and the diffusion hop of an adatom attaching to a small cluster (white arrow) are shown.

site. For example, in a monoatomic lattice gas model, $n_i = 0$ corresponds to an empty site and $n_i = 1$ indicates a lattice site which is occupied by an atom. In a model with m different particle species, $n_i = 0$ still would represent an empty site whereas $n_i = k$ would correspond to the occupation of site i with a particle of type k $(1 \leq k \leq m)$.

In some material systems (e.g. semiconductors), atoms at the crystal surface may be slightly shifted from their corresponding bulk positions due to surface reconstructions (cf. Sec. 2.2). As long as the topology of the lattice remains unchanged, this effect can be taken into account within the lattice gas framework by adding additional discrete degrees of freedom to the model, see the discussion of the growth model of II-VI(001) semiconductor surfaces presented in Chap. 2.

1.3.1 Solid-On-Solid Representation

Under the assumption that neither vacancies nor overhangs are formed in the growing crystal, the so-called solid-on-solid (SOS) approximation may be used in the modeling. Here, each atom of a given layer has the maximal possible number of binding partners in the layer below. For example, in the case of a simple cubic (sc) structure the SOS condition requires that each atom sits on top of another atom (cf. Fig. 1.4) whereas in an SOS representation of a face-centered cubic (fcc) crystal with (001) (or (111)) surface orientation each atom must have four (three) nearest neighbors in the layer below, see Fig. 1.5. For other crystal structures similar conditions can be derived, see e.g. Sec. 2.3.1 for an SOS representation of the zincblende lattice. If the SOS approximation is used in a lattice gas model then a given system configuration can be described conveniently by an integer array of variables which stores the height of the surface above the substrate. The main advantage is that the array size is fixed by the surface area, that is, the required memory to store the system configuration does not increase when the thickness of the simulated system becomes larger.

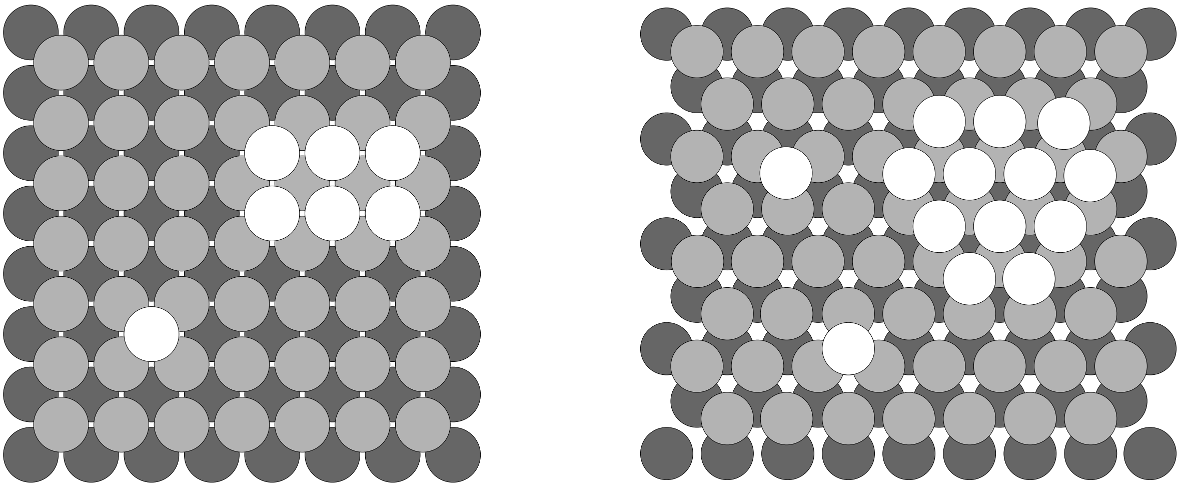

Figure 1.5: Different surface orientations of a face-centered cubic (fcc) crystal. Darker circles mark atoms which are located deeper. Atoms which make up an fcc(001) facet form a square lattice (left panel) whereas atoms of an fcc(111) facet arrange in a triangular lattice (right panel). In both cases the edges of adsorbate islands align with the lattice axes. On the fcc(111) surface two distinct types of binding sites are available: the upper single adatom and the atoms of the small island sit in fcc sites whereas the lower single atom sits in an hcp site. The combined set of fcc and hcp sites forms a honeycomb lattice. In an SOS model of the fcc(001) surface each atom must have four nearest neighbors in the layer below, in the case of the (111) surface three nearest neighbors are required.

1.3.2 Choice of the Lattice

In principle, all relevant lattice structures [39] can be represented in a solid-on-solid fashion, see e.g. [36] for the practical implementation of several lattice types. The specific choice of the lattice geometry depends on the purpose of the KMC simulation. If the simulation aims at the description of a specific material system, clearly the correct topology should be represented in the model as it determines, for instance, neighborhood relations and the potential diffusion events. On the other hand, if the focus is on the influence of certain atomistic processes on the qualitative features of the morphology the use of a simple lattice structure (e.g. simple cubic) is justified.

Note that the required lattice representation may depend on the considered surface orientation. For example, atoms of an fcc(001) surface arrange in a square lattice whereas for the fcc(111) orientation the surface atoms occupy sites on a triangular lattice, see Fig. 1.5. The modeling of growth on an fcc(111) surface should furthermore account for the two nonequivalent adsorption sites at the surface, i.e. the fcc and the hcp sites [39], see Fig. 1.5. An adatom which occupies an fcc site continues the regular ABC stacking sequence, whereas adsorption on an hcp site leads to ABA [39]. In experiments, both islands with regular fcc-stacking and islands with faulted hcp-stacking have been observed, depending on the considered material system and experimental conditions (e.g. [40]). A simulation model which aims at the description of stacking-fault formation thus necessarily has to incorporate the appropriate lattice representation for the adsorption sites which would be a honeycomb structure in this case [36].

In general, the shape of growing adsorbate islands directly reflects the symmetry of the lattice as the island edges usually align with the lattice axes. Thus, rectangular islands are commonly observed on substrates with square symmetry whereas islands with triangular or hexagonal shape form on an fcc(111) surface (cf. Fig. 1.5), depending on the experimental conditions [6]. In this context, the choice of a reasonable substrate geometry and the use of appropriate (periodic) boundary conditions in the model are essential in order to reduce boundary effects in the simulation of finite systems [18]. The use of an inadequate geometry, e.g. a square shape substrate for the representation of an fcc(111) surface, may yield complications as the shape of large islands that align with the lattice axes might conflict with the substrate geometry. In order to avoid such artefacts, the design of the substrate should reflect the lattice symmetry [36].

In the literature, lattice gas models with simple cubic symmetry and only one particle species have been used frequently as they allow for a straightforward implementation. Due to their conceptual simplicity these models obviously cannot describe properties of real materials faithfully. Nevertheless, they are quite useful for the investigation of basic and qualitative features of epitaxial growth as, e.g., kinetic roughening or coarsening of the surface [4]. For example, growth models with sc symmetry and effective one-particle dynamics allow for the simulation of large system sizes and time-scales [10, 41]. Thus, the influence of, e.g., step edge diffusion barriers, Schwoebel barriers, or incorporation mechanisms on the growth morphologies or scaling exponents in kinetic roughening may be studied efficiently [42]. Several properties of growth processes are believed to be universal, i.e. they should not depend on the symmetry of the crystal anyway, see e.g. [43].

1.3.3 Full Diffusion Models

In the conceptually simplest growth models, only the most recently deposited particle is considered mobile at a given time [4]. For example, upon arrival at the surface, an adatom may migrate a few lattice spacings to an empty site of lower height (in the vicinity of the deposition site) where it sticks irreversibly. After that, the simulation continues with the deposition of a new particle. In the simplest case, deposited particles become immobile immediately after incorporation into the crystal. Since time-consuming activated diffusion steps are completely neglected in this scheme, the simulation of large system sizes and the deposition of many adlayers becomes possible. Such models with limited adatom mobility are well suited for the description of basic phenomena like kinetic roughening of self-affine surfaces [4]. However, the assumption that only the incoming particle is mobile is rather unrealistic.

A more realistic, material-specific model should account for simultaneous diffusion and desorption events of many adatoms on the surface. In so-called *full diffusion models*, all atoms are considered mobile at the same time, in principle. Here, the deposition of a particle is only one possible event among all other processes and has to be implemented with the corresponding rate [18]. The simultaneous movement of many adatoms in the system leads to a much broader spectrum of possible events which in turn increases the computational costs of the model.

In the standard SOS approach only atoms right at the surface are considered mobile [18]. In the case of the simple cubic lattice this would mean that only atoms could move which have no nearest neighbor sitting on top, cf. Fig. 1.4. Bulk particles are surrounded by occupied lattice sites and vacancies are excluded. Concerted moves or exchange processes are usually omitted, thus the entire bulk remains fixed. In many cases the adatom mobility is further restricted due to simplifying assumptions in the model design, see Sec. 1.4.3.

1.4 Determination of Events and Rates

A key element of any kinetic Monte Carlo model is the determination of allowed processes (events) in the simulation and the calculation of the corresponding rates [18]. In contrast to e.g. molecular dynamics where all atomic movements arise naturally from the many-particle interactions, in KMC simulations a “catalogue” of possible microscopic events has to be *predefined*, and rates have to be assigned to the considered processes [18]. If the simulation aims at a faithful description of a specific material, then as many atomistic details as possible should be captured in the model, and the rates should be based on reliable (possibly first-principles) calculations. One problem is that it is sometimes hard to tell in advance what are the relevant processes: a multitude of different atomic configurations can occur in the course of growth, and some processes may possibly be overlooked, especially if the associated atomic motions appear counterintuitive. By unintentional exclusion of potentially crucial mechanisms it might be that essential properties of the system are missed in the simulation.

A typical KMC simulation of MBE growth accounts for the three basic mechanisms occurring at the surface: deposition, diffusion and desorption of adatoms. In the modeling of deposition, usually an ideal beam of particles is assumed which deposits, on average, the same amount of material per unit time and area everywhere on the surface [18]. Fluctuations on the atomistic level are represented in an SOS model by choosing randomly one of the available lattice sites for each deposition event. The rate for a deposition event at a given lattice site is defined as the number of incoming particles at this site per unit time, and the overall deposition rate R_d is obtained by multiplication with the system size.

The modeling of thermally activated diffusion and desorption processes requires knowledge about the energy barriers E_a which enter the corresponding Arrhenius rates [Eq. (1.4)]. In this context, input from experiments, molecular statics using semi-empirical potentials (e.g. [33, 44]) or DFT calculations [27] may help identify the relevant physical processes and associated energy barriers or rates. For example, in GaAs growth simulations by Kratzer *et al.* [25, 26], 30 distinct process types had to be taken into account based on DFT results. In general, the numerical evaluation of energy barriers or rates can become quite involved. For instance, in many cases diffusion events can be realized either by a hopping or exchange mechanism. In principle, for each configurational change, all possible realizations along with the correct transition paths would have to be identified which is a demanding task (e.g. [45]).

1.4.1 Bond Counting

In those cases where the knowledge about energy barriers is not sufficient or even not available, simplifying schemes have to be used in the calculation of the transition rates. Sometimes, the relevant barriers for surface diffusion or desorption of adatoms can be represented efficiently by a small number of independent parameters [18]. In this context, bond counting schemes have been used successfully in KMC simulations. The idea is to use only a few number of distinct barriers but explicitly account for the energies of the involved binding states [18]. In the bond counting approach one assumes that the binding energy of an adatom at a given site is essentially determined by the interactions ("bonds") with its nearest or next nearest neighbors, whereas the influence of atoms which are farther away can be neglected. This accounts for the short-range character of chemical bonds in real material systems.

A straightforward realization of the bond counting scheme in a simple cubic SOS model could be that each pair of nearest neighbor atoms forms a bond of equal strength. The determination of the energy E_b of a given binding state (i.e. system configuration) then amounts to adding up the contributions of all nearest neighbor interactions in the system.

For transitions between neighboring system configurations, e.g. by a diffusion hop of an adatom, both the energy of the initial binding state (E_b) and the energy of the transition state (E_t) are needed as they determine the corresponding energy barrier $E_a = E_t - E_b$. A reasonable assumption is that E_a increases with the depth of the initial binding state. In a particularly simple implementation of the bond counting method, the activation energy E_a is thus determined solely by the binding energy of the adatom at the initial site. In the example from above this would mean that the activation energy for a diffusion hop of an adatom can be obtained by counting the number of nearest neighbor bonds which are *broken* in the process. This simple approximation of E_a implies that the energy of the transition state is the same for all possible moves in the system. Another consequence is that e.g. the barriers for the diffusion of an adatom along the border of a terrace (step edge diffusion) and that for detachment from the step edge are always the same as the number of broken bonds is equal in both processes. In many cases, this is not a very good representation of the physical reality. In fact it is frequently observed experimentally that adatoms which are captured by a step edge display fast diffusion along the step edge whereas detachment from the step edge occurs only with a very low probability. This implies that the step edge diffusion barrier can be much lower than the barrier for detachment which cannot be reproduced by the simple bond counting scheme.

1.4.2 Kawasaki-Type Energy Barriers

A better representation of the energy barriers E_a within the bond counting approach can be achieved if the energies of both initial and final system configuration are taken into account. For example, one could assume that the energy of the transition state E_t is given by the maximum of the energies of initial and final binding state, E_i and E_f, plus a constant B_o which plays the role of a characteristic barrier for all nearest neighbor hops within the layer: $E_t = \max\{E_i + B_o, E_f + B_o\}$, see Fig. 1.6(a). Then, the activation energy $E_a = E_t - E_i$ for the transition from state i to f becomes

$$E_a = \max\{B_o, B_o + \Delta H\}, \tag{1.6}$$

with $\Delta H = E_f - E_i$ being the energy difference between initial and final state. In the simplest case, E_i and E_f are obtained, as above, by counting nearest or next nearest neighbor bonds and adding up the associated binding energies.

In the literature the barriers given by Eq. (1.6) are referred to as Kawasaki-type energy barriers due to the relationship with the Kawasaki-algorithm for the conserved-order-parameter Ising model, see [36]. From Eq. (1.6) it follows that the activation energy E_a is directly given by B_o if $\Delta H \leq 0$. This is the case for e.g. free surface diffusion but also for diffusion along a step edge if the initial and final site are energetically equivalent and hence $\Delta H = 0$. On the other hand, detachment of an adatom from a step edge always implies breaking the bond to the atom sitting in the step edge. Here, the associated energy gain $\Delta H > 0$ adds to the barrier B_o, and thus the activation energy E_a for detachment is larger than that for step edge diffusion.

The rates for the different processes are obtained by substituting Eq. (1.6) into the Arrhenius form [Eq. (1.4)]. Note that the detailed balance condition is satisfied by construction: apart from the extra barrier B_o, which cancels out in Eq. (1.2), the prescription is equivalent with Metropolis like rates in equilibrium Monte Carlo simulations [36].

If only one characteristic barrier B_o is present in the system, the factor $\exp\left[-B_o/(k_B T)\right]$ appears in all rates and can be taken to re-define the time scale. In general, though, several such barriers may apply to different types of events. For example, the diffusion of a free adsorbate particle on the substrate may be faster than the diffusion along a step edge. Consequently, a higher barrier would have to be assumed for the latter process. However, this cannot be realized by the simple expression in Eq. (1.6) which yields B_o for both processes since $\Delta H = 0$, cf. Fig. 1.6(a).

In a generalized version of the Kawasaki-type energy barriers, the single parameter B_o in Eq. (1.6) is thus replaced by two distinct barriers B_i and B_f which correspond to the initial and final system configuration:

$$E_a = \max\{B_i, B_f + \Delta H\}. \tag{1.7}$$

Again, $\Delta H = E_f - E_i$ denotes the energy difference between initial and final binding state. With this modification it is possible to assign different energy barriers to the two

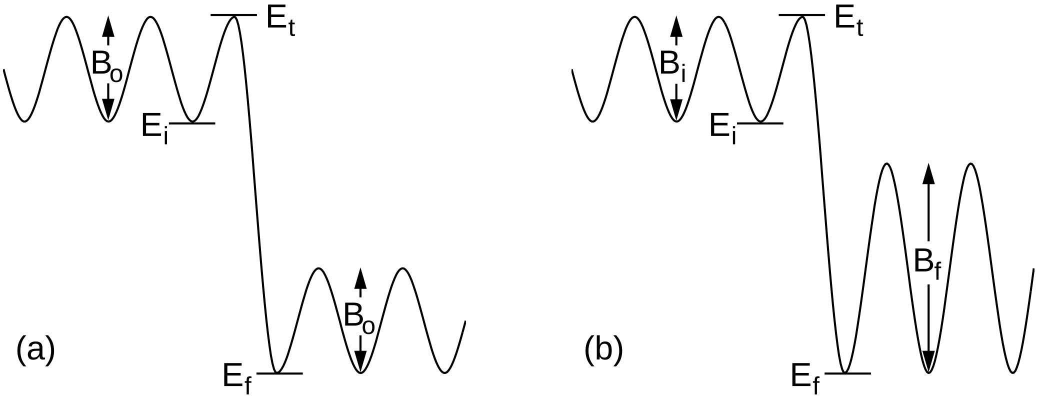

Figure 1.6: Illustration of Kawasaki-type energy barriers. The energies E_i, E_f and E_t of two neighboring binding states and the corresponding transition state are indicated, respectively. In this example, E_i could correspond to the binding energy of a free adatom on the surface whereas E_f marks the binding energy of the adatom at a step edge. (a) In the simple version [Eq. (1.6)] the barrier for free surface diffusion and diffusion along the step edge is the same, that is B_o. (b) In the generalized version [Eq. (1.7)] the barrier for free surface diffusion is B_i whereas a higher barrier B_f holds for step edge diffusion.

situations mentioned above, see Fig. 1.6(b). Note that Arrhenius transition rates with the modified energy barriers [Eq. (1.7)] still satisfy the detailed balance condition as the barriers B_i and B_f cancel out in Eq. (1.2).

1.4.3 Simplifications in the Model Design

Frequently, further simplifying assumptions are made in the simulations in order to reduce the computational effort [18]. In some cases certain processes may be excluded explicitly from the simulation if the associated time-scales are larger by orders of magnitude than those for other processes. For instance, depending on the material species and the experimental conditions in the MBE environment, the typical waiting time for a desorption event of an atom may be large compared to the time needed to deposit an entire monolayer (ML) of adsorbate material. For example, at an MBE growth temperature of 500°C the macroscopic sublimation rate of Si is of the order of $10^{-14}\,\mathrm{ML\,s^{-1}}$ [3]. Thus, assuming typical MBE deposition rates of $10^{-3} - 1\,\mathrm{ML\,s^{-1}}$, obviously desorption of Si atoms is negligible at this temperature and could be omitted in a simulation of Si growth. On the other hand, for very small particle fluxes or high temperatures adatom desorption becomes clearly relevant: the crystal does not grow but rather evaporates in this case, and desorption should thus be incorporated in the simulation.

The detachment of atoms from terrace edges or small islands is also expected to occur only with a very small rate if the corresponding binding energies are large. Hence, in an extreme case one might consider all detachment processes forbidden in the simulation (i.e. their rate is set to zero) which reduces the number of possible events considerably [18]. The justification of this simplification is again based on the comparison of the relevant time scales which are essentially determined by the incoming flux and the substrate temperature. For example, one could argue that in the presence of a strong particle flux, two-dimensional islands on the surface would grow rapidly by capturing new adatoms, and thus atoms at the island edges would be enclosed before they could possibly detach. Note that the implementation of irreversible attachment in the simulation violates the detailed balance condition as only one of the rates in Eq. (1.2) is non-zero.

In many cases, one is interested in the morphology of adsorbate islands during the initial stages of growth for which the adsorbate coverage is less than one monolayer [4, 6]. In this so-called submonolayer regime, the growing islands are essentially two-dimensional, that is they have a thickness of one atomic layer. At low coverages most of the deposited atoms will land on the substrate, only a small fraction will be deposited on top of existing islands. An atom which lands on top of an island will start diffusing until it reaches the island edge. At the edge the adatom may jump down or—in the presence of a high Schwoebel barrier (cf. Sec. 1.2.3)—will be reflected. In the latter case, the atom continues moving on top of the island. In the extreme case of an infinite Schwoebel barrier the atom will be reflected each time it encounters the island edge and thus never leaves the upper terrace. A simulation which focuses only on the first layer of the islands could neglect the movement of second layer atoms as they do not contribute to the growth of the base layer.

1.5 Implementation of the Monte Carlo Kinetics

A straightforward implementation of the stochastic Monte Carlo kinetics in a simulation algorithm could be realized as follows [5]: (i) select one of the possible events k at random with equal probability, (ii) calculate or look up its rate R_k, and (iii) accept (perform) the event k with probability R_k/R_{max}, where R_{max} is the largest of all rates of possible events in the model.

However, this algorithm is not very efficient for the simulation of crystal growth [5] as the acceptance probabilities for diffusion or desorption events can become rather small due to the exponential decrease of the Arrhenius rates [Eq. (1.4)]. Thus, especially at low temperatures a large fraction of selected events will be rejected, and possibly time-consuming computations have been performed for the determination of the corresponding rates without changing the system at all [18].

1.5.1 Rejection-Free Method

To circumvent the problem of small acceptance probabilities we use a rejection-free (continuous-time) algorithm in our simulations [36]. Here, in each Monte Carlo step an event k is selected according to its rate R_k and *performed.* Thus, the number of non-modifying steps in the simulation is zero, that is we never reject any moves at all.

The use of a rejection-free algorithm involves some additional computational effort: as the re-calculation of all the rates from scratch every time would be very expensive we have to keep track of the possible events and corresponding rates during the simulation. We then re-calculate only the rates of those events which are affected by some given event. The required bookkeeping effort may slow down the simulations to some extent. However, the gained speedup caused by the fact that no Monte Carlo steps are wasted usually outweighs the extra complexity of the algorithm, especially for simulations at low temperature [36].

In continuous-time Monte Carlo simulations the simulated physical time is not directly proportional to the number of MC steps since for different processes the associated time intervals have different lengths [5]. Under the assumption that no two events occur at the same time and that the sequence of events forms a Poisson process, it follows [46] that the time interval τ between two successive events (waiting time) is exponentially distributed with probability density $P(\tau) = R\exp(-R\tau)$ and average value $\langle\tau\rangle = 1/R$. Here, R denotes the sum of the rates of all possible events for a given system configuration.

In the simulation, exponentially distributed time intervals are generated from a uniformly distributed random variable through appropriate transformation of the corresponding probability densities [36]. Accordingly, the time increment between two Monte Carlo steps is given by

$$\tau = -\frac{\ln\rho}{R}, \tag{1.8}$$

where ρ is a uniformly distributed random number with $\rho \in]0,1]$.

1.5.2 Simulation Algorithm

At the beginning of a simulation run the rates of all possible microscopic events, i.e. deposition, desorption, and diffusion of particles, have to be calculated: particle deposition occurs with a rate R_d which follows from the given particle fluxes, and for diffusion and desorption processes we assume an Arrhenius dynamics with rates $R_i = \nu_i \exp[-E_{a,i}/(k_B T)]$, cf. Sec. 1.2.3. Subsequently, the events and the corresponding rates are stored in an appropriate data structure, and the total rate $R = R_d + \sum_i R_i$ is calculated. Following the work by Ahr [11] we use a complete binary tree for the storage and selection of particular events.

One iteration of the Monte Carlo algorithm then consists of the following steps:

1. Draw an event k according to its probability $p_k = R_k/R$ and perform it.
2. Re-calculate the rates of all affected events and the total rate R. Update the search tree accordingly.
3. Increase the system time by a time interval τ which is given by Eq. (1.8).

4. Go to step 1 unless some condition to terminate is fulfilled (e.g. a certain amount of physical time has passed or a maximum number of particles has been deposited).

Usually, interactions in a lattice gas model are only short-ranged (e.g. nearest neighbor or next nearest neighbor particle interactions). Then the number of events whose rates have to be re-calculated in step 2 is small, e.g. of order $\mathcal{O}(1)$.

1.6 Summary

In this chapter we have discussed the combined use of kinetic Monte Carlo simulations and discrete lattice gas models in the computational treatment of epitaxial crystal growth. A major advantage of this approach is the possibility to account for the relevant atomistic processes at the surface (deposition, diffusion, desorption of adatoms), while at the same time MBE relevant time scales of seconds or minutes can be covered in the simulation. The time scale enhancement compared to, e.g., molecular dynamics simulations is essentially due to the implementation of appropriate short cuts in the treatment of rare thermally activated diffusion or desorption events within the stochastic Monte Carlo method.

Depending on the specific purpose of the simulation, a variety of aspects has to be considered in the construction of the lattice gas model: among others, the choice of an appropriate lattice structure, the incorporation of the relevant atomistic processes, and the assignment of correct transition rates to the considered events are particularly important in this context.

In the absence of sufficient input from experimental studies or DFT calculations the energy barriers which enter the Arrhenius rates of thermally activated processes have to be approximated. In this context, the popular bond counting approach and the concept of Kawasaki-type energy barriers have been discussed. Finally, the implementation of the Monte Carlo kinetics by means of a rejection-free simulation algorithm has been described.

In the following, we will present applications of the lattice gas and kinetic Monte Carlo method in different situations of epitaxial growth. A lattice gas model which aims at the faithful description of (001) surfaces of II–VI semiconductors as e.g. CdTe or ZnSe is introduced in the next chapter. The model accounts for the correct zincblende structure of the considered material systems, as well as relevant surface reconstructions. Using kinetic Monte Carlo simulations we will show in Chap. 3 that the experimentally observed temperature dependence of growth rates in atomic layer epitaxy of CdTe can be explained within the framework of this model.

In Chap. 4 we focus on the formation of nanostructures during submonolayer heteroepitaxy of two different adsorbate materials on a given substrate. One aim is to determine the influence of kinetic effects on the morphology of growing islands. Therefore kinetic Monte Carlo simulations of a model ternary system are performed, using a simple cubic lattice gas with a small number of interaction parameters. In order to allow for a comparison with results obtained by an off-lattice simulation method the lattice gas model will be refined later by fitting the model parameters to a set of off-lattice energy barriers.

Chapter 2

Kinetic Model of II–VI(001) Semiconductor Surfaces

Research on II–VI compound semiconductors (e.g., CdTe, ZnSe, BeTe, ZnO, CdS and others) has become a field of growing interest during the past years [47]. In particular, their potential applicability in electronic or optoelectronic devices has made them a promising material class from the technological point of view. For example, wide bandgap compounds such as BeTe allow for the development of green or blue light-emitting diodes (LED) [48]. On the other hand, incorporation of Mn in II–VI compounds results in diluted magnetic or even ferromagnetic semiconductors with unique magneto-optic or magneto-transport properties which may be used in magnetic storage devices [47].

A wide range of topics is currently under investigation, including the formation and optical or electronic properties of self-assembled quantum dots, synthesis and characterization of nanocrystals [49], or the injection of spin-polarized electrons into non-magnetic semiconductors. The latter is essential for the development of future electronic devices relying on the deliberate manipulation of electron spins (so-called spintronics) [50].

High-quality samples of II–VI materials required for practical devices are usually prepared by epitaxial growth techniques such as MBE, cf. Sec. 1.1. In order to obtain structures which satisfy the device-quality demands a detailed knowledge of the atomic mechanisms involved in the growth process is indispensable. In particular, the surface structure of a given material and its dependence on experimental conditions play a decisive role during the growth of thin films with sharp interfaces.

In the case of II–VI epitaxy surface reconstructions have a considerable impact on the growth process, and various experimental studies have addressed the question which reconstructions are present [51–54] and how experimental control parameters as temperature or particle flux influence the reconstructions [54–56]. For example, a temperature driven reordering of the surface atoms has been observed at Cd-terminated CdTe(001) surfaces [51, 54].

The majority of the cited studies has focused on the properties of CdTe and ZnSe, where a fairly complete qualitative overview over the surface phase diagram has been obtained, see e.g. [57, 58] for a review on the surface structure of CdTe. Additional knowledge about the chemical bonding of surface atoms and ground state energies of several reconstructions has been gained from density functional theory (DFT) calculations for both CdTe [22,23] and ZnSe [20,21,59]. For example, the results indicate that the two relevant surface reconstructions for Cd-terminated CdTe(001) surfaces are energetically nearly degenerate [22]. Within the framework of two-dimensional lattice gas simulations in thermal equilibrium it has been demonstrated that the above mentioned reordering of CdTe(001) surfaces can be traced back to the very small energy difference between the two reconstructions [11, 60, 61].

In the following we will investigate the influence of surface reconstructions under non-equilibrium growth conditions. We study a three-dimensional lattice gas model of II–VI(001) surfaces which extends the concepts developed by Ahr [11]. The (001) surface is of particular technological relevance as it frequently serves as substrate surface for epitaxy of II–VI compounds and heterostructures. We will focus on the description of CdTe(001), though many aspects of the considerations apply to other II–VI compounds like, e.g., ZnSe or ZnTe. Before presenting the model in Sec. 2.3 a brief review over known properties of CdTe(001) surfaces is given in the following.

2.1 Lattice Structure of CdTe

Like many other binary II–VI compounds CdTe crystallizes in the zincblende structure which basically consists of two interpenetrating face-centered cubic (fcc) lattices [39]. Each of the two sublattices is occupied by either only metal (Cd) or non-metal (Te) atoms. In the bulk, an atom of a given type is surrounded by four nearest neighbor (NN) atoms of the opposite type which form the corners of a tetrahedron, see Fig. 2.1.

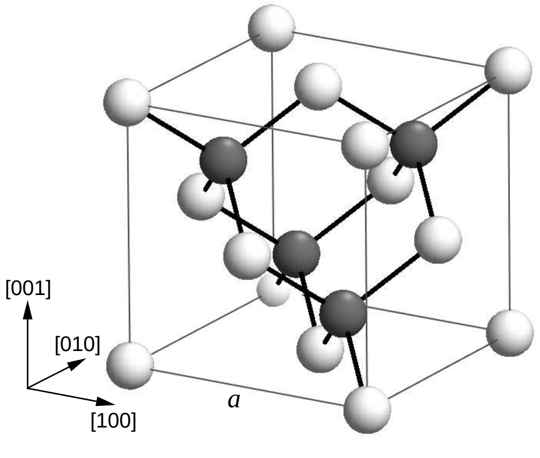

Figure 2.1: Unit cell of the zincblende structure of a CdTe crystal. Cd atoms are shown in dark gray, Te atoms are light gray. Bonds between nearest neighbor atoms are drawn as thick lines. a denotes the lattice constant.

If the CdTe crystal is viewed along the [001] direction, an alternation of Cd and Te layers can be observed. The ideal (001) surface would be obtained by merely cutting the crystal parallel to one of these layers [57]. In the absence of relaxation or reconstruction of the surface atoms the surface would thus be terminated by either a full monolayer (ML) of Cd or a full ML of Te, arranged in a two-dimensional square lattice of period $a/\sqrt{2}$. Here, $a = 0.648\,\mathrm{nm}$ denotes the lattice constant of the full three-dimensional zincblende structure, see Fig. 2.1.

For both Cd- and Te-terminated surfaces each atom in the topmost layer has two dangling bonds. The projection of these onto the (001) surface plane define the [110] direction (Cd dangling bonds) and the $[1\bar{1}0]$ direction (Te dangling bonds), respectively.

2.2 Reconstructions of CdTe(001) Surfaces

The geometric structure of a CdTe(001) surface, derived experimentally from, e.g., low energy electron diffraction (LEED) [53] or scanning tunneling microscopy (STM) [62] measurements, deviates from the ideal one where all surface atoms retain their bulk positions [57, 58]. This is due to the fact that, in general, the creation of a surface is energetically unfavorable and atoms at the surface attempt to reduce the surface excess energy by relaxation and reconstruction. While relaxation indicates the displacement of surface atoms along the surface normal, reconstruction includes lateral movements of the surface atoms, the incorporation of adatoms, or the creation of vacancies or dimers. For compound semiconductors like CdTe surface reconstructions are a common phenomenon and the stability of a given surface structure can be estimated by electron counting rules [63]. According to these, the number of available electrons in the surface layer should be distributed such that the anion (Te) dangling bonds at the surface are fully occupied whereas the cation (Cd) dangling bonds remain empty: the energy levels of the cation dangling bonds are located in or close to the conduction band whereas the ones of the Te dangling bonds are in or close to the valence band. Thus, the surface energy is lowered when an electron is transferred from a cation dangling bond to a Te dangling bond.

Figure 2.2 illustrates the relevant surface reconstructions of CdTe(001) which comply with the electron counting rule and are indeed observed experimentally. Figure 2.3 shows a schematic phase diagram of the surface structure as a function of temperature and particle fluxes in a typical MBE environment, following [57].

Under vacuum conditions and in the absence of particle deposition, the CdTe(001) surface is Cd-terminated. The surface is characterized by vacancy structures with limited Cd coverage $\theta^{\mathrm{Cd}} \leq 1/2$. At low temperatures one finds a dominant $c(2 \times 2)$ reconstruction which corresponds to a checkerboard-like occupation of the available square lattice sites [Fig. 2.2(left)]. Frequently, one observes a contribution of a (2×1) structure where the Cd atoms arrange in rows along the [110] direction which alternate with rows of vacancies [Fig. 2.2(middle)]. Note that in both arrangements lateral Cd neighbors along $[1\bar{1}0]$ do not occur as this would imply a local concentration of positive charges which is energetically extremely unfavorable. DFT calculations for zero temperature and $\theta^{\mathrm{Cd}} = 1/2$ have shown that the $c(2 \times 2)$ ordering has a slightly lower surface energy than the competing (2×1) structure [22, 23]. The calculated energy

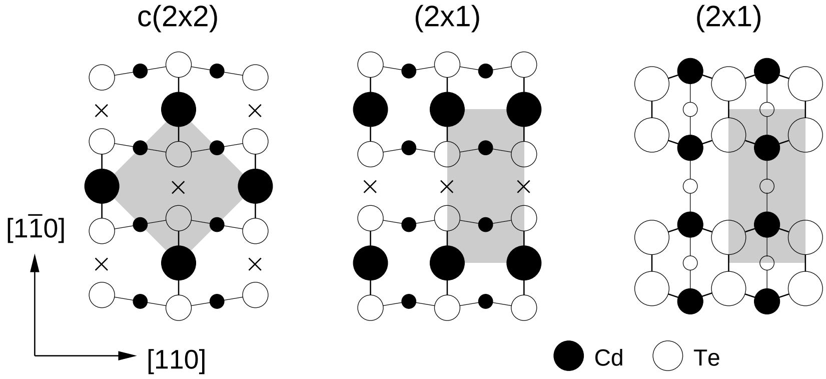

Figure 2.2: Schematic representation of the prevalent reconstructions of CdTe(001). These are the $c(2 \times 2)$ and (2×1) vacancy structures for the Cd-terminated surface (left and middle) and the (2×1) arrangement of Te dimers for the Te-terminated surface (right). Filled/empty circles represent Cd/Te atoms, their size corresponds to the height: the smaller the circle, the deeper the atom is buried. Crosses mark missing Cd atoms in the topmost layer, shaded areas denote the surface unit cells.

difference of $\Delta E \approx 16\,\text{meV}$ per (1×1) surface unit cell[1] accounts for spontaneous local transitions between the two reconstructions which were observed experimentally by STM measurements at room temperature [62, 64].

For temperatures $T \gtrsim 570\,\text{K}$ the surface is dominated *locally* by the (2×1) structure [54]. Despite the fact that significant sublimation sets in even below 570 K, the temperature driven reordering has been discussed in terms of an order-disorder phase transition in effective equilibrium by means of planar lattice gas models [11, 60, 61]: at low temperature, there is a long-range ordered Cd-rich phase with a $c(2 \times 2)$ reconstruction. At a critical temperature the Cd atoms lose their long-range order and arrange preferentially in a (2×1) pattern. The results are consistent with the experimental observation of small (2×1) domains which indicate a high degree of disorder [54].

In the presence of a stationary Cd flux the $c(2 \times 2)$ structure can be stabilized at temperatures above the transition in vacuum [51, 57]. On the other hand, a steady deposition of Te stabilizes Te-terminated surfaces [51, 57]: at relatively small fluxes and high temperatures a Te coverage $\theta^{\text{Te}} \approx 1$ is observed, hence there is no vacancy structure as for Cd-terminated surfaces. The Te atoms arrange in rows of dimers along the [110] direction at the surface, corresponding to a (2×1) reconstruction pattern [Fig. 2.2(right)].

At high Te flux and low temperatures Te coverages $\theta^{\text{Te}} \approx 3/2$ with a (2×1) surface symmetry are observed, cf. Fig. 2.3. The evaporation of terminating Te layers after ending deposition has been studied in different temperature regimes and the analysis of the corresponding Arrhenius plots suggests the presence of a very weak binding of excess Te [51, 57, 58]. It has been hypothesized that additional Te atoms are introduced

---

[1] Similar calculations for a Zn-terminated ZnSe(001) surface yield a higher value of $\Delta E \approx 30\,\text{meV}$ per (1×1) unit cell [20, 21].

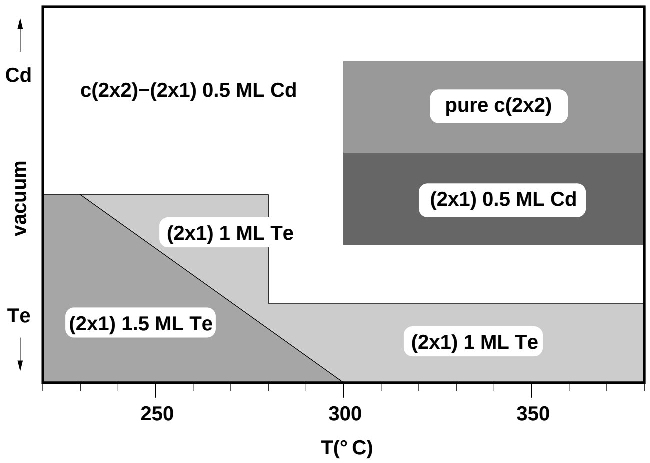

Figure 2.3: Schematic surface phase diagram of CdTe under typical MBE conditions according to [57]. Shown are the prevalent reconstructions and the corresponding surface coverage as function of temperature and particle flux. The middle part corresponds to vacuum conditions, upper and lower part display the situation under Cd and Te flux, respectively.

into dimers, thus forming trimers [51, 55, 57]. On the contrary, high resolution STM images of the (2×1) Te-stabilized surface [65] indicate the presence of physisorbed Te_2 molecules on the surface which might also account for Te coverages $\theta^{Te} > 1$. However, the precise mechanism of binding the excess Te to the surface remains unknown [58].

The presence of excess Te is of particular importance, e.g., for the explanation of the temperature dependent growth rate of CdTe in atomic layer epitaxy (ALE), cf. Chap. 3. In principle, a growth rate of one complete layer of CdTe per ALE cycle could be achieved. However, in a wide range of temperatures, one observes a growth rate of at most 1/2 layer per ALE cycle [66, 67]. This limitation reflects the restricted coverage of Cd-terminated surfaces. Only for sufficiently low temperatures one finds the expected rate of approximately one layer per cycle, with a temperature driven, sudden transition from one regime to the other [66, 67]. In the lattice gas model presented below we will account for additional weakly bound Te atoms in an effective way, and we will explain how the presence of these weakly bound atoms allows to overcome the growth rate limitation.

2.3 Lattice Gas Model

In the following we describe the three-dimensional lattice gas model of II–VI(001) semiconductor surfaces which accounts for both the correct zincblende structure of the material systems and the relevant surface reconstructions of Cd- and Te-terminated surfaces.

2.3.1 Representation of the Crystal Structure

In our model we exclude the incorporation of defects or vacancies into the crystal. Then the zincblende structure (Fig. 2.1) can be represented in a solid-on-solid (SOS) manner,

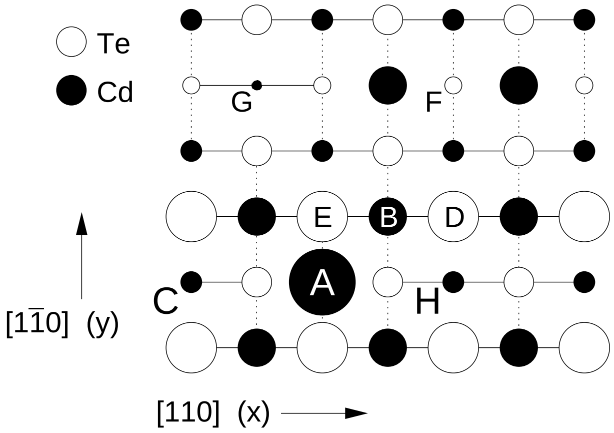

Figure 2.4: Solid-on-solid representation of the zincblende lattice. Filled/empty circles represent Cd/Te atoms, their size corresponds to the height. Dotted lines denote bonds of Cd to Te atoms in the layer below, solid lines link Te with underlying Cd. Only bonds between visible atoms are displayed.

cf. Sec. 1.3.1. We use cartesian coordinates where the [110], [1$\bar{1}$0] and [001] directions define the x-, y- and z-axis, respectively. If the zincblende lattice is projected onto the x-y plane in the z-direction, the images of all atoms are located on a square lattice (cf. Fig. 2.4) with lattice constant $a/(2\sqrt{2})$. Again, a denotes the lattice constant of the full zincblende structure, cf. Fig. 2.1. If we measure all distances in appropriate units and assume that the origin of our coordinate system is at the center of a Te atom then the images of Te atoms lie at (i,j) in the x-y plane with integer values i,j and $i+j$ *even*. Conversely, the images of Cd atoms are located at (i',j') with $i'+j'$ *odd*, see Fig. 2.4.

In our SOS representation the (001) surface now is described by a two-dimensional $2N_x \times 2N_y$ array $h(x,y)$ of integers. Each value $h(x,y)$ corresponds to the maximal z-coordinate or, loosely speaking, height of the column of atoms whose images lie at (x,y), measured in units of the spacing between a Cd and a Te layer.

An atom in the zincblende lattice may have at most four binding partners, see Fig. 2.1. Due to the SOS condition, each atom must have at least two bonds to NN atoms of the opposite species in the layer below: an atom with only one bond would form an overhang which is not allowed in an SOS model.

An atom with exactly two bonds may be removed from the crystal without violating the SOS condition and is considered as *mobile* in the following. A Cd atom at (x,y) is bound to Te atoms at $(x,y\pm 1)$ in the layer below and can be bound to Te atoms at $(x\pm 1,y)$ in the layer above, see Fig. 2.4. The atom is mobile if it has no bonds to Te atoms in the layer above which implies $h(x,y) > h(x\pm 1,y)$. For example, the Cd atom labeled “A” in Fig. 2.4 is mobile. For a Te atom at (x',y'), a similar consideration yields $h(x',y') > h(x',y'\pm 1)$ as condition for mobility, which is fulfilled for, e.g., the Te atom labeled “D” in Fig. 2.4.

On the other hand, removing an atom with three or four bonds would create an overhang or a vacancy, respectively, and is thus forbidden: the corresponding atom is considered as *immobile*. Examples for immobile atoms in Fig. 2.4 are the Cd atom “B” with four bonds and the Te atom “E” with three bonds.

Similarly, an atom may be deposited only at sites where it forms exactly two bonds to the atoms in the layer below. Deposition at sites with only one bond would create an overhang whereas the formation of three or four bonds during deposition implies the presence of an overhang or a vacancy, respectively, which do not occur in the SOS model. As a consequence, the diffusion process of a mobile atom which is removed from one site and deposited at another cannot change the number of chemical bonds in the system.

An atom can be deposited at a site if the SOS condition is fulfilled and the atomic species matches the character of the site. At a Cd site at (x, y), the SOS condition requires $h(x, y-1) = h(x, y+1)$ and $h(x, y) < h(x, y \pm 1)$. A Te site at (x', y') can be occupied if $h(x'-1, y') = h(x'+1, y')$ and $h(x', y') < h(x' \pm 1, y')$. The deposition of an atom at (x, y) is performed by setting $h(x, y) \leftarrow h(x, y) + 4$. Similarly, setting $h(x, y) \leftarrow h(x, y) - 4$ removes the atom at (x, y). In Fig. 2.4 for instance sites "C", "G", and "H" are available for Cd deposition whereas "F" can be occupied by a Te atom.

The positions of the atoms in *one layer* of the zincblende lattice lie on a square lattice. Note that the distance between nearest neighbor atoms in this square lattice (denoted as *lateral nearest neighbors* in the following) is *twice* the distance between neighboring images of atoms in the projection of the *whole* crystal onto the x-y plane, see Fig. 2.4. Accordingly, lateral nearest neighbors are separated by $a/\sqrt{2}$ with a from above.

In addition to $h(x, y)$ which basically describes the positions of the atoms a second array $d(x, y)$ is used to store the reconstruction of Te terminated surfaces. The array value $d(x, y)$ denotes the dimerization of a Te atom by giving the direction in which the dimer bond is formed: $d(x, y) = \pm 1$ corresponds to a Te atom at (x, y) which is shifted toward the lateral NN Te atom at $(x, y \pm 2)$, see Fig. 2.5, whereas $d(x, y) = 0$ corresponds to an undimerized Te atom. A similar scheme has been applied by Rockett *et al.* [68, 69] for the representation of Si dimers in simulations of epitaxial growth on Si(001) surfaces. Note that Te dimers are always oriented along the y-direction. A Te dimer is thus characterized by a d value of $+1$ for one Te atom and -1 for the other. As a consequence, a Te atom can be involved in at most one dimer. Te dimerization introduces additional degrees of freedom to the model without changing the topology of the lattice.

2.3.2 Energetics

A faithful representation of the crystal energetics would certainly require the implementation of long-range interactions as well as interactions which depend on the simultaneous occupation of three or more lattice sites. In order to make the simulation of our model feasible we make the reasonable assumption that the dominant contribution to the total binding energy stems from the chemical bonds between nearest neighbors of Cd and Te, and further (effective) short-ranged pair interactions between lateral nearest neighbors and lateral diagonal neighbors in the same layer, see Fig. 2.5. The interaction strengths are chosen such that essential properties of the system are reproduced, e.g., the termination of the surface with Cd under vacuum conditions and the reconstructions of Cd- and Te-terminated surfaces, see Fig. 2.2.

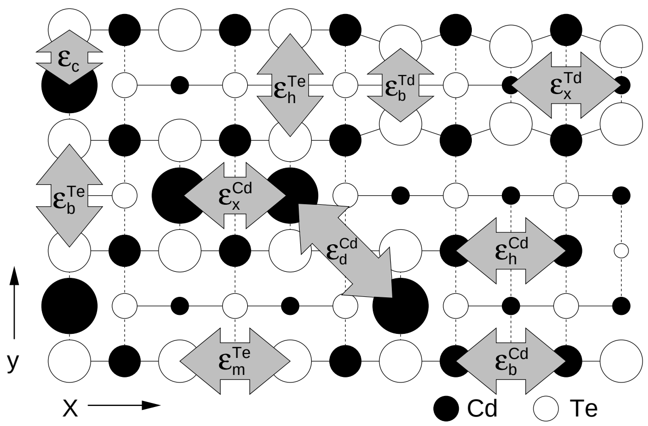

Figure 2.5: Particle interactions in the lattice gas model as described in the text. Filled/empty circles correspond to Cd/Te atoms. Te dimers are represented by smaller distances between lateral nearest neighbors in the y-direction.

Every Cd–Te bond in the system contributes an energy $\varepsilon_c < 0$, the sum of which representing the greatest part of the total binding energy of the crystal. The crystal structure is further stabilized by effective, isotropic intra-layer interactions $\varepsilon_b^{\mathrm{Cd}}$ and $\varepsilon_b^{\mathrm{Te}}$ between lateral nearest neighbor pairs of two immobile Cd or Te atoms, respectively. For pairs of one mobile and one immobile atom of the same species we introduce interactions $\varepsilon_h^{\mathrm{Cd}}$ (Cd–Cd) and $\varepsilon_h^{\mathrm{Te}}$ (Te–Te) which shall also be isotropic.

As in the planar lattice gas models studied in [60, 61] an infinite repulsion excludes lateral NN pairs of mobile Cd in y-direction at the surface, owing to the fact that neighboring Cd atoms in $[1\bar{1}0]$ direction are not observed in the $c(2 \times 2)$ and (2×1) reconstructions (cf. Fig. 2.2). An attractive interaction $\varepsilon_x^{\mathrm{Cd}} < 0$ between lateral NN of mobile Cd in x-direction and a competing interaction $\varepsilon_d^{\mathrm{Cd}} < 0$ between lateral diagonal neighbors favor the (2×1) or $c(2\times2)$ arrangement, respectively. As demonstrated in [60, 61], the temperature dependence of the Cd reconstruction is reproduced qualitatively if $\left|\varepsilon_x^{\mathrm{Cd}}\right| \lesssim 2 \left|\varepsilon_d^{\mathrm{Cd}}\right|$ holds.

Lateral NN pairs of mobile Te which do not form a dimer contribute an energy $\varepsilon_m^{\mathrm{Te}} < 0$, whereas the energy $\varepsilon_b^{\mathrm{Td}} < \varepsilon_m^{\mathrm{Te}}$ is assigned to a pair which forms a dimer, reflecting the energy gain due to dimerization. Pairwise interactions $\varepsilon_x^{\mathrm{Td}}$ of neighboring dimers in x-direction favor their arrangement in rows along [110], corresponding to a (2×1) surface symmetry.

2.3.3 Reservoir of Weakly Bound Te

In addition to Te particles at regular SOS lattice sites, we include the capture of Te atoms in a weakly bound state, denoted as Te* atoms in the following. The energy contribution of each Te* atom is ε^* with $|\varepsilon^*| < 2\,|\varepsilon_c|$. The latter accounts for the fact that the binding of a Te* is weaker compared to that of an isolated mobile atom at a regular lattice site which has two Cd–Te bonds of strength ε_c.

Following an earlier hypothesis [51, 57] these weakly bound Te* might be associated with atoms which occupy Cd sites temporarily and hence form a Te trimer [11]. However, as already mentioned in Sec. 2.2 the precise nature of the Te* is still unknown. In this work, we abandon the assumption of Te trimers and instead include Te* particles in an effective fashion.

We introduce a reservoir of Te* with $n^* = \theta^* N_x N_y$ particles, where $N_x N_y$ is the number of atoms in one complete bulk layer of Te. The total reservoir occupation θ^* is composed of two parts: $\theta^* = \theta^*_{loc} + \theta^*_{mob}$. The quantity θ^*_{loc} accounts for the fraction of Te* which are *localized* on top of mobile Cd and thus neutralize the infinite repulsion between Cd lateral NN in y-direction [11]. This effect will be discussed in more detail in Sec. 2.3.5. Localized Te* are represented by a two-dimensional $2N_x \times 2N_y$ array $l(x, y)$: a Te* atom which sits on top of a Cd atom at (x, y) corresponds to $l(x, y) = 1$, otherwise $l(x, y) = 0$.

On the contrary, θ^*_{mob} corresponds to the remaining Te* atoms which are highly *mobile* and no assumption is made about their precise location and the nature of the binding. In general, during our simulations $\theta^*_{loc} \ll \theta^*_{mob}$ holds for most of the time.

For the calculation of the overall Te coverage besides mobile Te atoms at regular lattice sites also localized and mobile Te* atoms are taken into account. According to the experimentally observed range of Te coverages [57,58] the total reservoir occupation thus is restricted to values $0 \leq \theta^* \leq 1/2$. In our model we will exclude larger values by a simple cut-off: if θ^* has reached its maximum value 1/2 all processes leading to an increase of θ^* are forbidden, i.e. their rate is set to zero.

We furthermore assume that an attractive pairwise interaction between Te* atoms stabilizes the reservoir. In a mean field fashion we represent the latter by an energy contribution $\varepsilon^*_b \, \theta^* \, n^*$ with parameter $\varepsilon^*_b < 0$.

In summary, the total energy of a given configuration can be written as

$$\begin{aligned} H &= \varepsilon_c \, n_c + \varepsilon_b^{\mathrm{Cd}} \, n_b^{\mathrm{Cd}} + \varepsilon_b^{\mathrm{Te}} \, n_b^{\mathrm{Te}} + \varepsilon_h^{\mathrm{Cd}} \, n_h^{\mathrm{Cd}} + \varepsilon_h^{\mathrm{Te}} \, n_h^{\mathrm{Te}} \\ &+ \varepsilon_x^{\mathrm{Cd}} \, n_x^{\mathrm{Cd}} + \varepsilon_d^{\mathrm{Cd}} \, n_d^{\mathrm{Cd}} + \varepsilon_m^{\mathrm{Te}} \, n_m^{\mathrm{Te}} \\ &+ \varepsilon_b^{\mathrm{Td}} \, n_b^{\mathrm{Td}} + \varepsilon_x^{\mathrm{Td}} \, n_x^{\mathrm{Td}} \\ &+ \varepsilon^* \, n^* + \varepsilon_b^* \, \theta^* \, n^*, \end{aligned} \tag{2.1}$$

which depends on the number of Cd–Te bonds (n_c), bulk lateral NN pairs of Cd (n_b^{Cd}) and Te (n_b^{Te}), lateral NN pairs of one mobile and one immobile Cd (n_h^{Cd}) or Te (n_h^{Te}), lateral NN and NNN pairs of mobile Cd at the surface (n_x^{Cd} and n_d^{Cd}), and lateral NN pairs of mobile Te not forming a dimer (n_m^{Te}). The number of Te dimers is denoted as n_b^{Td}, whereas n_x^{Td} counts pairs of neighboring Te dimers along the x-direction. The last line in Eq. (2.1) accounts for the contribution of the Te* reservoir which is occupied by n^* atoms. Additionally, we consider only surface configurations where the number of lateral y-neighbors of mobile Cd atoms without a localized Te* atom is zero.

2.3.4 Dynamics and Growth

As we are interested in the non-equilibrium dynamics of the system under sublimation or growth conditions, specifying the energy of a given configuration is not sufficient. In fact, only the energy contribution of a few active layers which contain mobile particles will be relevant in the following. The kinetics of the system is governed by the energy barriers which have to be overcome in thermally activated transitions between the different configurations, cf. Sec. 1.2.3.

So far, the available experimental data and first principles results are not sufficient for a systematic fit of our model parameters. In particular, reliable evaluations or estimates of, e.g., diffusion barriers are not available, apart from very few exceptions. Therefore, we do not aim at a precise quantitative description of the CdTe(001) surface.

Nevertheless, essential features can be deduced from experimental data and physical insight. Important qualitative features of the model turn out to be quite robust against variations of the parameters, as long as they comply with some essential conditions. In our simulations we will use a parameter set which is based on previous investigations of related models and their comparison with experimental findings [11, 70]. There, the observed temperature dependent structure of Cd-terminated surfaces under step-flow sublimation has been reproduced qualitatively by appropriate choice of the parameter set. Furthermore, a semi-quantitative match of, e.g., the reordering temperature and macroscopic sublimation rates has been achieved [11, 70].

The microscopic processes incorporated in our kinetic Monte Carlo simulations are deposition of adatoms, diffusion and desorption of mobile atoms, transitions of Te atoms between regular lattice sites and the reservoir, and desorption of reservoir atoms.

We consider only the deposition of single atoms, although in experimental systems Te probably arrives as binary molecule at the surface. The deposition of a Cd or Te atom occurs via an incorporation process: first, the particle type and a lattice site are chosen randomly. Then, a search is performed within an incorporation radius r_{inc} for the site with the lowest height where deposition is possible [4, 6]. If this is, for a Cd atom, a site with a neighboring mobile Cd atom in y-direction, deposition is only possible if there is either a localized Te* on top of the Cd neighbor, already, or a mobile Te* attaches to the impinging Cd. The latter occurs with probability θ^*_{mob}.

For a Te atom proper adsorption sites include, besides regular Te sites, mobile Cd atoms with no localized Te* attached as well as empty Cd sites. In the latter two cases, the Te atom becomes a mobile reservoir Te* with probability $1 - 2\theta^*$ which is zero for $\theta^* = 1/2$ as required. With probability $2\theta^*$ deposition is rejected and the particle evaporates. As a consequence, the reservoir occupation is limited to values $\theta^* \leq 1/2$.

The rates for all thermally activated processes are of the Arrhenius form

$$R = \alpha \, \nu \, \exp\left(-\frac{E_a}{k_B T}\right), \tag{2.2}$$

where E_a and ν denote the activation energy and attempt frequency for a given process, respectively. The prefactor α accounts for rates which depend explicitly on the reservoir occupation, see Table 2.1 and the discussion in Sec. 2.3.5.

The desorption of mobile atoms from regular lattice sites or mobile Te* from the reservoir requires an activation energy $E_a = \Delta H$ where ΔH denotes the energy difference between the initial and the final system configuration and is given by Eq. (2.1). As in the modeling of a deposition process we consider only desorption of single atoms,

process	α	ν	E_a
Cd or Te diffusion	1	ν_o	$\max\{B_o, B_o + \Delta H\}$
Cd diffusion (Te* involved)	θ^*_{mob}	ν_o	$\max\{B_o, B_o + \Delta H\}$
Cd or Te desorption	1	ν_o	ΔH
Te $\rightarrow$ Te$^*_{mob}$	$1 - 2\theta^*$	ν_o	$\max\{B_o, B^* + \Delta H\}$
Te $\rightarrow$ Te$^*_{loc}$	$1 - 2\theta^*$	ν_o	$\max\{B_o, B^* + \Delta H\}$
Te$^*_{mob}$ $\rightarrow$ Te	θ^*_{mob}	ν^*	$\max\{B^*, B_o + \Delta H\}$
Te$^*_{loc}$ $\rightarrow$ Te	1	ν^*	$\max\{B^*, B_o + \Delta H\}$
Te$^*_{mob}$ desorption	θ^*_{mob}	ν^*	ΔH

Table 2.1: Thermally activated processes and corresponding values of attempt frequencies ν, prefactors α and activation energies E_a used for calculating the Arrhenius rates [Eq. (2.2)] as described in the text.

neglecting the fact that Te probably evaporates from the surface in the form of Te_2 molecules, in reality.

Diffusion of mobile atoms at the surface and transitions of Te atoms between regular SOS sites and the reservoir are modeled using Kawasaki-type energy barriers (cf. Sec. 1.4.2)

$$E_a = \max\{B_i, B_f + \Delta H\}. \tag{2.3}$$

Here, the barriers B_i and B_f, corresponding to the initial and final configuration, respectively, depend on the type of process, and the energy difference ΔH is, again, given by Eq. (2.1).

For all diffusion steps we use equal barriers $B_i = B_f = B_o$ in Eq. (2.3) similar to earlier studies [11,70]. A mobile particle at site $\vec{x} = (x, y)$ may diffuse to all available lateral NN or lateral diagonal neighbor sites $\vec{x}' = (x', y')$ in the same layer provided the SOS and other conditions are fulfilled. This corresponds to the following set of hopping vectors $\Delta\vec{x} = \vec{x}' - \vec{x}$: $\Delta\vec{x} \in \{(2,0), (-2,0), (0,2), (0,-2), (2,2), (-2,2), (2,-2), (-2,-2)\}$ For example, the Cd atom “A” in Fig. 2.4 may jump to one of the lateral NN sites “C” or “H”, corresponding to hopping vectors $\Delta\vec{x} = (-2,0)$ and $\Delta\vec{x} = (2,0)$, respectively, whereas the Te atom “D” may jump to site “F”, corresponding to $\Delta\vec{x} = (0,2)$. With the above defined set of hopping vectors it is not yet possible for a particle to cross a step without violating the SOS condition. For example, in Fig. 2.4 the nearest site to “A” available for Cd deposition on the lower terrace is “G” which corresponds to a hopping vector $\Delta\vec{x} = (-1,3)$. By symmetry considerations we obtain $\{(3,1), (-3,1), (3,-1), (-3,-1), (1,3), (-1,3), (1,-3), (-1,-3)\}$ as the minimal set of additional hopping vectors which enable the crossing of steps of one monolayer height oriented in arbitrary direction [11]. If steps higher than one monolayer were to cross we would have to incorporate further hopping vectors which would increase the complexity of the model significantly. Since steps of two or more monolayers height rarely occur in our simulations, neglecting diffusion across such high steps is not a severe restriction.

A mobile Te atom at the surface may enter the Te* reservoir provided the reservoir is not full, that is $\theta^* \leq 1/2$. The assumption that Te* atoms are less strongly bound than Te atoms at regular surface sites implies $B_i = B_o$ and $B_f = B^* < B_o$ in Eq. (2.3) for the transition of a Te atom into the reservoir. Conversely, $B_i = B^*$ and $B_f = B_o$ hold for the opposite process, see Table 2.1.

For all diffusion processes and the desorption of mobile atoms at regular surface sites we assume a common attempt frequency $\nu_o = 10^{12}\,\mathrm{s}^{-1}$ whereas a lower frequency ν^* is used for the transition of Te* atoms to regular Te states and the evaporation of mobile Te*. This choice is based on the reasonable assumption that Te* atoms reside in potential energy minima which are much shallower than those for Te atoms at regular surface sites [7]. According to transition state theory the attempt frequency ν^* which corresponds to the harmonic oscillation frequency at the local energy minimum will become smaller [29, 38]. A similar argument has been used by Itoh [71] in order to motivate an attempt frequency of weakly bound arsenic as low as $10^8\,\mathrm{s}^{-1}$ in simulations of InAs(001). In our simulations, the choice of a lower frequency ν^* can be further motivated by comparison with experimental observations as will be discussed in Chap. 3.

The formation or breaking of dimers from lateral NN pairs of mobile Te atoms is taken into account implicitly. A diffusion hop of a Cd atom onto a Te dimer, for instance, requires the breaking of the dimer which has to be considered in the energy balance ΔH of the process. The deposition of a Cd atom will always break all underlying Te dimers involved. On the other hand, dimer formation is assumed to occur instantaneously, whenever it is possible due to the resulting energy gain. A similar simplification has been used before for the description of Si-dimerization on Si(001) surfaces [68, 69]. Hence, if any event results in two undimerized Te atoms which are in the correct configuration for forming a dimer pair, a dimer bond will be created immediately. If there is more than one possible dimerization, the configuration with the lowest total energy [Eq. (2.1)] will be chosen.

2.3.5 The Role of Te* Atoms

The existence of a weakly bound state for Te atoms is essential to facilitate growth in our model. For example, consider a Cd-terminated surface with $c(2 \times 2)$ reconstruction and maximum coverage $\theta^{\mathrm{Cd}} = 1/2$. Clearly, deposition of Te at a regular lattice site would violate the SOS condition. On the other hand, the incorporation of additional Cd is impossible due to the infinite repulsion of lateral nearest neighbors in y-direction, see Fig. 2.6(a).

It is plausible to assume, however, that an additional Te bound to a Cd would neutralize the repulsion as it provides three negatively charged dangling bonds. Such Te atoms which stay *on top* of mobile Cd atoms are treated as part of the Te* reservoir where they form the fraction θ^*_{loc} of localized Te* atoms, cf. Sec. 2.3.3. In our model, mobile Cd atoms can hop to empty sites neighboring another mobile Cd in y-direction, provided there is either already a localized Te* on top of the neighboring Cd, or a *mobile* Te* attaches to the diffusing Cd atom. This Te* then would become a localized Te*

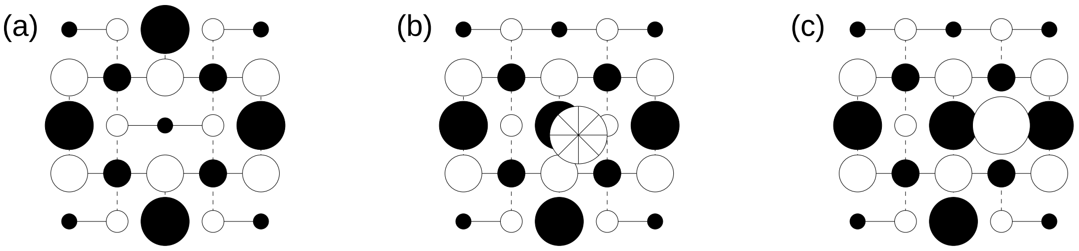

Figure 2.6: Incorporation of a Te atom on a $c(2 \times 2)$ reconstructed surface through mediation of the Te* reservoir. (a) In the absence of appropriate SOS sites, newly deposited Te atoms will occupy mobile Te* states. (b) A mobile Te* attaches to the Cd atom which has jumped to the center lattice site and becomes a localized Te* (open circle with a star inside) neutralizing the infinite repulsion. (c) The localized Te* from (b) gets incorporated at the right adjacent regular SOS site.

itself, see Fig. 2.6(b).

The latter process is assumed to happen with a probability θ^*_{mob} which is reflected in the prefactor α of the corresponding rate [Eq. (2.2)], see Table 2.1. Thus, we assume that mobile Te* which are not attached to Cd atoms are available instantaneously everywhere at the surface. Note that after the diffusion step of the Cd atom the reservoir occupation $\theta^* = \theta^*_{loc} + \theta^*_{mob}$ remains the same while the ratio $\theta^*_{loc}/\theta^*_{mob}$ has *increased.* If at any point of the simulation a localized Te* is no longer needed it will become a mobile Te* again. For example, consider the backward process in Figs. 2.6(b) and (a): if the center Cd atom in Fig. 2.6(b) makes a diffusion hop to the lateral nearest neighbor site in positive y-direction, the localized Te* is no longer required and thus joins the fraction of mobile Te* atoms, see Fig. 2.6(a). Hence, the ratio $\theta^*_{loc}/\theta^*_{mob}$ *decreases* leaving θ^* unchanged, though.

Through the mediation of Te* atoms, Cd atoms at the surface can coalesce into islands in spite of the NN repulsion, provided the reservoir of Te* is not empty. Thus the completion of Cd layers can be achieved during growth.

In our simulations we consider also transitions of Te between regular lattice sites and reservoir states as well as the desorption of mobile Te* into the vacuum. All of these processes change the reservoir occupation and in general, the rates also depend explicitly on the reservoir occupation, i.e. $\alpha \neq 1$ (see Table 2.1).

For instance, mobile Te atoms at the surface may become mobile Te* provided the reservoir is not fully occupied, i.e. $\theta^* < 1/2$. This happens with a rate according to Eq. (2.2) with $\alpha = 1 - 2\theta^*$ which is zero if the reservoir density has reached its maximum value 1/2. Conversely, the rates for transition of a mobile Te* to a regular Te state or desorption of a mobile Te* are proportional to the density θ^*_{mob} of mobile Te* atoms.

A localized Te* atom which sits on top of a Cd atom at (x, y) may become bound at one of the two neighboring regular Te sites at $(x \pm 1, y)$, if available, see Figs. 2.6(b) and (c). This reduces the density θ^*_{loc} and consequently also θ^*. The opposite process is possible for a suitable configuration, again under the condition that $\theta^* < 1/2$.

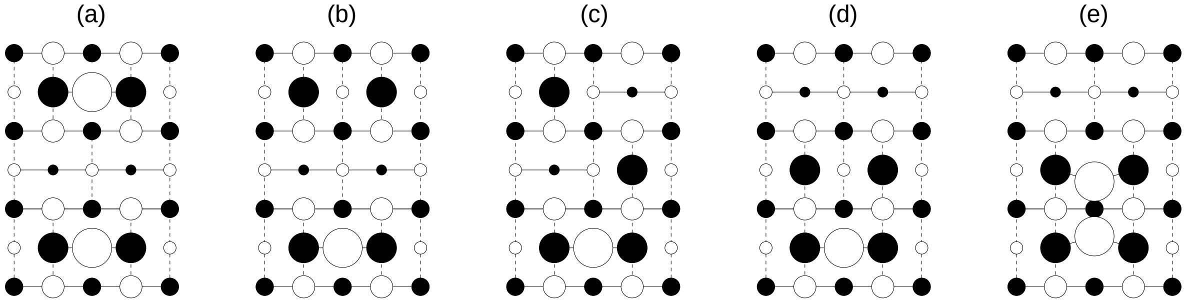

Figure 2.7: Coalescence of two small islands through mediation of the Te* reservoir. The Te atom from the upper island in (a) enters the Te* reservoir (b) and the Cd atoms diffuse towards the lower island (c),(d). Then, a mobile Te* of the reservoir gets incorporated at the newly created SOS lattice site and forms a dimer bond with the Te atom of the lower island (e).

The corresponding prefactor in Eq. (2.2) is $\alpha = 1 - 2\theta^*$. As an example, the Te atom in Fig. 2.6(c) may jump on top of the center Cd atom, restoring the configuration of Fig. 2.6(b).

The availability of Te* states is also important for preserving the ergodicity of our model. Consider for example the surface configuration in Fig. 2.7(a): the merging of the two small islands would be energetically favorable due to the increased number of attractive bindings (two additional Cd–Cd bonds plus one dimer bond), see Fig. 2.7(e). However, in the absence of a Te flux it is not possible to construct a sequence of single particle moves on the SOS lattice which leads from (a) to (e) without violating the SOS condition: neither of the Cd atoms of the islands in Fig. 2.7(a) may jump away for this would lead to an Te atom forming an overhang. On the other hand, a Te atom that jumped off the island would land in the wrong sublattice which is not allowed. With the help of the Te* reservoir the coalescence of the two islands can now be achieved: the Te atom of the upper island in Fig. 2.7(a) temporarily enters a mobile Te* state [Fig. 2.7(b)]. Then, the two Cd atoms can diffuse towards the lower island [Figs. 2.7(c) and (d)]. Finally, a mobile Te* atom may become incorporated at the SOS lattice site provided by the two Cd atoms [Fig. 2.7(e)].

2.3.6 Surface Characterization

For the characterization of the surface we calculate the average surface height

$$\langle h \rangle = \frac{1}{4N_xN_y} \sum_{x,y=1}^{2N_x,2N_y} h(x,y). \tag{2.4}$$

Furthermore, the surface coverage with Cd or Te is determined. To this end, we introduce two $2N_x \times 2N_y$ arrays $c(x,y)$ and $t(x,y)$ of integers which denote the *mobile* Cd and Te atoms: $c(x,y) = 1$ if a mobile Cd atom is located at site (x,y) and zero otherwise. Conversely, $t(x,y) = 1$ holds for a mobile Te atom at (x,y) whereas $t(x,y) = 0$

in all other cases. The Cd and Te coverages are then defined as

$$\theta^{\mathrm{Cd}} = \frac{1}{N_x N_y} \sum_{x,y=1}^{2N_x,2N_y} c(x,y), \tag{2.5}$$

$$\theta^{\mathrm{Te}} = \frac{1}{N_x N_y} \sum_{x,y=1}^{2N_x,2N_y} t(x,y). \tag{2.6}$$

Additionally, we determine the reservoir occupation $\theta^* = (n^*_{mob} + n^*_{loc})/(N_x N_y)$ where n^*_{mob} denotes the number of mobile Te* atoms and the number n^*_{loc} of localized Te* is given by $n^*_{loc} = \sum_{x,y=1}^{2N_x,2N_y} l(x,y)$ with the array $l(x,y)$ defined in Sec. 2.3.3.

In order to quantify the contribution of the Cd reconstructions we consider the pair correlations

$$K_x^{\mathrm{Cd}} = \frac{1}{\theta^{\mathrm{Cd}} N_x N_y} \sum_{x,y=1}^{2N_x,2N_y} c(x,y)c(x+2,y), \tag{2.7}$$

$$K_d^{\mathrm{Cd}} = \frac{1}{2\theta^{\mathrm{Cd}} N_x N_y} \sum_{x,y=1}^{2N_x,2N_y} c(x,y)\left[c(x+2,y+2) + c(x+2,y-2)\right] \tag{2.8}$$

which measure the probability to find two mobile Cd atoms occupying lateral NN sites in the x-direction or lateral diagonal neighbor sites, respectively. K_x^{Cd} and K_d^{Cd} are normalized by the Cd coverage such that they are equal to the fraction of mobile Cd atoms which are part of locally (2×1) or $c(2 \times 2)$ reconstructed regions of the surface.

2.3.7 Parameter Estimation

As mentioned above, the experimental data and first principles results are insufficient for a systematic fit of the model parameters. Therefore any parameter set will, to some extent, be based on estimates and physical reasoning. In our simulations we focus on the following parameter set which reflects the results obtained from previous investigations [11, 60, 61]: $r_{inc} = 2$, $\varepsilon_x^{\mathrm{Cd}} = -1.95|\varepsilon_d^{\mathrm{Cd}}|$, $\varepsilon_b^{\mathrm{Cd}} = \varepsilon_b^{\mathrm{Te}} = \varepsilon_h^{\mathrm{Te}} = -0.8|\varepsilon_d^{\mathrm{Cd}}|$, $\varepsilon_h^{\mathrm{Cd}} = 0$, $\varepsilon_m^{\mathrm{Te}} = -0.6|\varepsilon_d^{\mathrm{Cd}}|$, $\varepsilon_b^{\mathrm{Td}} = -1.0|\varepsilon_d^{\mathrm{Cd}}|$, $\varepsilon_x^{\mathrm{Td}} = -0.4|\varepsilon_d^{\mathrm{Cd}}|$, $\varepsilon_c = -6.5|\varepsilon_d^{\mathrm{Cd}}|$, $\varepsilon^* = -5|\varepsilon_d^{\mathrm{Cd}}|$, $\varepsilon_b^* = -8|\varepsilon_d^{\mathrm{Cd}}|$, $B_o = 7|\varepsilon_d^{\mathrm{Cd}}|$, $B^* = 2|\varepsilon_d^{\mathrm{Cd}}|$. The motivation of this choice follows the outline given in [11]: the interaction between lateral diagonal neighbors of mobile Cd is attractive, which is reflected in a negative value of $\varepsilon_d^{\mathrm{Cd}}$. For a mobile Cd atom in a $c(2 \times 2)$ domain the interaction with its four lateral diagonal neighbor atoms amounts to $-4|\varepsilon_d^{\mathrm{Cd}}|$. On the other hand, Cd atoms which are part of the (2×1) arrangement have two lateral nearest neighbors yielding $2\varepsilon_x^{\mathrm{Cd}}$. The choice $\varepsilon_x^{\mathrm{Cd}} = -1.95|\varepsilon_d^{\mathrm{Cd}}|$ ensures that the $c(2 \times 2)$ vacancy structure is energetically favorable compared to (2×1) and that the difference between the surface energies of the two reconstructions—which is $|2\varepsilon_d^{\mathrm{Cd}} - \varepsilon_x^{\mathrm{Cd}}|/2$ per (1×1) surface unit cell—is small compared to the total surface energy. The parameters $\varepsilon_b^{\mathrm{Cd}}$, $\varepsilon_b^{\mathrm{Te}}$, $\varepsilon_h^{\mathrm{Te}}$, $\varepsilon_h^{\mathrm{Cd}}$, $\varepsilon_m^{\mathrm{Te}}$, $\varepsilon_b^{\mathrm{Td}}$, $\varepsilon_x^{\mathrm{Td}}$ are chosen such that under vacuum a

Cd terminated surface with $c(2 \times 2)$ reconstruction is obtained at low temperatures. By comparing the activation energy for desorption of a mobile Cd from a (2×1) domain with the activation energy for desorption of a Te atom from a (2×1) dimer arrangement, we obtain $2\varepsilon_x^{\mathrm{Cd}} < 3\varepsilon_m^{\mathrm{Te}} + \varepsilon_b^{\mathrm{Td}} + 2\varepsilon_x^{\mathrm{Td}}$ as approximate condition for the stability of the Cd termination under vacuum. The dimer interaction $\varepsilon_b^{\mathrm{Td}}$ should be stronger than the coupling $\varepsilon_m^{\mathrm{Te}}$ between mobile Te which do not form a dimer. Te dimers tend to arrange in rows, leading to a (2×1) symmetry: thus $\varepsilon_x^{\mathrm{Td}}$ is necessarily negative. From simulations of planar lattice gas models [11, 61] $|\varepsilon_d^{\mathrm{Cd}}|$ has been estimated to be approximately 0.1 eV. Additionally, it has been argued [11] that the activation energy for the desorption of a single atom—which is $\approx 2|\varepsilon_c|$—should be on the same order as the macroscopic activation energy for sublimation. For the latter, experimentally determined values range from 0.96 eV to 1.95 eV depending on the particle species and sublimation mode [51, 57, 72]. A value of $\varepsilon_c = -6.5|\varepsilon_d^{\mathrm{Cd}}|$ corresponding to a desorption energy of ≈ 1.3 eV should thus be a reasonable starting point. The binding energy ε^* in the reservoir must not be too small such that Te* are not desorbed too fast and incorporation of Te atoms on $c(2 \times 2)$ reconstructed surfaces via the reservoir becomes possible. At low temperatures, a reservoir occupation of $\theta^* \approx 1/2$ should be stabilized. Thus, a negative value of ε_b^* is required. We choose $\varepsilon_b^* = -8|\varepsilon_d^{\mathrm{Cd}}|$ such that for a fully occupied reservoir ($\theta^* = 1/2$) the mean field interaction $\varepsilon_b^* \theta^*$ between Te* atoms is on the same order as the intra-layer interaction of mobile Cd atoms in a perfect $c(2 \times 2)$ or (2×1) reconstruction with $\theta^{\mathrm{Cd}} = 1/2$.

The barrier for diffusion of a Te atom on the SOS surface should be smaller than the barrier for the transition into a Te* state. This implies $B_o < |2\varepsilon_c - \varepsilon^*|$. On the other hand, the barrier for the transition of a Te* atom to a regular SOS site should be smaller than the one for desorption of Te* which yields $B^* < |\varepsilon^*|$.

For the attempt frequencies in the Arrhenius rates [Eq. (2.2)] we choose $\nu_o = 10^{12}\,\mathrm{s}^{-1}$ for the diffusion of mobile atoms at the surface, following earlier investigations [10, 11, 72]. The transition of Te* atoms to regular Te states and the evaporation of mobile Te* is modeled using $\nu^* = 10^8\,\mathrm{s}^{-1}$, similar to the value used in [71] for the diffusion of weakly bound arsenic.

By setting the value of the interaction between lateral diagonal Cd neighbors to $\varepsilon_d^{\mathrm{Cd}} = -1$ we fix the energy scale in our simulations. In addition we set $k_B = \left|\varepsilon_d^{\mathrm{Cd}}\right| = 1$ formally and, hence, measure the temperature T on the same scale. In the next chapter we will comment on a potential quantitative comparison with experimental data.

2.4 Summary

We have presented and discussed in detail a solid-on-solid lattice gas model for the simulation of epitaxial growth on II–VI(001) semiconductor surfaces. In our discussion we have focused on the description of CdTe surfaces though many aspects would carry over to other material systems such as, e.g. ZnSe or ZnTe. The model accounts for the zincblende lattice structure of CdTe as well as the relevant surface reconstructions of both Cd and Te terminated surfaces. Two different particle species, Cd and Te, are considered in our model. The particles interact via effective short-range pair-interactions, the strength of which is partially based on the results of DFT total energy calculations and available experimental data. For example, the interactions between lateral nearest and diagonal neighbors of mobile Cd atoms reflect the fact that there is a very small difference in the surface energies of the $c(2 \times 2)$ and (2×1) vacancy structures for a Cd terminated surface at maximum coverage and zero temperature.

In addition to Cd and Te atoms which reside at SOS surface sites, we allow for the storage of additional Te in a weakly bound Te* state. This is motivated by experimental studies where surface coverages $\theta^{\mathrm{Te}} > 1$ have been observed at low temperatures and high Te fluxes. Though the presence of excess Te at the surface is rather obvious, the true nature of the binding state has not been resolved yet. In our model, we incorporate the weakly bound Te* in terms of a mean field ansatz by introducing a reservoir with limited Te* occupation. The reservoir is also essential to facilitate growth in the model as Te* atoms may be localized on top of Cd atoms and thus neutralize the infinite repulsion between lateral nearest neighbors of mobile Cd in the y-direction. Since the experimental data and results from first principle calculations are not sufficient for a systematic fit of the model parameters, in its present state the model is not intended to give a full quantitative matching with experiments. In simpler versions of the model [11, 70] a semi-quantitative matching of macroscopic activation energies for step-flow and layer-by-layer sublimation with experimental results has been achieved. In comparative studies with the present extension of the model we obtain activation energies which are of equal quality. This confirms that the used parameters (Sec. 2.3.7), although partially based on estimates, correspond to a physically reasonable region of the parameter space.

Chapter 3

Growth Rates in Atomic Layer Epitaxy

In standard molecular beam epitaxy (MBE) of binary II–VI semiconductors (e.g. CdTe, ZnSe, ZnTe), where the constituent elements are brought to the surface simultaneously, the reduced surface mobility of the incoming species may result in rough growth fronts and thus makes it difficult to grow perfectly flat layers. An alternative technique, developed by Suntola and Antson in the mid 1970s, is the so-called atomic layer epitaxy (ALE) [2,73]. Here, cations and anions are sent sequentially onto the substrate in pulses with flux F and duration t_p, leaving dead times t_d in-between. The whole sequence comprising a pulse of each element and the intermediate dead times is called ALE or reaction cycle, see Fig. 3.1 for an illustration.

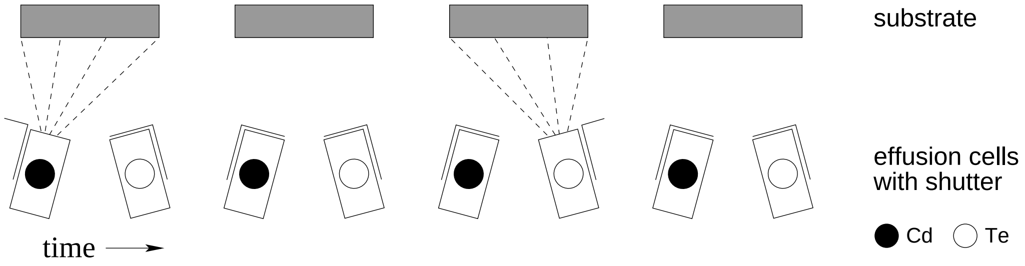

Figure 3.1: Schematic illustration of one reaction cycle in ALE growth of CdTe. The constituent elements are sent sequentially in pulses onto the substrate. The pulses are separated by dead times during which the effusion cells are closed.

ALE makes use of the fact that for II–VI materials like CdTe the bond strengths of the compound to be grown are usually much larger than those of the pure constituent elements (Cd or Te). Thus, throughout a, say, Te pulse the incoming Te is bound to the surface by strong Cd–Te bonds until saturation with Te is reached. The surplus Te will then be bound to the surface only very weakly and quickly evaporates during the subsequent dead time, provided the substrate temperature is sufficiently high. The same happens to Cd during the following Cd pulse. Consequently, growth proceeds in a surface-controlled mode instead of a source-controlled mode as is the case for conventional thin film techniques like MBE. In principle, a self-regulated growth rate of one complete monolayer (ML) of the compound per ALE cycle is obtained, and the cycle may be repeated indefinitely until the desired film thickness is reached.

However, in the case of II–VI semiconductors surface reconstructions may lead to deviations from the ideal growth rate of 1 ML per ALE cycle. For instance, the vacancy structures of cation terminated (001) surfaces (cf. Fig. 2.2) allow for coverages of at most 1/2 during the cation pulse. For CdTe(001) [66, 67], ZnSe(001) [74] and ZnTe(001) [52, 75], growth rates of only 1/2 ML per ALE cycle are reported experimentally for a wide range of temperatures, directly related to the submonolayer coverage of the reconstructed surfaces.

At sufficiently low temperatures, though, an increase of the growth rate from 1/2 ML to approximately 1 ML per ALE cycle is observed for, e.g., CdTe despite the limited coverage of the cation terminated surface [66, 67]. As a possible explanation for this increase the presence of additional Te at the end of the Te pulses has been discussed [57, 58], cf. Sec. 2.2. This should allow for the incorporation of more than 1/2 ML of Cd during the subsequent Cd pulse. Although the precise nature of the binding of this excess Te to the surface is yet unknown it is clear that the binding state must be relatively weak because for higher temperatures the ALE growth rate decreases to 1/2 ML per cycle.

In this chapter we will show by means of KMC simulations of ALE growth, that within the framework of the lattice gas model from Chap. 2 we are able to explain the experimentally observed temperature dependence of the ALE growth rate of CdTe(001). We argue that the presence of weakly bound excess Te at low temperatures is indeed crucial for the transition between the different growth rate regimes. In our model this weakly bound excess Te is realized by the reservoir of Te* introduced in Sec. 2.3.3. Before presenting results of the ALE simulations we will therefore discuss the properties of the Te* reservoir in greater detail.

3.1 Analysis of the Te* Reservoir Dynamics

In the model presented in Chap. 2, the occupation θ^* of the Te* reservoir results from the complex interplay of deposition, evaporation and transitions between Te* and Te states. However, the basic temperature dependence of θ^* can be understood from considering a flat surface in the presence of a steady flux of Te atoms.

After the Te coverage has reached the value $\theta^{\mathrm{Te}} = 1$, only deposition directly into the reservoir is possible. If we neglect the desorption of regular Te from the surface and transitions of the type Te → Te*, the temporal evolution of θ^* is governed by the balance of direct deposition and evaporation of Te*. The rate of the latter is a function of θ^* itself and one obtains the following simplifying ordinary differential equation:

$$\frac{d\theta^*}{dt} \approx F^{\mathrm{Te}}\,\Theta(1/2-\theta^*) - \theta^*\,\nu^*\,\exp\left[-\frac{1}{T}\left(|\varepsilon^*| + \theta^*\,|\varepsilon_b^*|\right)\right]. \tag{3.1}$$

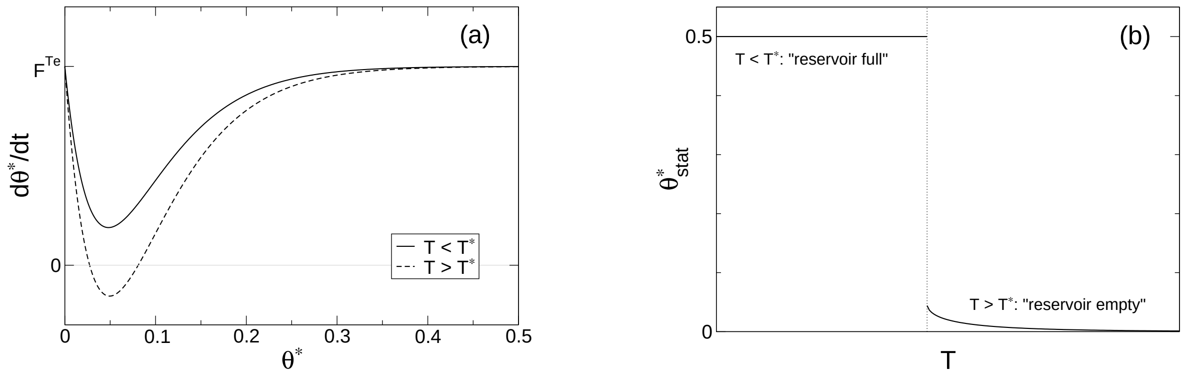

Figure 3.2: (a) Schematic representation of the r.h.s. of Eq. (3.1) for temperatures below and above the characteristic temperature T^* as described in the text. (b) Stationary reservoir occupation (solid line) versus temperature as derived from Eq. (3.1). The dotted line marks $T = T^*$.

Whereas the Te flux F^{Te} increases θ^*, desorption of Te* occurs with a frequency proportional to θ^* multiplied with the Arrhenius rate for single particle evaporation from the reservoir. Clearly, the filling of the reservoir must saturate at $\theta^* \approx 1/2$. However, the precise nature of the saturation process is not essential for the following considerations and we choose a simple cut-off represented by the Heaviside function: $\Theta(x) = 1$ for $x > 0$ and 0 otherwise.

Given ε^*, ε_b^*, ν^* and F^{Te}, the right-hand side in Eq. (3.1) is positive for all $\theta^* \in [0, 1/2]$ if the temperature T is low enough, see Fig. 3.2(a). Hence, the occupation θ^* reaches a stationary value $\theta^*_{stat} = 1/2$, that is the reservoir will be filled in this case. Above a characteristic temperature T^* the r.h.s. displays two zeros at fairly small values of θ^*, see Fig. 3.2(a). As a consequence, the differential equation has an attractive fixed point with a stationary value $\theta^*_{stat} \approx 0$ for $T > T^*$. In Fig. 3.2(b) the temperature dependence of the stationary reservoir occupation θ^*_{stat} is plotted schematically. Note that θ^*_{stat} jumps discontinuously at $T = T^*$.

Figure 3.3(a) shows T^* as function of F^{Te} for the choice of parameters $\varepsilon^* = -5$, $\varepsilon_b^* = -8$ and $\nu^* = 10^8\,\mathrm{s}^{-1}$. There is a rapid increase of T^* for very low values of F^{Te} which becomes weaker and weaker for higher fluxes. For $F^{\mathrm{Te}} = 5\,\mathrm{ML\,s}^{-1}$ we obtain $T^* \approx 0.39$, as an example, and at $T = 0.40$ the stationary occupation is already as low as $\theta^*_{stat} \approx 0.02$ in this case. Hence, starting from $\theta^* = 0$, the reservoir cannot be filled significantly for $T > T^*$. The behavior predicted from Eq. (3.1) is in excellent agreement with simulations of the situation in the full model. Note that in [66] a simple evaporation model of ALE growth was proposed which produces a flux-dependence of the characteristic temperature which is similar to the one in Fig. 3.3(a).

The simplified Eq. (3.1) is also useful in investigating the initial sublimation of Te* from a surface with maximum Te coverage 3/2, i.e. $\theta^{\mathrm{Te}} = 1$ and $\theta^* = 1/2$. Figure 3.3(b) displays the evolution of θ^* for $\varepsilon^* = -5$, $\varepsilon_b^* = -8$, $\nu^* = 10^8\,\mathrm{s}^{-1}$ and three different temperatures as obtained from the numerical integration of Eq. (3.1) with

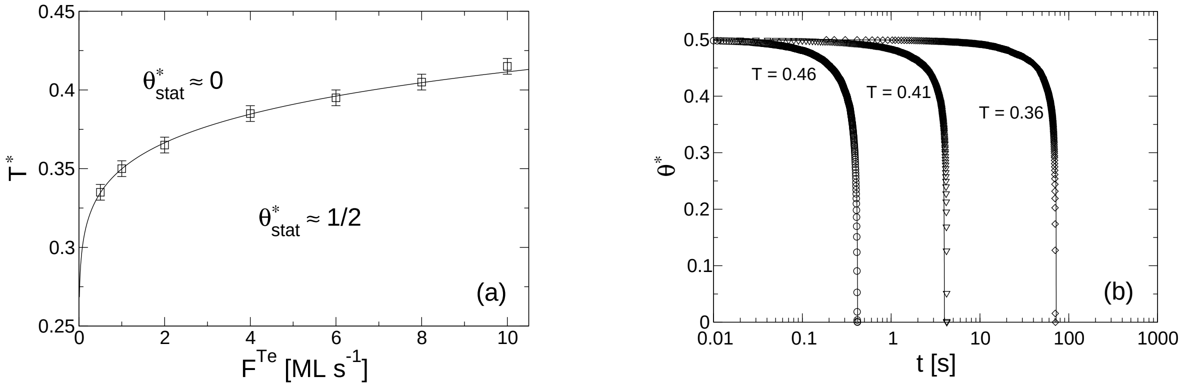

Figure 3.3: Analysis of the reservoir dynamics for $\varepsilon^* = -5$, $\varepsilon^*_b = -8$, $\nu^* = 10^8\,\mathrm{s}^{-1}$. (a) The temperature T^* above which an initially empty reservoir of Te* cannot be filled. The curve shows the result as obtained from Eq. (3.1). Additionally, symbols indicate the temperature where the growth rate drops from $\approx 1\,$ML to $\approx 0.5\,$ML CdTe per ALE cycle in the KMC simulations (cf. Sec. 3.2).
(b) Sublimation of Te* from an initially filled reservoir for three different temperatures. Solid lines represent the numerical integration of Eq. (3.1) with $F^{\mathrm{Te}} = 0$, symbols correspond to simulations of the situation in the full model.

$F^{\mathrm{Te}} = 0$. The results from simulations of the corresponding situation in the full kinetic model are again in excellent agreement with the simplified description, which neglects evaporation of regular Te and other processes.

We obtain a well-defined characteristic time τ^* for the decrease of θ^* from 1/2 to, say, $\theta^*_\tau = 0.05$. The precise value of θ^*_τ is of little relevance as $\theta^*(t)$ decreases to zero very rapidly, cf. Fig. 3.3(b). The temperature dependence of τ^* is very well described

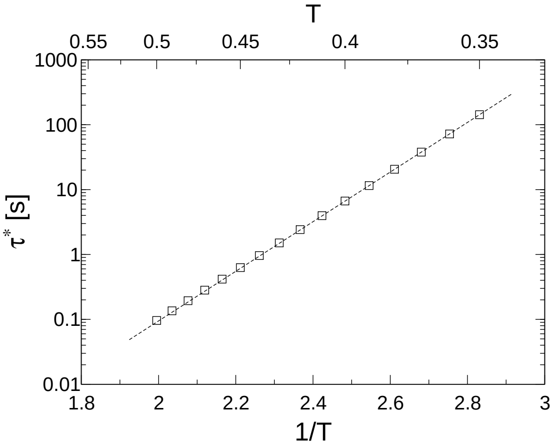

Figure 3.4: Temperature dependence of the characteristic time τ^* for Te* sublimation. The dashed line shows a fit to the data with an Arrhenius law as described in the text.

by an Arrhenius law $\tau^* = \tau_o \exp(E_a/T)$ with macroscopic activation energy $E_a \approx 8.5$ and prefactor $\tau_o \approx 3.8 \times 10^{-9}\,$s, see Fig. 3.4. In Refs. [51, 57] experimental data is discussed for the initial sublimation of Te starting from a Te-terminated surface with coverage 3/2. There, the macroscopic activation energy is reported to be $E_a \approx 0.96\,\mathrm{eV}$, providing a potential reference point for attempting a quantitative fit of our model.

Note that the prefactor $\tau_o \sim 10^{-9}\,\mathrm{s}$ obtained from Fig. 3.4 is not too different from the time constant $1/\nu^* = 10^{-8}\,\mathrm{s}$ assumed for Te* desorption. This should be expected, as the latter is the limiting microscopic process of the scenario. In an attempt to extract the prefactor from an analogous Arrhenius plot of experimental data [51] we obtain a value of about the same order, i.e. $\tau_o \sim 10^{-9}\,\mathrm{s}$. On the contrary, the value from data for Cd desorption [51] corresponds to frequencies which are larger by orders of magnitude. The determination of prefactors from experimental data for relatively small temperature ranges will most likely be flawed to some extent. Nevertheless the rough comparison may serve as additional qualitative justification for choosing ν^* much smaller than other frequencies in our model.

3.2 Simulation of ALE Growth

In order to gain a qualitative understanding of the ALE growth scenario we perform KMC simulations according to the standard scheme described in Sec. 1.5.2. All simulation results presented in the following are obtained with the parameter set specified in Sec. 2.3.7 and system sizes $N_x = N_y = 64$, averaging over five independent simulation runs. We model a situation in which Cd and Te are deposited in alternate pulses of length $t_p = 0.9\,\mathrm{s}$, each with a constant flux $F^{\mathrm{Cd}} = F^{\mathrm{Te}} = 5\,\mathrm{ML\,s^{-1}}$. The pulses are separated by a dead time $t_d = 0.1\,\mathrm{s}$, hence, the duration of one complete ALE cycle is $2(t_p + t_d) = 2\,\mathrm{s}$ in total. Note that the characteristic time τ^* for reservoir sublimation is large compared with the dead time interval for all relevant temperatures, cf. Fig. 3.4. For the following simulations the initial surface is perfectly flat and Te-terminated with coverage $\theta^{\mathrm{Te}} = 1$ and $\theta^* = 0$. Deposition always starts with a Cd pulse.

Illustrating surface snapshots of growing surfaces at $T = 0.44$ and $T = 0.36$ are shown in Figs. 3.5 and 3.7, corresponding to the two different growth regimes discussed in the following.

3.2.1 High Temperature Regime

At fairly high temperatures, growth proceeds according to the following scenario in our simulations:

I) The first Cd pulse adds half a layer of Cd to the system. The infinite repulsion of lateral NN in y-direction prevents coverages $\theta^{\mathrm{Cd}} > 1/2$. Except for a very short period at the beginning of the Cd pulse the predominant arrangement of Cd atoms is in a local $c(2 \times 2)$ ordering, i.e. a checkerboard pattern which is reflected in the magnitude of the Cd correlations K_x^{Cd} and K_d^{Cd}, see Fig. 3.6(a). The contribution of the (2×1) row structure as a thermal excitation increases with higher T.

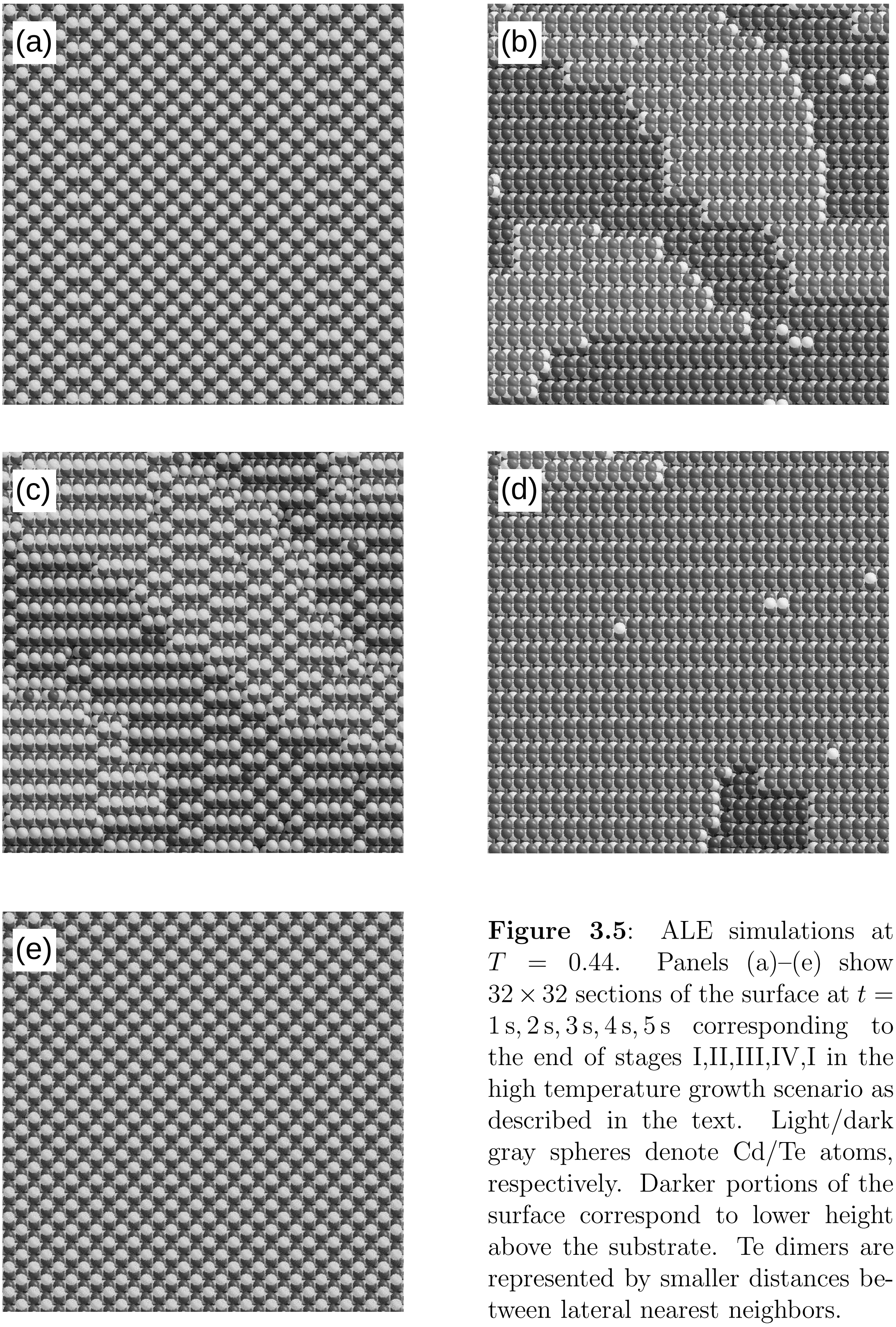

Figure 3.5: ALE simulations at $T = 0.44$. Panels (a)–(e) show 32×32 sections of the surface at $t = 1\,\mathrm{s}, 2\,\mathrm{s}, 3\,\mathrm{s}, 4\,\mathrm{s}, 5\,\mathrm{s}$ corresponding to the end of stages I,II,III,IV,I in the high temperature growth scenario as described in the text. Light/dark gray spheres denote Cd/Te atoms, respectively. Darker portions of the surface correspond to lower height above the substrate. Te dimers are represented by smaller distances between lateral nearest neighbors.

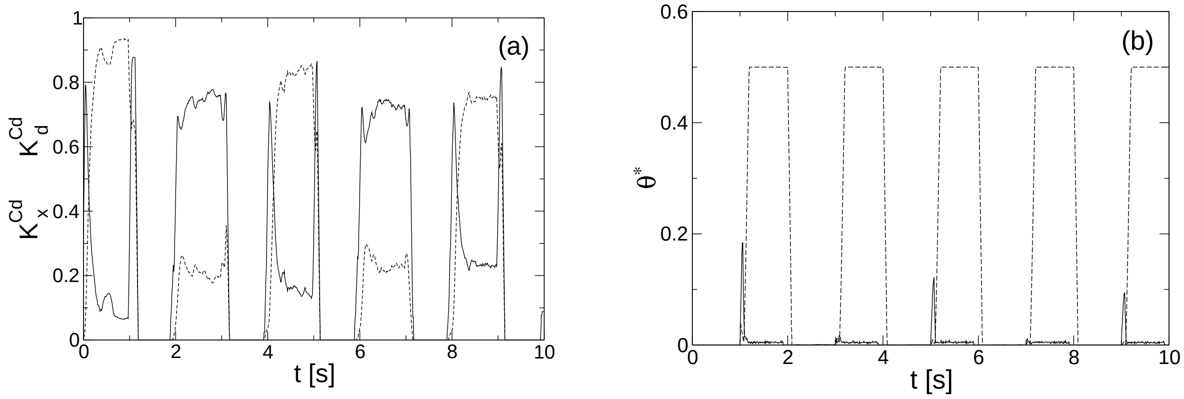

Figure 3.6: (a) Time dependence of the Cd correlations K_x^{Cd} (solid line) and K_d^{Cd} (dashed line) for the simulation run with $T = 0.44$ shown in Fig. 3.5. For clarity of plotting, the curves have been smoothed by averaging over an time interval $\Delta t = 0.06\,\mathrm{s}$ around each data point. (b) Time dependence of the reservoir occupation for the simulation runs with $T = 0.44$ (solid line) and $T = 0.36$ (dashed line) shown in Figs. 3.5 and 3.7.

II) After the first Te pulse and the dead time, half a layer of Te has been incorporated. Diffusion of particles leads to the formation of islands upon the Te-terminated surface. Note that the existence of the Te*-reservoir state is crucial for this process, as discussed in Sec. 2.3.5. Surface Te atoms form dimers, preferentially, and these arrange in rows along the x-direction, yielding a predominant (2×1) symmetry of the surface. Although incorporation of Te occurs to a considerable degree through the reservoir state Te*, at the end of the dead time one finds $\theta^* \approx 0$, as discussed above. This is confirmed by Fig. 3.6(b) which shows the time evolution of the reservoir occupation (solid line): θ^* remains close to zero except for a very short period at the beginning of the Te pulse when the Te terminated islands begin to form.

III) The second Cd pulse places mobile atoms on top of existing islands and in between. The pre-dominant local ordering is the (2×1) pattern, i.e. rows of Cd alternating with empty rows, again signaled by the Cd correlations in Fig. 3.6(a). This is due to the influence of the island edges on the reconstruction, an analogous effect occurs in layer by layer sublimation [11, 70, 76]. At the end of the dead time, the islands from stage II are still present but now they are Cd-terminated.

IV) During the second Te pulse, atoms are deposited onto the Cd-terminated islands and in between. The particles rearrange by means of diffusion, leveling off the islands and forming a flat Te-terminated surface. At the end of the dead time, the initial state of the system is restored with one complete layer of CdTe added to the system. In the simulations the filling of gaps is incomplete to a degree which depends on the temperature and the length of the dead time interval.

Hence, at temperatures $T > T^*$, our model reproduces ALE growth in the same double cycle sequence which was hypothesized and discussed for CdTe and ZnTe in the literature [57, 58]. Figure 3.8 shows the evolution of the film height with time in the ALE process at $T = 0.44$, which is well above the characteristic $T^* \approx 0.39$ obtained for $F^{\mathrm{Te}} = 5\,\mathrm{ML\,s^{-1}}$.

3.2.2 Low Temperature Regime

The picture changes qualitatively for temperatures $T < T^*$. We again prepare a flat Te-terminated surface with coverage $\theta^{\mathrm{Te}} = 1$, $\theta^* = 0$, and deposition starts with a Cd pulse. The surface structures obtained after the first Cd and Te pulse are very much alike the ones of stages I and II of the high temperature scenario, since initially the Te* reservoir is empty. Note however, that due to a decreased mobility of the atoms the islands on the Te terminated surface are less compact. Since $T < T^*$, at the end of the Te pulse the surface is not only Te terminated but also the Te* reservoir is filled, i.e. $\theta^* \approx 1/2$, as can be seen in Fig. 3.6(b). Thus, from this point on the ALE growth scenario proceeds along the following lines in our model:

A) The Cd pulse places atoms onto the islands and in between which is analogous to stage III of the high temperature scenario. But now Cd particles at the surface can coalesce, because Te* from the reservoir are available to neutralize the NN repulsion of mobile Cd in y-direction. Therefore the gaps between the islands are leveled out by half a monolayer of Cd atoms and the reservoir which provides also approx. 1/2 monolayer of Te. The surface is then covered by another half layer of Cd atoms arranging in a mixed $c(2 \times 2)$-(2×1) vacancy structure. Thus, the adsorption of one complete monolayer of Cd and a half monolayer of Te which came from the reservoir leads to an increase of the surface height by 3/4 of a complete CdTe layer. At the end of step A) the reservoir is empty, see Fig. 3.6(b).

B) The following Te pulse leads to a Te terminated surface with islands, which is identical to the one described above. Again, due to low temperature and short dead time, also the Te* reservoir is filled. Hence, another half monolayer of Te is adsorbed and in total one complete layer of CdTe added in only one ALE cycle. At the end of step B) the reservoir has reached its maximum occupation, see Fig. 3.6(b).

Figure 3.8 shows the evolution of the mean surface height $\langle h \rangle$ with time at $T = 0.36$, i.e. below T^* for $F^{\mathrm{Te}} = 5\,\mathrm{ML\,s^{-1}}$. Note that for the first Cd and Te pulse ($t \leq 2s$), the curve is essentially identical with that of the high T regime, because in both simulations the reservoir is empty, initially. Hence the upper curve of Fig. 3.8 corresponds to the sequence of stages A/B only for times $t > 2\,\mathrm{s}$. The mean height as displayed in Fig. 3.8 increases by 3/4 of a complete CdTe layer during the Cd pulse A) because $\langle h \rangle$ takes into account only particles at SOS lattice sites, disregarding the Te* reservoir.

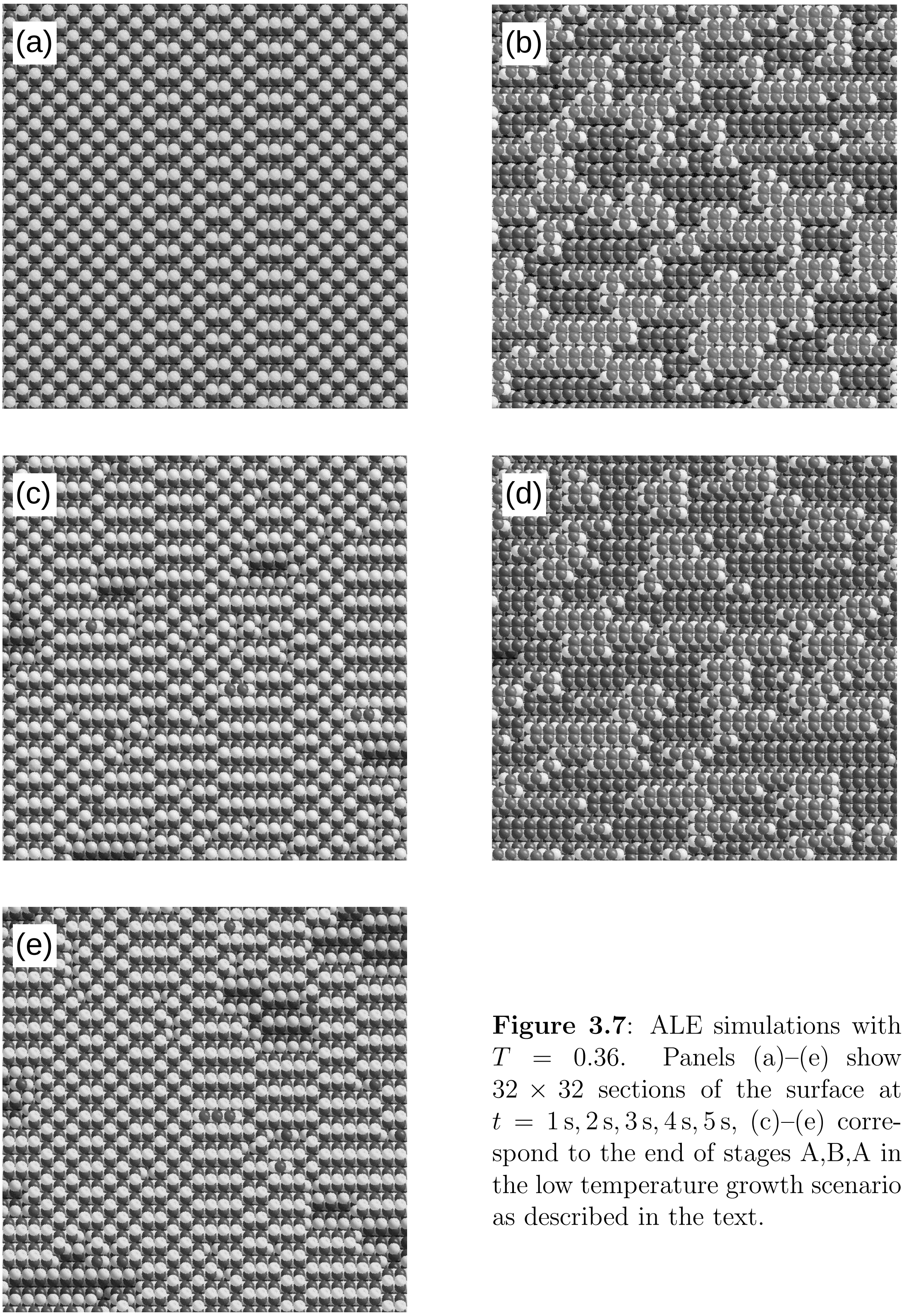

Figure 3.7: ALE simulations with $T = 0.36$. Panels (a)–(e) show 32×32 sections of the surface at $t = 1\,\mathrm{s}, 2\,\mathrm{s}, 3\,\mathrm{s}, 4\,\mathrm{s}, 5\,\mathrm{s}$, (c)–(e) correspond to the end of stages A,B,A in the low temperature growth scenario as described in the text.

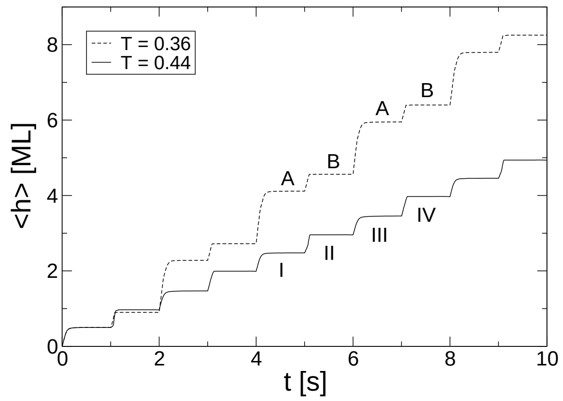

Figure 3.8: Mean height of the film vs time for ALE simulations with $T = 0.44$ and $T = 0.36$. $\langle h \rangle$ takes into account only particles at regular lattice sites, excluding the reservoir of Te*. Numbers I-IV and letters A,B mark the stages of the two different growth scenarios as described in the text.

From simulations for various temperatures we have obtained the average growth rate per ALE cycle. Figure 3.9(b) shows that, with increasing T, the growth rate drops very rapidly in the vicinity of the characteristic T^* as obtained from the considerations of Sec. 3.1. The comparison with Fig. 3.9(a) shows qualitative agreement with experimental results for an analogous growth scenario studied by Faschinger and Sitter [66]. Very similar data has been published by Hartmann *et al.* [67] and is also discussed in Ref. [57]. Note that in both experiments growth rates above 1 layer of CdTe per ALE cycle were observed at very low temperatures. This is presumably due to the formation of Cd crystallites at the surface and cannot be reproduced in our model [58].

The temperature driven break-down of the growth rate is due to the fact that the reservoir cannot be filled significantly for $T > T^*$. Simulation results for various values of the flux strongly support this assumption as can be seen from Fig. 3.3(a): the symbols which indicate the temperature where the growth rate drops in the simulations lie almost exactly on the curve that marks T^*.

In principle, the re-evaporation of Te* during the dead time interval could be an alternative cause for the reduced growth rate. Note, however, that even for a flux as high as $F^{\mathrm{Te}} = 10\,\mathrm{ML\,s^{-1}}$ with $T^* \approx 0.41$, one finds that the characteristic time for reservoir sublimation is $\tau^* \approx 4\,\mathrm{s}$, cf. Fig. 3.3(b). Hence, it appears safe to say that during dead time intervals shorter than, say, 1 s, θ^* will remain close to the maximum value 1/2, provided all other conditions allow for the filling of the reservoir during a Te pulse. As a consequence, we expect that the characteristic value of T which marks the drop of the growth rate in Fig. 3.9 should be essentially independent of the pulse duration or dead time interval within a wide range of reasonable values.

Comparing the experimental results by Hartmann *et al.* [67] and Faschinger and Sitter [66] for the ALE growth rate one finds that the temperature where the growth rate drops to approximately 1/2 layers of CdTe per cycle is different in the two studies: a temperature of ≈ 250°C is reported in [67], whereas in [66] the drop of the growth rate has been observed at a higher temperature of ≈ 290°C. Within the framework of our model the temperature difference can be explained if one takes into account the respective experimental conditions. Whereas Hartmann *et al.* combined particle fluxes of about $0.5\,\mathrm{ML\,s^{-1}}$ with 8 s pulse time and 1 s dead times, the flux used by

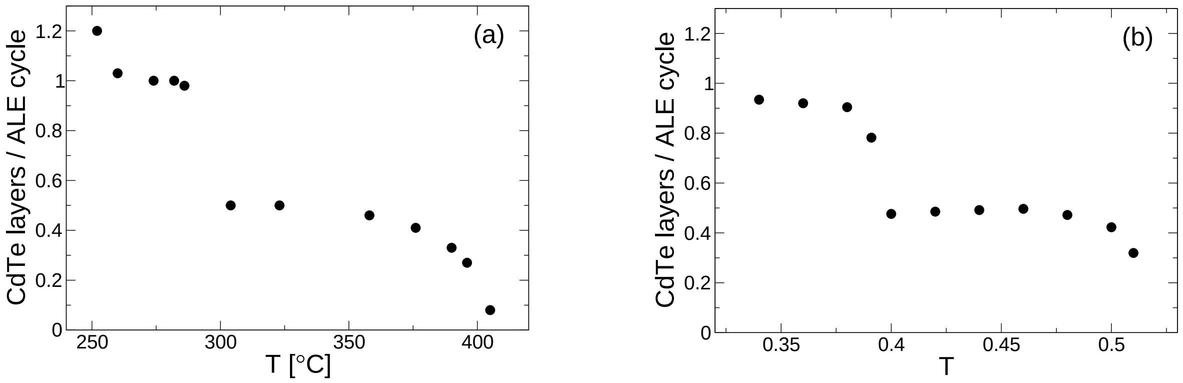

Figure 3.9: Growth rates in layers of CdTe per ALE cycle vs temperature T.
(a) Experimentally observed growth rates of CdTe(001) as published by Faschinger and Sitter (plot generated after Fig. 3 in Ref. [66]). The pulse duration was 0.8 s with a total deposition of 1.5 layers of each element, followed by dead time intervals of length 0.2 s. The most prominent feature is the sudden decrease of the growth rate at $T \approx 290°\mathrm{C}$. One additional data point has been omitted (growth rate 1.4 layers per cycle at 230°C).
(b) Average growth rates in the ALE simulations with parameters as described in Sec. 3.2. The temperature is measured in dimensionless units of $\left|\varepsilon_d^{\mathrm{Cd}}\right| = 1$. The growth rate drops at $T \approx T^* \approx 0.39$ for $F^{\mathrm{Te}} = 5\,\mathrm{ML\,s^{-1}}$.

Faschinger and Sitter was about $2\,\mathrm{ML\,s^{-1}}$ with a pulse duration of 0.8 s and a dead time of 0.2 s. As discussed above, the difference of the dead times can be neglected, but for the given fluxes one reads from Fig. 3.3(a) a significant increase of T^* by about 9%. As demonstrated, T^* practically coincides with the temperature where the growth rate drops which consequently is expected to increase by the same amount. The difference of the absolute temperatures observed in Refs. [67] and [66] is about 8% (of the lower one) which is indeed comparable with our results.

For very high T, sublimation of the crystal dominates over the incoming flux and growth becomes impossible. The ALE growth rate vanishes at a temperature which is essentially independent of the properties of Te* atoms.

3.2.3 Growth on a Vicinal Surface

For completeness, we have also performed ALE simulations on a stepped surface. The steps are parallel to the [100] direction and the terraces have a width of 16 lattice constants. All other parameters are the same as in the preceding simulations. Starting with a Te terminated surface and $\theta^* = 0$ we find that for low temperatures growth proceeds along the same sequence as described in Sec. 3.2.2. Again, we obtain a growth rate of about 1 ML of CdTe per ALE cycle. At $T \approx T^*$ the growth rate drops to $\approx$ 0.5 ML CdTe per ALE cycle and for both high and low temperatures the time evolution of the mean surface height looks similar to the one shown in Fig. 3.8.

In the high temperature regime, though, we do not observe the double cycle sequence

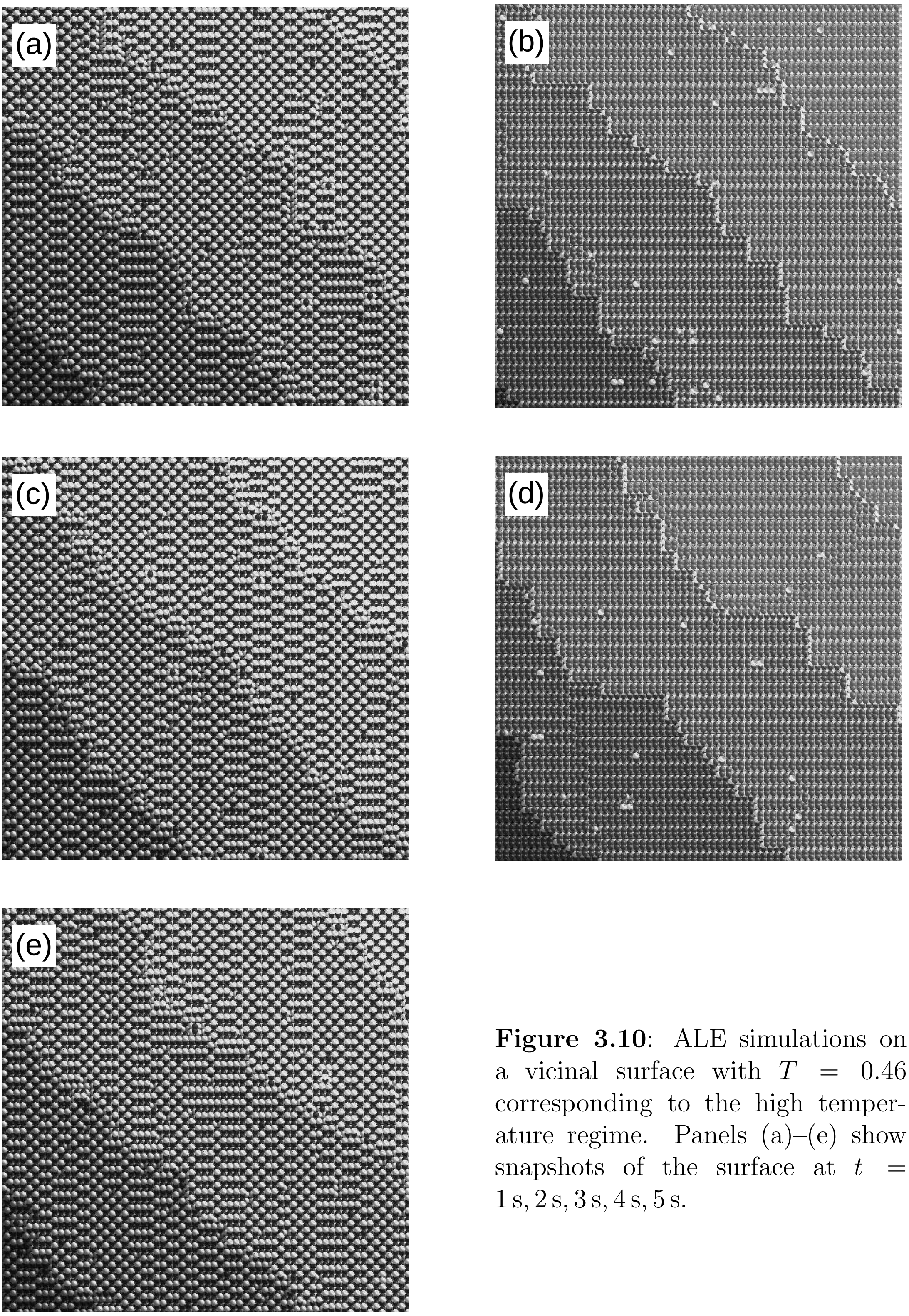

Figure 3.10: ALE simulations on a vicinal surface with $T = 0.46$ corresponding to the high temperature regime. Panels (a)–(e) show snapshots of the surface at $t = 1\,\mathrm{s}, 2\,\mathrm{s}, 3\,\mathrm{s}, 4\,\mathrm{s}, 5\,\mathrm{s}$.

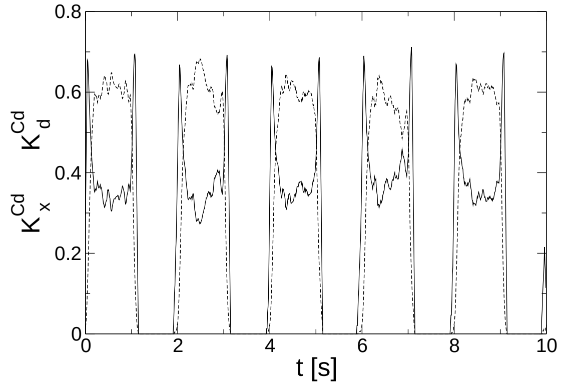

Figure 3.11: Time evolution of the Cd correlations K_x^{Cd} (solid line) and K_d^{Cd} (dashed line) for the ALE simulation run shown in Fig. 3.10. For clarity of plotting, the curves have been smoothed by averaging over an time interval $\Delta t = 0.06\,\mathrm{s}$ around each data point.

as described in Sec. 3.2.1, that is, there is no alternation between a rough surface with islands and a flat surface in subsequent ALE cycles. Instead, all deposited particles are captured by the step edges and growth proceeds in a step flow mode as can be seen from Fig. 3.10 which shows surface snapshots for a simulation run at $T = 0.46$.

Due to the absence of island formation the $c(2\times2)$ reconstruction dominates during each Cd pulse which is reflected in the Cd correlations, see Fig. 3.11. Note that at the beginning of each Cd or Te pulse K_x^{Cd} is peaked because for low Cd coverages it is locally favorable for Cd atoms to align along the x-direction, contributing thus to the (2×1) arrangement. The same effect has already been observed at the beginning of stages I and II in the high temperature regime for growth on a flat surface, cf. Fig. 3.6(a).

3.3 Summary and Outlook

In summary, we have shown by means of KMC simulations of the growth model from Chap. 2 that the reservoir of weakly bound Te* may explain the experimentally observed temperature dependence of ALE growth rates for, e.g., CdTe(001). Although the precise nature of such a weakly bound Te* state at the surface is unknown, its existence is clearly evident from various experimental observations [57, 58]. In our simulations, only below a characteristic temperature T^* a significant amount of Te* is present and facilitates growth rates of approximately 1 layer of CdTe per ALE cycle. As in the corresponding experiments, we observe a sudden transition from the self-limited growth rate of about 1/2 layer per ALE cycle at high T to the low temperature regime with a rate close to 1 complete layer per cycle.

Our analysis shows that the characteristic transition temperature should depend only weakly on the model (or experimental) parameters within a wide range of reasonable choices. The key dependence is on the particle flux during Cd and Te pulses, respectively, and our model reproduces its effect on the transition qualitatively correct.

As an attempt towards a more quantitative comparison with experiments, one might identify the temperature $T^* \approx 0.365$ for a flux of $2\,\mathrm{ML\,s^{-1}}$ in our model (cf. Fig 3.3) with the experimental value $T \approx 290^{\circ}\mathrm{C}$ by Faschinger *et al.* [66]. Thus, the energy scale $\varepsilon_d^{\mathrm{Cd}}$

of our model may be fixed, and we obtain $\varepsilon_d^{\mathrm{Cd}} = -0.133\,\mathrm{eV}$. This, in turn, yields a value of $E_a \approx 1.13\,\mathrm{eV}$ for the macroscopic activation energy for desorption of Te* atoms which roughly agrees with the experimentally determined $0.96\,\mathrm{eV}$ [51, 57]. Furthermore, the value of T^* for our simulations with $5\,\mathrm{ML\,s^{-1}}$ translates into $T^* \approx 329^{\circ}\mathrm{C}$ which agrees well with results of the simple evaporation model discussed in [66].

Thus, a quantitative match with experimental data seems feasible. In simpler versions of the model it was possible to reproduce the temperature dependence of the surface reconstruction as well as macroscopic sublimation rates on a semiquantitative level [70]. The larger number of parameters in the current extension, however, requires further input from experiment. In addition, reliable estimates of microscopic energy barriers from, e.g., first principle quantum chemical or density functional calculations as are available for III–VI semiconductors [26, 30, 77, 78] would be extremely useful. Such calculations should also shed light on the nature of the weakly bound Te* states on the surface.

Chapter 4

Nanostructure Formation in Surface-Confined Alloys

Heteroepitaxial growth of thin films has been a field of growing interest in recent years [1] as it displays a variety of highly non-trivial phenomena. Among these are, e.g., the self-organized formation of three-dimensional islands, so-called Quantum Dots [79], self-assembly of ordered nanoscale domain patterns [80] or lateral multilayers [81], or the emergence of misfit dislocations [82].

In this chapter we use (kinetic) Monte Carlo simulations of a model ternary system to determine the influence of kinetic and strain effects on the morphology of self-assembled nanostructures during submonolayer heteroepitaxy. Therefore we study the growth of two different types of adsorbate particles on a given substrate. Our investigations are mainly motivated by experimental studies on metal epitaxy where a variety of material systems have been found which, though immiscible in the bulk, form stable alloy layers if deposited as a thin film onto specific substrate materials. This form of surface-confined alloying is reported for, e.g., CoAg/Ru(0001) [82–85], CoAg/Mo(110) [81], FeAg/Mo(110) [81], CuAg/Ru(0001) [86], and PdAu/Ru(0001) [87]. All these material systems, as diverse as they may seem at first sight, have one thing in common: the lattice constant of the first adsorbate component is smaller with respect to the substrate (i.e. it has a negative misfit) whereas the lattice constant of the second component is larger (positive misfit). For such systems which are dominated by atomic size mismatch it has been shown theoretically [88] that surface alloying may serve as a possible strain relaxation mechanism. The condition is that the decrease of the strain energy caused by the intermixing outbalances the increase of the interface energy.

Besides the presence of both positive and negative misfit in the same heteroepitaxial system, differences in binding energies play a decisive role as they tend to separate the two adsorbate materials. From both theoretical models [89, 90] and experimental observations [83] it is known that the competition between chemical interactions, favoring phase separation, and elastic interactions, favoring alloying [88], may result in stripe-like structures. Furthermore the alloying can lead to a change in the morphology of the grown films. For example, in the case of CoAg/Ru(0001) both Co and Ag form islands

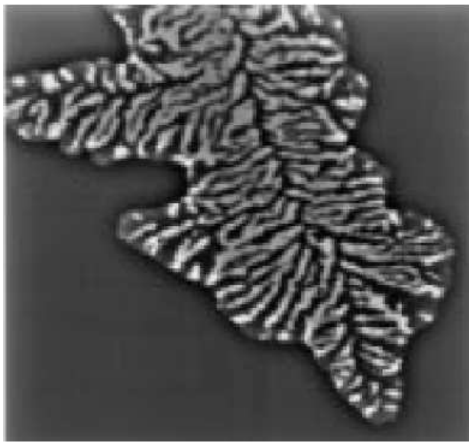

Figure 4.1: $50 \times 50\,\mathrm{nm}^2$ scanning tunneling microscopy image of a dendritic CoAg island on Ru(0001) (taken from Ref. [83]).

of compact shape if deposited alone onto the substrate. Their co-deposition however yields ramified islands [83] which consist of alternating veins of approximately constant width (see Fig. 4.1).

It has been conjectured in [83] that the difference in the chemical binding energies of the two adsorbate species results in an enhanced diffusion barrier for a particle trying to cross the interface at the edge of a vein structure. This again should cause atoms diffusing along step edges to become either reflected or desorbed at the interface and thus naturally lead to ramification. Following this hypothesis the island ramification observed for CoAg/Ru(0001) should be generic for multi-component growth where different chemical binding energies are inherently present. However, it is still an open question which are the real underlying microscopic mechanisms for the formation of the described multi-component structures and to what extent e.g. kinetic effects are involved.

4.1 Lattice Gas Description

In the following we will set up a lattice gas model to investigate the influence of kinetics on the film morphologies during multi-component growth. The implementation of different chemical binding energies between different particle species allows for a clarification of the hypothesis made in [83]. Additionally, we will gain knowledge about how features of nanostructures depend on control and material parameters which is essential for the preparation of such nanostructures. Since an explicit treatment of strain effects is inherently beyond the scope of a simple lattice-based simulation method, at a later point we will compare our results with those obtained by an off-lattice simulation method where both strain and binding energy effects are taken into account [17].

4.1.1 Simulation Model

We consider a solid-on-solid model with two adsorbate species, denoted A and B in the following, which grow on a different planar substrate S with simple cubic (sc) structure. The topmost layer of the substrate provides a square lattice with $N \times M$ adsorption sites (x, y) for the adsorbate particles. The sc symmetry is chosen for computational benefits: each lattice site has only four in-plane nearest neighbor (NN) sites compared to six in-plane NN in the case of a close-packed lattice [e.g., face-centered cubic (fcc) or hexagonal close-packed (hcp)]. This allows for a faster calculation of the activation energies E_a for diffusion events since we have to take only four NN into account in the bond-counting procedure, cf. Sec. 1.4.1. Another reason for choosing the sc structure is the possibility to compare our simulation results with those from the off-lattice model (Sec. 4.4) where also the sc symmetry is considered.

One important problem with this choice, though, is that the majority of the experimental results mentioned above are given for metals grown on substrates with fcc/hcp symmetry. However, it is reasonable to assume that the symmetry of the underlying substrate will primarily affect the geometry of the grown adsorbate islands. In the case of the experimental systems one finds triangular shaped islands whereas for the sc structure square shaped islands are expected, cf. Sec. 1.3.2.

In our model each lattice site (x, y) may be either empty or occupied by an A or B particle. Adsorbate particles interact with their lateral NN through attractive two-particle interactions with the energy parameters E^{AA}, E^{BB} and E^{AB}. Here, E^{AA} and E^{BB} denote the binding of two A-particles or two B-particles, respectively, whereas E^{AB} represents the inter-species binding between A- and B-particles. The total energy of the system can then be written as

$$H = -E^{\mathrm{AA}} n^{\mathrm{AA}} - E^{\mathrm{BB}} n^{\mathrm{BB}} - E^{\mathrm{AB}} n^{\mathrm{AB}} - \mu^{\mathrm{A}} n^{\mathrm{A}} - \mu^{\mathrm{B}} n^{\mathrm{B}}, \tag{4.1}$$

where $n^{\mathrm{A}}, n^{\mathrm{B}}$ denote the number of A and B particles, and $n^{\mathrm{AA}}, n^{\mathrm{BB}}, n^{\mathrm{AB}}$ count the number of A–A, B–B and A–B bonds, respectively. The binding of adsorbate particles to the substrate is represented by the effective chemical potentials μ^{A} and μ^{B}.

Two basic microscopic processes are taken into account: random deposition of adsorbate particles onto the substrate, and diffusion of adatoms on the substrate. Since here we are only interested in the submonolayer regime we disregard second layer nucleation, i.e. particles which are deposited onto other particles will be ignored. This would correspond to the presence of a very high Schwoebel barrier for diffusion across step edges, cf. Sec. 1.4.3. Note that for the same reason diffusion jumps of particles onto others are suppressed. For the temperature regime considered in the following, desorption of adsorbate particles is also negligible and therefore omitted from our simulations.

Diffusion of adatoms on the surface is described by thermally activated NN hopping processes with Arrhenius rates

$$R = \nu_o \exp(-\frac{E_a}{k_B T}) \tag{4.2}$$

where we choose $\nu_o = 10^{12}\,\mathrm{s}^{-1}$ as common attempt frequency for all diffusion processes.

For the activation energy E_a of a diffusion event which leads from the initial (i) to the final (f) configuration we use Kawasaki-type energy barriers (cf. Sec. 1.4.2)

$$E_a = \max\left\{B_i, B_f + \Delta H\right\}, \tag{4.3}$$

where ΔH denotes the total energy change caused by the diffusion event and is given by Eq. (4.1). The diffusion barriers B_i and B_f depend on the type of the diffusing particle as well as the local surrounding at its initial and final position (cf. Sec. 1.4.2). Note that a diffusion event does not change the number of A and B particles $(n^{\mathrm{A}}, n^{\mathrm{B}})$ in Eq. (4.1). Without loss of generality we may thus set $\mu^{\mathrm{A}} = \mu^{\mathrm{B}} = 0$ in the absence of desorption.

4.1.2 Symmetric Parameter Set

In order to obtain a general insight into the behavior of the model and at the same time keep the number of parameters low, in the basic variant of our model we assume a common value for all barriers B_i, B_f in Eq. (4.3), i.e.

$$B_i = B_f = B^0 \qquad \forall\, i, f \tag{4.4}$$

Also, the strength of A–A and B–B bonds shall be the same in this (simplifying) case:

$$E^{\mathrm{AA}} = E^{\mathrm{BB}} = E^0. \tag{4.5}$$

The model then is mainly governed by the interaction E^{AB} between A and B particles which is assumed to be weaker than between two particles of the same type,

$$E^{\mathrm{AB}} < E^0, \tag{4.6}$$

following the hypothesis in [83]. We will refer to this situation as the symmetric parameter set since A and B particles are treated identically apart from the weaker binding energy between them. Later, the comparison between lattice gas and off-lattice simulation results requires the use of an enhanced parameter set which is fitted to a set of off-lattice diffusion barriers corresponding to characteristic diffusion situations (see Sec. 4.5).

Figure 4.2(a) shows exemplary diffusion processes of a free B particle (light gray) on the substrate and B particles at the boundary of a small A–B cluster together with their corresponding activation energies [Eq. (4.3)] for the symmetric parameter set. For A particles the picture is essentially the same, except that the activation energies for crossing the A–B interface have to be exchanged, as well as those for detachment from A and B step edges. In Fig. 4.2(b) the activation energies E_a for a diffusion jump of a B particle parallel (in negative x-direction) and perpendicular to the step edge of a small A–B cluster are plotted versus the x-position of the B particle. As long as the particle is away from the step edge the activation energies for both diffusion directions

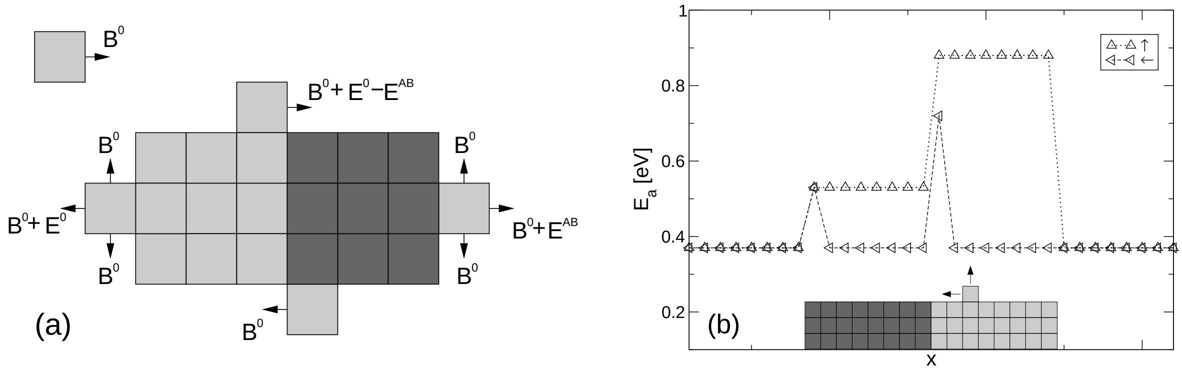

Figure 4.2: Diffusion processes and corresponding activation energies for the symmetric version of the lattice gas model. (a) Diffusion of a free B particle (light gray) and B particles at the step edge of a small A–B cluster. (b) Activation energies for diffusion of a B particle parallel (from right to left) and perpendicular to the step edge of a small A–B cluster. The values correspond to $B^0 = 0.37\,\text{eV}$, $E^0 = 0.51\,\text{eV}$, $E^{\text{AB}} = 0.16\,\text{eV}$.

are the same and equal to B^0. When the particle sits at the step edge the value of E_a for perpendicular diffusion, that is detachment from the step edge, is larger because the particle has to break the bond to the NN sitting in the step edge. The barrier for diffusion along the step edge remains B^0 as long as the particle is away from the A–B interface. Now the fact that $E^{\text{AB}} < E^0$ has two main implications. First, the B particle faces an enhanced diffusion barrier $B^0 + E^0 - E^{\text{AB}} > B^0$ when it attempts to cross the A–B interface coming from the B side. Note that for the reverse jump the barrier is B^0, cf. Fig. 4.2(a). The same happens to an A particle which tries to cross the interface coming from the A side. Thus, A and B particles diffusing along step edges are likely to be reflected at A–B interfaces. Second, the activation energy for detachment of a B particle from a step edge made up of A particles is lower than that for detachment from a B step edge and vice versa, cf. Fig. 4.2(b). This should lead to preferential sticking of particles to regions of the same type.

4.2 Simulations with Symmetric Parameter Set

In the following we will investigate the influence of the interaction E^{AB} between A and B adsorbate particles on the morphology of growing films. Therefore we perform KMC simulations using the symmetric parameter set [Eqs. (4.4)–(4.6)]. We fix $B^0 = 0.37\,\text{eV}$ and $E^0 = 0.51\,\text{eV}$, corresponding to typical values for metal self-diffusion and detachment barriers (see, e.g., [33, 44, 91]). On the other hand, E^{AB} is varied between $0.06\,\text{eV}$ and $0.51\,\text{eV}$, corresponding to $0.12 < \alpha \leq 1$ for the ratio $\alpha = E^{\text{AB}}/E^0$ of the binding energies. If not otherwise mentioned the temperature is set to $T = 500\,\text{K}$.

4.2.1 Island Geometry

At time $t = 0\,\mathrm{s}$ we prepare a flat square substrate with $N = M = 150$ and periodic boundary conditions in both lattice directions. The deposition rate for both A and B particles is set to $5 \times 10^{-3}\,\mathrm{ML\,s^{-1}}$ resulting in an overall deposition rate of $10^{-2}\,\mathrm{ML\,s^{-1}}$. When the total adsorbate coverage $\theta = (n^{\mathrm{A}} + n^{\mathrm{B}})/N^2$ has reached 0.5 the particle fluxes are switched off and the simulation is halted. The realization of the simulation algorithm follows the outline given in Sec. 1.5.2.

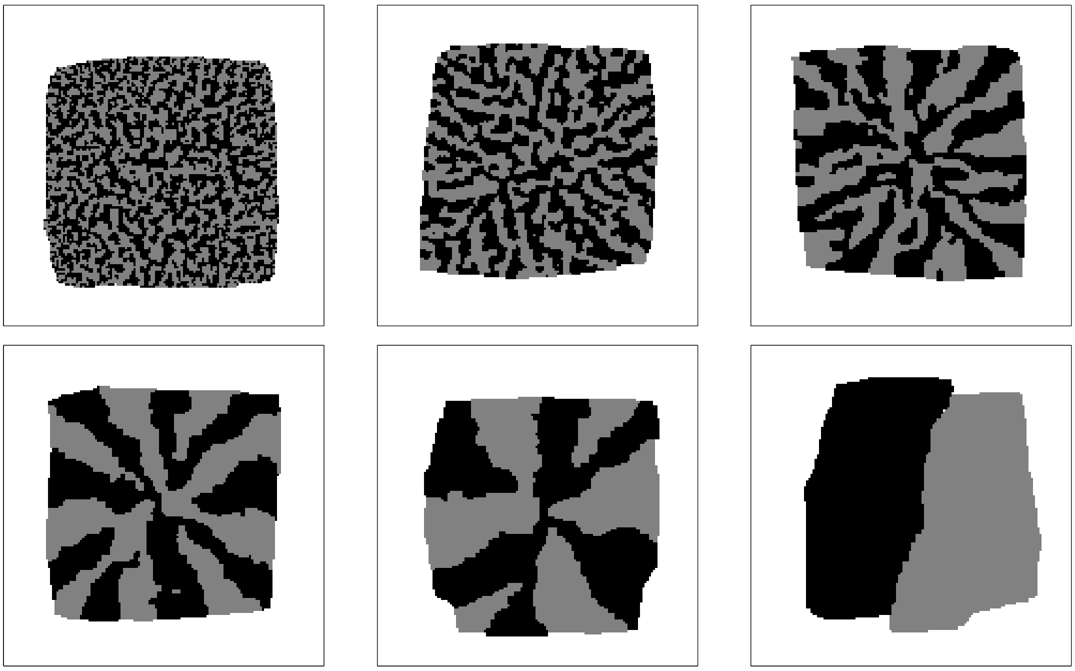

Figure 4.3: Typical island configurations obtained at the end of simulation runs with the symmetric parameter set for $T = 500\,\mathrm{K}$ and different values of $\alpha = E^{\mathrm{AB}}/E^0$: $\alpha = 0.86$, 0.71, 0.59, 0.51, 0.47 and 0.12 (from top left to bottom right). The system size is 150×150 and the total coverage is $\theta = 0.5$.

Figure 4.3 shows snapshots of exemplary system configurations obtained at the end of simulation runs for different values of $\alpha = E^{\mathrm{AB}}/E^0$. For the whole range of α values one observes compact island shapes with the island boundaries roughly parallel to the lattice directions. The weaker binding energy between A particles (dark gray) and B particles (light gray) leads to an aggregation of particles of the same type in clusters which can be characterized as stripes. For the higher values of α these stripes are rather thin and show a considerable degree of irregular intermixing. In the limit $\alpha \to 1$ A and B particles become indistinguishable and the stripe structures of Fig. 4.3 completely vanish in favor of compact islands with randomly distributed light and dark gray areas.

For intermediate values of α the stripes become much thicker and their average size increases with decreasing E^{AB}. Furthermore, there is a tendency for them to stretch outwards and become wider during growth. At a certain stage of the island growth a

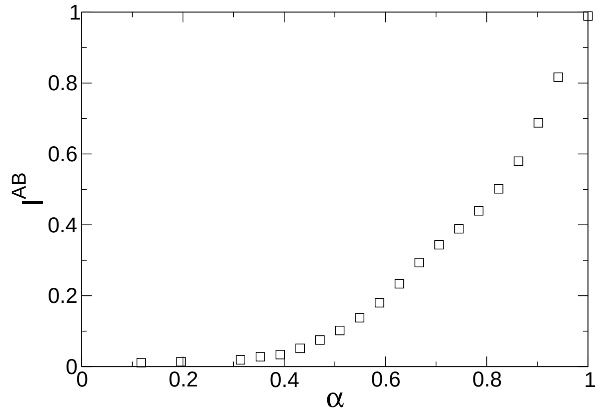

Figure 4.4: Normalized length of the A–B interface for island configurations like the ones from Fig. 4.3 in dependence on $\alpha = E^{\mathrm{AB}}/E^0$. Each value is obtained by averaging over ten independent simulation runs. Errorbars are smaller than the symbol size.

stripe of one particle type may become wide enough for particles of the other type to form a stable nucleus within this stripe, thus leading to a branch-like structure. For low values of α there are only a few big clusters with sizes comparable to the system size, and in the limit $\alpha \to 0$ the separation of A and B particles is more or less complete such that the branching is no longer noticeable.

Figure 4.4 shows the length of the A–B interface (i.e. the number n^{AB} of A–B bonds) normalized by the total number of adsorbate particles $n = n^{\mathrm{A}} + n^{\mathrm{B}}$ in dependence on α. The ratio $l^{\mathrm{AB}} = n^{\mathrm{AB}}/n$ is directly related to the compactness of the A and B clusters: a low value of l^{AB} corresponds to large compact clusters whereas many small clusters imply a high value of l^{AB}. From Fig. 4.4 it can be seen that l^{AB} increases monotonously with increasing α from a value close to zero for low α to a value close to unity at $\alpha = 1$. Both limits may be readily explained: for $\alpha \to 0$ the island consists only of one compact A and B cluster with a more or less straight interface between them. The length of this interface, that is the number n^{AB} of A–B bonds, scales with the square root of the number of adsorbate particles, $n^{\mathrm{AB}} \sim \sqrt{n}$. Consequently, the ratio $l^{\mathrm{AB}} = n^{\mathrm{AB}}/n \sim 1/\sqrt{n}$ goes to zero for n becoming large. On the other side, for $\alpha = 1$ ($E^{\mathrm{AB}} = E^0$) the types of two NN particles are completely uncorrelated, as discussed above. Assuming an ideal square island with n particles the total number of NN bonds is $2(n - \sqrt{n})$ where the second term accounts for the reduced number of bonds at the island boundary. Given any two NN particles, the probability for them not being of the same type is 1/2. This yields $n^{\mathrm{AB}} = n - \sqrt{n}$ for the number of A–B bonds in the island and thus $l^{\mathrm{AB}} = 1 - 1/\sqrt{n} \approx 1$ for large n.

4.2.2 Equilibrium Simulations

The occurrence of stripe-like structures and branching in Fig. 4.3 must be attributed to the kinetic segregation of A and B particles during the island growth. From thermodynamic considerations one would expect more or less complete separation of both particle types for not too high temperatures and not too large values of the inter-species binding energy E^{AB}. We test this assumption by performing canonical equilibrium simulations where the adsorbate coverage remains constant. Since we are not interested in *how* the

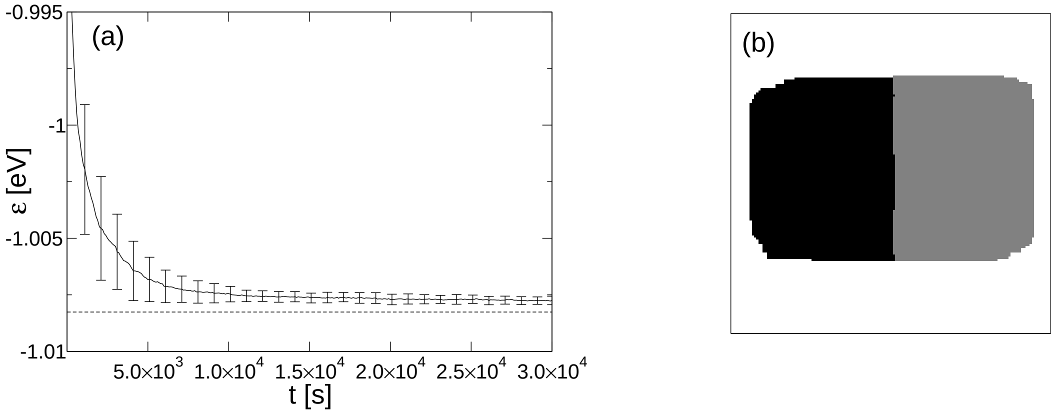

Figure 4.5: Equilibrium simulation at $T = 500\,\mathrm{K}$ for $E^0 = 0.51\,\mathrm{eV}$ and $E^{\mathrm{AB}} = 0.26\,\mathrm{eV}$. (a) Time dependence of the total energy per adsorbate particle. The values are obtained by averaging over ten independent simulation runs. Errorbars are given by the standard deviation. The dashed line marks the theoretical value for the minimum energy configuration at $T = 0\,\mathrm{K}$ given by Eq. (A.5). (b) Typical system configuration at $t = 3 \times 10^4\,\mathrm{s}$. A 150×150 section of the 250×250 system is shown.

system approaches equilibrium we apply a simulation scheme with non-local dynamics where in each step an A or B particle from site i may jump to *any* vacant lattice site j of the system [11, 61]. This yields considerably faster equilibration compared to the local Kawasaki dynamics with NN diffusion only. The details of the simulation algorithm are described in App. A.1.

For the simulations we prepare a square substrate with A and B particles randomly distributed, and the number $n = n^{\mathrm{A}} + n^{\mathrm{B}}$ and ratio $n^{\mathrm{A}}/n^{\mathrm{B}}$ being the same as at the end of the KMC simulations from above. Here, we have to take care of a effect which is caused by our use of periodic boundary conditions: since in the KMC simulations $\theta > \theta_c = 1/4$ the minimum energy configuration for $T = 0\,\mathrm{K}$ would be given by a band which wraps around the boundaries, see App. A.2. In order to avoid simulation runs being trapped in this somewhat artificial configuration we increase the system size from $N = 150$ to $N' = 250$. Thus, the coverage decreases from $\theta = 0.5 > \theta_c$ to $\theta' = \theta\,(N/N')^2 = 0.18 < \theta_c$ while the number of adsorbate particles $n = N\theta^2 = N'\theta'^2$ remains constant. The resulting equilibrium shapes may then be compared with the KMC simulation results.

Figure 4.5(a) shows the time dependence of the total energy per particle ϵ obtained by equilibrium simulations for $E^{\mathrm{AB}} = 0.26\,\mathrm{eV}$ ($\alpha = 0.51$) at $T = 500\,\mathrm{K}$. Similar results are obtained for a range of E^{AB} values. As one can see, ϵ converges to a value slightly above the one corresponding to the theoretical minimum energy configuration at $T = 0\,\mathrm{K}$ (dashed line) which is given by Eq. (A.5) of App. A.2: $\epsilon = -2E^0 + 2E^0\sqrt{2-\alpha}/(N\sqrt{\theta}) \approx -1.008\,\mathrm{eV}$.

Figure 4.5(b) shows a typical system configuration obtained after $3 \times 10^4\,\mathrm{s}$ simulated time which confirms that A and B particles separate and due to the attractive binding energy E^{AB} form a single rectangular island consisting of one A and one B region. The interface between the A and the B region is not perfectly straight and the island edges are rounded, in accordance with theoretical calculations which yield $T_R = 0$ as roughening temperature of two-dimensional crystals. Thus, at any finite temperature neither facets nor angular points are expected [3]. Note that the ratio d_x/d_y of the island diameters in x- and y-direction is close to 1.5 and not to 1 which would be the case if A and B particles were indistinguishable, i.e. $E^{\mathrm{AB}} = E^0$ (cf. App. A.2).

In conclusion, our equilibrium simulations confirm the above stated assumption that the formation of stripes and the branching during growth are caused by the kinetic segregation of adsorbate particles under the non-equilibrium growth conditions. Under equilibrium conditions we observe separation of the different species into very large domains. Note that an increase of the temperature in the growth simulations results in an enhanced mobility of the diffusing adsorbate particles which in turn leads to a more efficient segregation of A and B particles. For a given value of E^{AB} the stripes thus become thicker with increasing temperature as was observed in comparative KMC simulations with temperatures up to 600 K.

4.2.3 Step Geometry

Due to the square lattice and the island topology chosen the grown stripe-structures from Sec. 4.2.1 exhibit a fourfold symmetry. In the following we focus on the stripe formation in only one growth direction. For this purpose we choose a different growth topology for our simulations where the growth proceeds from a step edge. All other parameters are the same as in Sec. 4.2.1.

We assume that our $N \times M$ system represents one particular terrace of a vicinal surface with elongated terraces of constant width M as depicted in Fig. 4.6. Therefore we use periodic boundary conditions in the direction parallel to the step edge (x-direction). In the perpendicular y-direction the system is bounded by the lower part of a step edge at $y = 0$ and the upper part of the next step edge at $y = M$, see Fig. 4.6. Adsorbate particles may attach to and diffuse at the lower part of the step edge where we choose E^0 and B^0 for the interaction between adsorbate particles and the step edge. At the upper part of the next step edge adsorbate particles are reflected, again representing

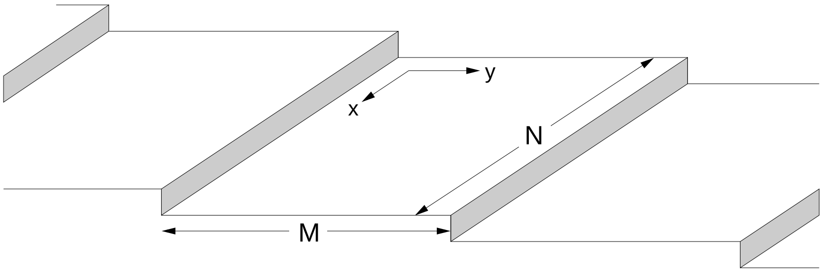

Figure 4.6: Illustration of the step geometry: $N \times M$ system bounded by two consecutive steps of a vicinal surface.

an infinite Ehrlich-Schwoebel barrier for interlayer jumps.

The terrace width is set to $M = 100$ in our simulations. Since for the used parameter set the diffusion length [3] of free adsorbate particles is large compared to the terrace width, newly deposited adatoms are very likely to attach to the step edge at $y = 0$. Thus, terrace nucleation is suppressed and growth proceeds from the step edge.

4.2.4 Influence of the Binding Energy

Figure 4.7 shows snapshots of exemplary system configurations obtained at the end of simulation runs for $N = 512$ and different values of $\alpha = E^{\mathrm{AB}}/E^0$. The difference between E^{AB} and E^0 leads to a separation of A and B particles in stripe-like clusters. The average thickness of the stripes tends to increase with a decreasing value of E^{AB}. For low E^{AB} A and B clusters are well separated and almost always extend from the step edge to the free surface. With increasing E^{AB} though they become more and more intertwined. These observations can be explained by the fact that with decreasing E^{AB} it is more favorable for A and B particles to attach to particles of the same type. We notice further that there is no clear orientation of the stripes, for example parallel to the growth (y-) direction. On the contrary, stripes of one particle type may very well grow sideways leading to a rough stripe interface, as can be seen best in the bottom panel of Fig. 4.7. We also observe that for all values of E^{AB} the profiles of the grown films are rather rough. This is caused by two different effects: on the one hand the enhanced barrier for A particles crossing an A–B interface (and vice versa), leads to preferential nucleation near the interfaces. This is the dominant effect for low values of E^{AB} as can be seen by the large protrusions in the bottom panel of Fig. 4.7. On the other hand, there is a reduced probability for particles to diffuse around a corner since this implies detachment from the step edge which is energetically costly. This leads to the characteristic crevices in the simulations with higher values of E^{AB} (cf. the upper panels of Fig. 4.7) and will be discussed in more detail in Sec. 4.2.6.

We now have a closer look at the influence of E^{AB} on the stripe width. Due to the absence of straight interfaces and the considerable degree of irregularity for the higher values of E^{AB} the stripe width determination cannot be done straightforwardly by, e.g., means of Fourier transform. Instead we calculate for each connected cluster of A particles the ratio between its perimeter length and its volume. This is done by counting the number of perimeter particles n_p together with the total number of particles n_c in the same cluster and forming the ratio $\Lambda = n_p/n_c$. The average of Λ over all clusters should then give a measure for the average thickness of the clusters. For example, for a rather thin cluster most of its particles sit at the edge and therefore Λ should be close to 1, whereas with increasing cluster thickness Λ should decrease towards 0. For each value of E^{AB} we perform ten independent simulation runs and average over the occurring A clusters. To get a better statistics the clusters are initially sorted by their size and very small clusters ($< 0.2\times$ the mean cluster size), for which $\Lambda \approx 1$ holds, are omitted from averaging.

Figure 4.8 shows the dependence of Λ on $\alpha = E^{\mathrm{AB}}/E^0$. As one sees Λ increases

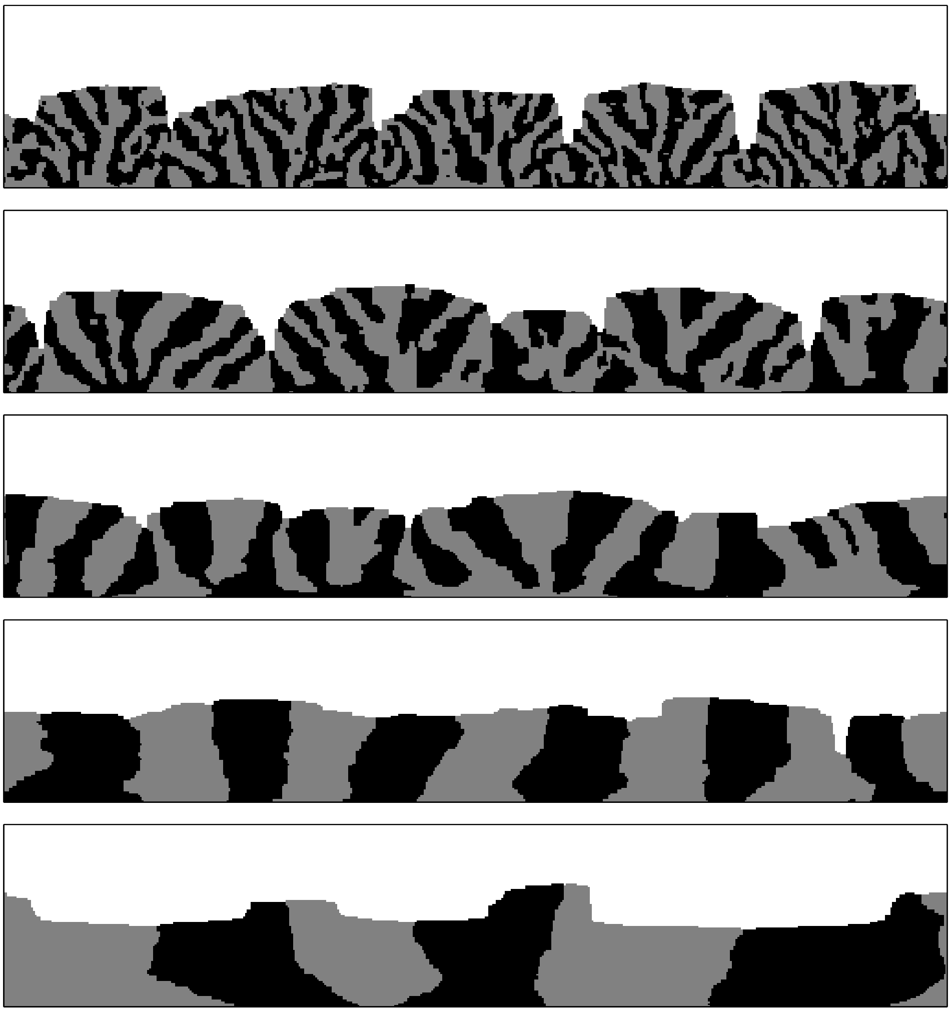

Figure 4.7: System configurations obtained at the end of simulation runs with the step geometry for different values of $\alpha = E^{\mathrm{AB}}/E^{0}$: $\alpha = 0.63$, 0.55, 0.47, 0.39 and 0.31 (from top to bottom). A particles appear dark gray, B particles are light gray. The system size is 512×100.

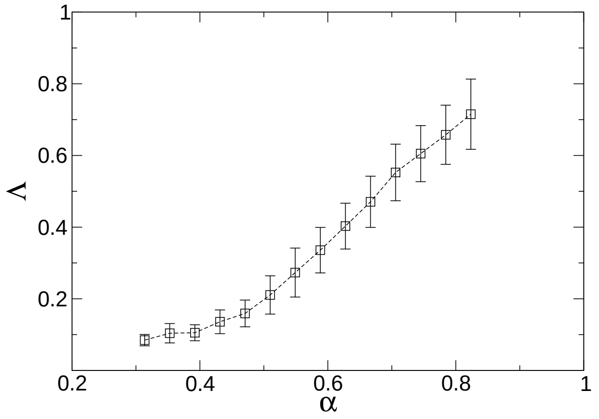

Figure 4.8: Dependence of Λ on $\alpha = E^{\mathrm{AB}}/E^0$. Each value is obtained by averaging over the A clusters of ten independent simulation runs. Errorbars are given by the standard deviation.

monotonously with increasing α confirming that the stripe width decreases with the difference in binding energies becoming smaller. The errorbars in Fig. 4.8 indicate that the stripes become more uniform in size with decreasing E^{AB} which can also be noticed in Fig. 4.7. For $\alpha = 0.31$ we obtain $\Lambda \approx 0.08$. This is close to the value $4(N+M)/(NM) \approx 0.05$ which we would expect in the limit $\alpha \to 0$ if all A particles assembled in a single rectangular cluster of length $N/2$ and width $M/2$. When α approaches 1, Λ also should tend to 1 because A and B particles should then be perfectly mixed, since there is no longer a preference for a particle to stick to its own kind (cf. Sec. 4.2.1). Accordingly, most of the clusters contain $\mathcal{O}(1)$ particles which results in $\Lambda \approx 1$. This assumption is clearly supported by the behavior of Λ as shown in Fig. 4.8.

4.2.5 Influence of the Adsorbate Concentration

In the preceding sections we have seen that the reduced binding energy E^{AB} between A and B particles may lead to stripe formation where the stripe width increases with decreasing E^{AB}. In the following we will investigate the influence of another control parameter, namely the concentration of one particle species, on the stripe width. Therefore the A particle flux F^{A} is varied between $10^{-3}\,\mathrm{ML\,s^{-1}}$ and $5 \times 10^{-3}\,\mathrm{ML\,s^{-1}}$ leaving the total flux $F^{\mathrm{A}} + F^{\mathrm{B}} = 10^{-2}\,\mathrm{ML\,s^{-1}}$ constant. Again, we start our simulations with an empty substrate and subsequently co-deposit A and B particles until a total adsorbate coverage of 0.5 is reached.

Figure 4.9 shows simulation results for $\alpha = 0.31$ (left column) and $\alpha = 0.51$ (right column). The picture shows that for an increasing A particle flux the width of the A stripes seems to increase which is understandable because due to the higher binding energy additional A particles are more likely to stick to existing A clusters than form new nuclei within regions of B particles. The tendency for the stripes to become thinner with increasing E^{AB}—noticed already in the previous section for equal A and B fluxes—applies for all ratios $F^{\mathrm{A}}/F^{\mathrm{B}}$ of the particle fluxes. Furthermore, the rough surface profile is clearly visible.

In order to quantify the stripe width we measure again the quantity Λ as in the simulations before. Figure 4.10 shows the dependence of Λ on the A particle flux F^{A}

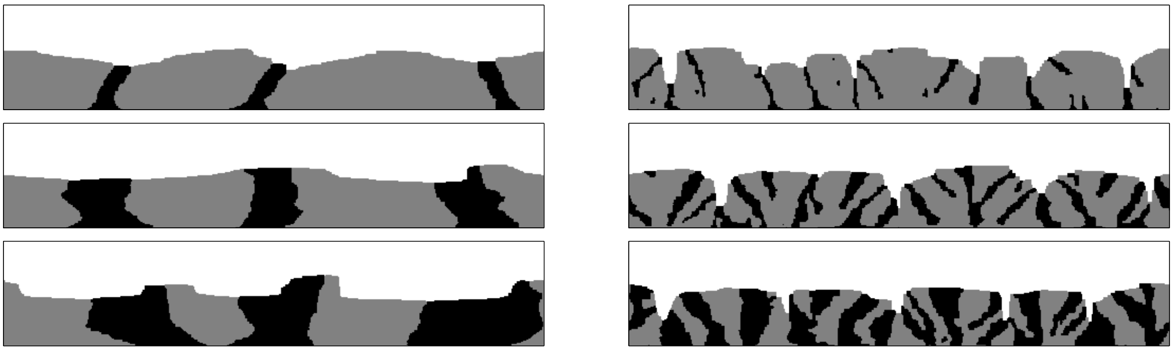

Figure 4.9: Simulation results for $\alpha = 0.31$ (left column), $\alpha = 0.51$ (right column) and $F^{\mathrm{A}} = 10^{-3}\,\mathrm{ML\,s^{-1}}, 3 \times 10^{-3}\,\mathrm{ML\,s^{-1}}$ and $5 \times 10^{-3}\,\mathrm{ML\,s^{-1}}$ (top to bottom). A particles appear dark gray, B particles are light gray. The system sizes are 512×100 and the total flux is $F^{\mathrm{A}} + F^{\mathrm{B}} = 10^{-2}\,\mathrm{ML\,s^{-1}}$.

for various values of α which confirms the assumptions from above: for all values of α Λ decreases with increasing A flux, indicating that the average stripe width increases. Also, for a fixed value of the A flux Λ increases with increasing α, that is the stripes become thinner on average. The errorbars in Fig. 4.10 indicate that, apart from the rough surface profile, for low values of α we obtain a rather narrow distribution of stripe widths. This implies that for systems with a weak binding energy E^{AB} between A and B particles—compared to the one between particles of the same type—the kinetic phase separation may indeed yield well-ordered arrays of stripes of about equal width.

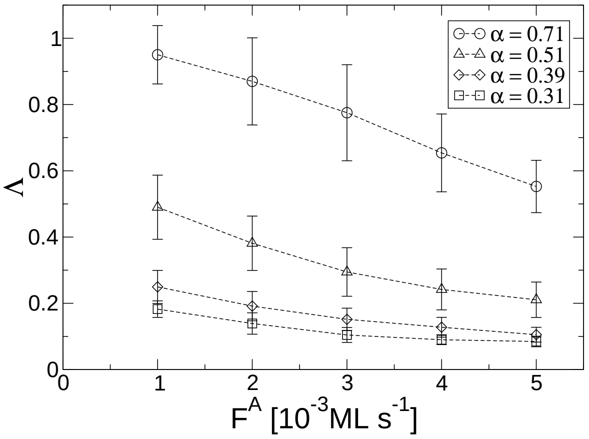

Figure 4.10: Dependence of Λ on the A particle flux F^{A} (with $F^{\mathrm{A}} + F^{\mathrm{B}} = 10^{-2}\,\mathrm{ML\,s^{-1}}$) for different values of $\alpha = E^{\mathrm{AB}}/E^{0}$. Each data point is obtained by averaging over clusters from ten independent simulation runs.

4.2.6 Kinetic Instability

From Figs. 4.7 and 4.9 one observes that for the higher values of E^{AB} the grown film structures are split into several blocks divided by deep crevices leading to a rough surface profile. This behavior reveals a kinetic growth instability, similar to the Bales-Zangwill instability for stepped surfaces [4,92], and is due to a reduced corner rounding

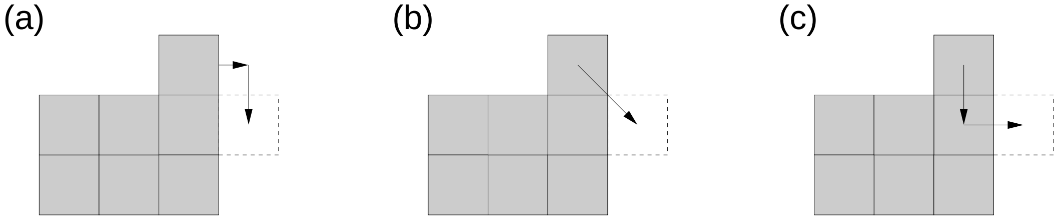

Figure 4.11: Corner diffusion mechanisms. (a) Two consecutive NN diffusion steps. (b) One NNN diffusion step. (c) Exchange diffusion.

probability of adsorbate particles [93].

Since in our model we consider only diffusion jumps to NN sites the diffusion past the outside of a corner requires two steps, see Fig. 4.11(a). First, a particle has to detach from the step edge which implies crossing an enhanced energy barrier and therefore is less favorable than diffusion at the step edge. In fact, this additional barrier can be thought of as an Ehrlich-Schwoebel barrier for step edge diffusion [41]. Second, after detachment the now free particle has to attach again at the other side of the corner which happens with a probability of 1/4 since all four diffusion directions are equivalent. As a consequence, the process of corner rounding is strongly inhibited. If now at some stage during growth a small indentation forms by local fluctuations, it may develop into a deep crevice as—due to the argument given above—the filling through particles diffusing at the step edge is suppressed. In principle, such a crevice can also be filled up by newly deposited particles. However, the probability for a particle to be deposited right into the crevice is comparatively low.

In order to determine the influence of the reduced corner rounding we now compare two different diffusion modes: in the first case only NN diffusion is allowed as in the simulations before. In the second case we include diffusion jumps to next nearest neighbor (NNN) sites which implies that only one (diagonal) jump is needed for a particle to get around a corner, see Fig. 4.11(b). As consequence of the chosen dynamics [Eq. (4.3)] the energy barrier for such a corner rounding step is the same as for diffusion at the step edge.

In many experimental systems corner diffusion affects significantly the morphologies of growing islands (compact or fractal, see, e.g., [94–96]). Two different atomic mechanisms are discussed in this context [97]: a particle at the step edge may either get around the corner by single diffusion steps [cf. Fig. 4.11(a)], or the corner rounding is achieved via a concerted move of that edge particle and the one sitting in the corner. In the latter scenario the corner particle is pushed out by the edge particle, see Fig. 4.11(c). Such exchange processes which are also relevant in the case of terrace and interlayer diffusion [15, 33, 44, 98] may serve as motivation for including NNN diffusion in our simulations, see Fig. 4.11(b).

The simulations are carried out with only one adsorbate species, which corresponds to the limit $E^{\mathrm{AB}} = E^0$, and the profile roughness of the growing film given by $w = \sqrt{<y^2> - <y>^2}$ is measured [4]. Here, $y = y(x)$ denotes the maximal y-coordinate of

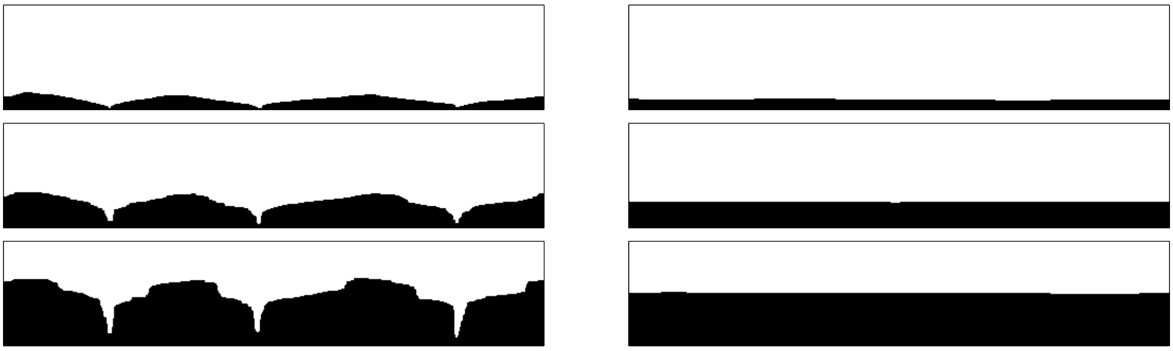

Figure 4.12: Surface configurations obtained for simulations with NN diffusion only (left column) and with NNN diffusion included (right column). The coverages are $\theta = 0.1$ (top), $\theta = 0.25$ (middle) and $\theta = 0.5$ (bottom). Only 512×100 sections of the 1024×100 systems are shown.

the growing film at given x-position, and $< \cdot >$ means the average over all x-positions.

Figure 4.13 shows the dependence of w on the adsorbate coverage θ for the two different situations. For the case of NN diffusion only and coverages up to ≈ 0.1 we find a power-law increase $w \sim \theta^{\beta}$ of the surface roughness with a growth exponent $\beta \approx 0.52$ comparable to the one for $1d$ random deposition [4]. For $\theta > 0.1$ the above mentioned crevices begin to evolve leading to a slightly faster increase of w. The left column of Fig. 4.12 shows corresponding system configurations for $\theta = 0.1, 0.25$ and 0.5. The development of the growth instability is clearly visible: in the initial stage of growth adsorbate particles form immobile nuclei at the step edge which then serve as nucleation centers for additional particles. Thus several mounds form which grow both in x- and y-direction. Since corner rounding is inhibited there is a net inward current of particles in the upper layers of each mound. This leads to a wavy profile, see Fig. 4.12 (top left), with indentations at the locations where the bases of two mounds meet. This meeting occurs at a coverage $\theta \approx 0.1$ and the indentations are then in turn amplified by the reduced corner rounding and develop into deep crevices, see Fig. 4.12 (middle

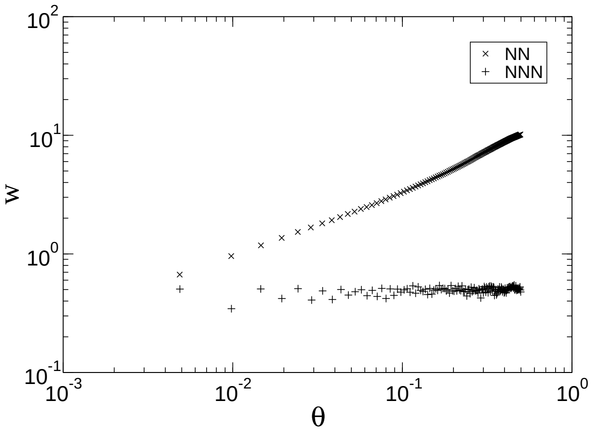

Figure 4.13: Dependence of the profile roughness on the coverage for the case of NN diffusion only (×) and with NNN diffusion included (+). Each data point is obtained by averaging over ten independent simulation runs.

and bottom left).

The situation is completely different for the case where NNN diffusion is included. Here, particles may easily get around a corner and growth proceeds in a layer-by-layer fashion, as can be seen in Fig. 4.12 (right column). Hence, the profile remains basically flat during the simulations and w merely fluctuates around a low value of ≈ 0.5, see Fig. 4.13. This is in agreement with recent investigations on unstable epitaxial growth in simple cubic geometries. Here, compact island morphologies with straight edges along the $\langle 100 \rangle$ and $\langle 010 \rangle$ directions have been observed in the presence of strong corner diffusion [41, 99, 100].

In conclusion, we find that the formation of crevices in the simulations with high E^{AB} reflects a generic growth instability which is due to the reduced corner rounding probability in the model with NN diffusion only. Note that with decreasing E^{AB} the formation of crevices is less pronounced, cf. Figs. 4.7 and 4.10, since, e.g., A particles may round a B corner more easily (and vice versa) due to the reduced detachment barrier. The surface profiles though still are rather rough.

In principle, the discussed growth instability should also be observable in the island geometry investigated in Sec. 4.2.1. However, the distance of the crevices in the film structures grown with the step geometry suggests that for the given values of the parameters (e.g. temperature) this should occur on length scales which exceed the used system size.

4.3 Simulations with Next Nearest Neighbor Diffusion

In this section we will further concentrate on simulations with NNN diffusion included. Based on the observations from the previous section we conjecture not only smoother surface profiles in this case but also straighter interfaces between A and B regions leading to a more well-defined wavelength of the stripe patterns. Due to the NNN diffusion the number of possible diffusion events for a free particle doubles (4 NN sites + 4 NNN sites). In order to avoid a slowing-down of the simulations caused by excessive terrace diffusion we adopt a further simplification. Whenever a deposition event occurs the newly arrived particle is placed directly at the growing film interface at random position. This deposition scheme is similar to the ones applied in a wide range of one-dimensional SOS growth models [4]. Since the profile roughness is small (cf. Fig. 4.13) the modified deposition mechanism has no impact on the growing morphologies as was confirmed by us in comparative simulations with “normal” deposition.

4.3.1 Influence of the Binding Energy

We first check on the E^{AB} dependence of the stripe width for a fixed temperature $T = 450\,\mathrm{K}$. We perform simulations for various values of $\alpha = E^{\mathrm{AB}}/E^0$. The system sizes are chosen to be 1024×100 and the remaining parameters are the same as above.

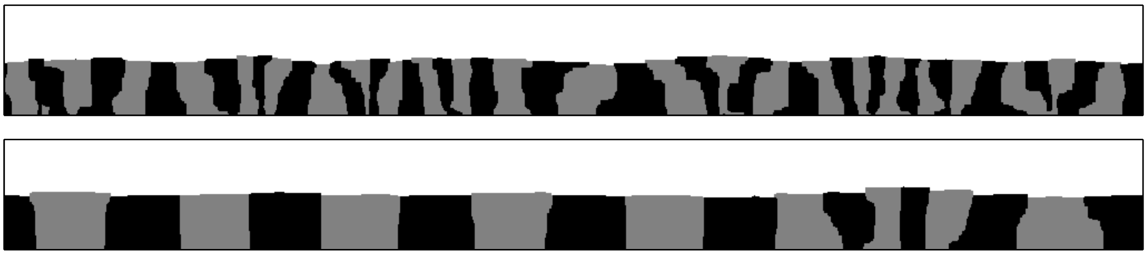

Figure 4.14: Surface snapshots at the end of simulation runs with NNN diffusion and $T = 450\,\text{K}$. $E^{\text{AB}}/E^0 = 0.51$ (top) and $E^{\text{AB}}/E^0 = 0.31$ (bottom). The system size is 1024×100 and the total coverage is $\theta = 0.5$.

Figure 4.14 shows simulation results for $\alpha = 0.51$ and $\alpha = 0.31$. As expected the surface profiles are much smoother than for the simulations with NN diffusion only. The stripes extend from the step to the free interface and the stripe width increases with decreasing E^{AB} as before. For the lower value of E^{AB} both stripes with straight interfaces and rough interfaces are observed whereas for higher E^{AB} the stripe interfaces are always quite rough. In order to derive the stripe width λ we make a one-dimensional cut through the film parallel to the step edge at $y = 40$, which is ten lattice sites below the average y-value of the film profile. From this one-dimensional section λ is obtained by averaging over the widths of all A regions. Figure 4.15 shows the average width λ of the A stripes in dependence on the scaled A–B binding energy. Similar to the simulations with NN diffusion only (cf. Sec. 4.2.4) the stripe width increases with decreasing α as it becomes more favorable for particles to stick to their own kind.

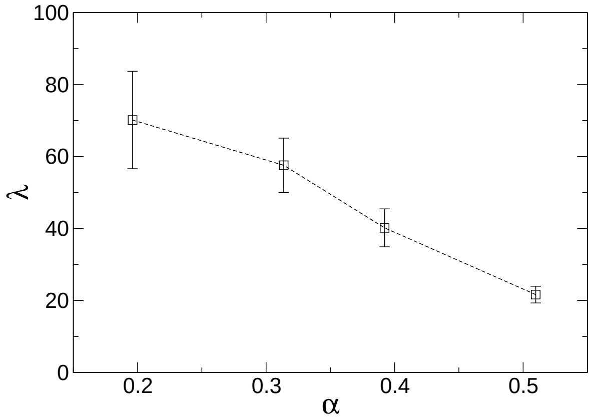

Figure 4.15: Dependence of the A stripe width on $\alpha = E^{\text{AB}}/E^0$ for $T = 450\,\text{K}$. Errorbars are given by the standard deviation.

It is remarkable that for low values of E^{AB} both stripes with straight interfaces and stable width occur together with stripes with rough interfaces and large fluctuations of their width. Later, we will argue that for this type of simulations indeed a broad range of stripe widths is at least metastable under growth conditions.

4.3.2 Influence of the Adsorbate Concentration

In order to determine the dependence of the stripe width on the concentration of one adsorbate species we perform simulations with variable A particle flux F^{A} and constant total flux $F^{\mathrm{A}} + F^{\mathrm{B}} = 10^{-2}\,\mathrm{ML\,s^{-1}}$ as in Sec. 4.2.5. Figure 4.16 shows typical surface configurations for $F^{\mathrm{A}} = 10^{-3}\,\mathrm{ML\,s^{-1}}, 3 \times 10^{-3}\,\mathrm{ML\,s^{-1}}$ and $5 \times 10^{-3}\,\mathrm{ML\,s^{-1}}$ (from top to bottom), and in Fig. 4.17 the width of both A and B stripes is plotted versus the A particle flux.

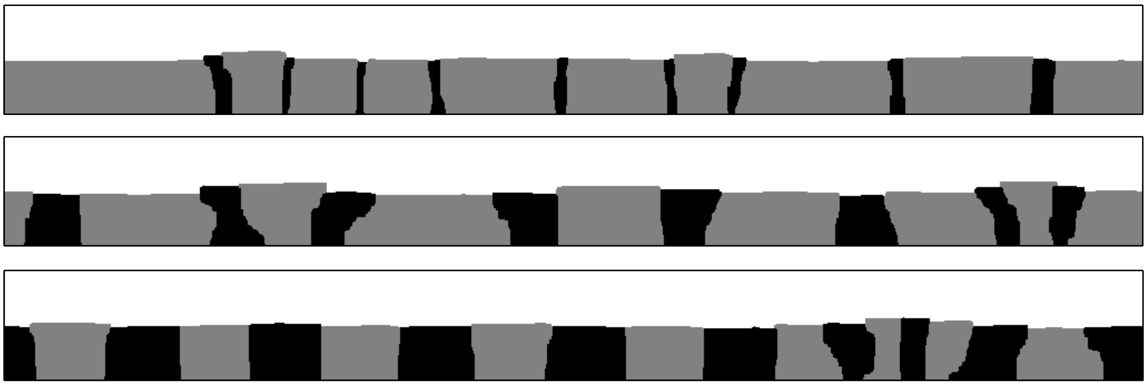

Figure 4.16: Surface snapshots at the end of simulation runs with NNN diffusion, $E^{\mathrm{AB}}/E^{0} = 0.31$ and $T = 450\,\mathrm{K}$ for $F^{\mathrm{A}} = 10^{-3}\,\mathrm{ML\,s^{-1}}, 3 \times 10^{-3}\,\mathrm{ML\,s^{-1}}$ and $5 \times 10^{-3}\,\mathrm{ML\,s^{-1}}$ (top to bottom). The system size is 1024×100 and the total flux is $10^{-2}\,\mathrm{ML\,s^{-1}}$.

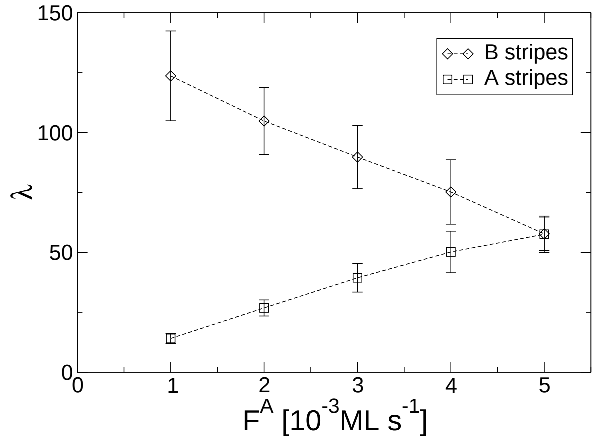

Figure 4.17: Dependence of the width of A and B stripes on the A particle flux F^{A} (with $F^{\mathrm{A}} + F^{\mathrm{B}} = 10^{-2}\,\mathrm{ML\,s^{-1}}$) for $\alpha = 0.31$ and $T = 450\,\mathrm{K}$. Each data point is obtained by averaging over ten independent simulation runs. Errorbars are given by the standard deviation.

The A stripes become thicker with increasing A particle concentration while the number of stripes stays about the same as can be seen from Fig. 4.16. Conversely, the width of the B stripes decreases on average. However, already for low values of F^{A} both thick and thin B stripes exist, as can be seen from the top panel of Fig. 4.16. This observation is also confirmed by the relatively large errorbars of the B stripe width, as shown in Fig. 4.17.

Since the width of the B stripes directly corresponds to the distance between A stripes this implies that for low A particle concentration the A stripes—although rather uniform in their width—are not at all uniformly spaced. In order to obtain film configurations where both A *and* B stripes have a narrow width distribution additional size-limiting mechanisms have to be present as will be discussed further below.

4.3.3 Temperature Dependence

Since the separation of A and B particles is driven by thermally activated adatom diffusion we expect a strong dependence of the domain sizes on the growth temperature which is another important control parameter. In this section we will investigate the temperature dependence of the stripe width for fixed values of the A–B binding energy and particle fluxes. Therefore we perform simulations with $E^{\mathrm{AB}}/E^0 = 0.31$, $F^{\mathrm{A}} = F^{\mathrm{B}} = 5 \times 10^{-3}\,\mathrm{ML\,s^{-1}}$, and different temperatures T. Figure 4.18 shows typical system configurations at the end of simulation runs with $T = 350\,\mathrm{K}, 400\,\mathrm{K}, 450\,\mathrm{K}$ and $500\,\mathrm{K}$ (from top to bottom). As one can see the average stripe width becomes larger with increasing temperature. For high temperatures both diffusion at and detachment from step edges become more likely. Thus, adsorbate particles may sample a larger region of the system and may find the energetically most favorable sites—that is, sites with many NN of the same particle type—more frequently than at low temperatures. Hence, larger stripes form at higher temperatures. We notice further that, similar to decreasing E^{AB}, increasing the temperature yields a higher percentage of stripes with straight interfaces.

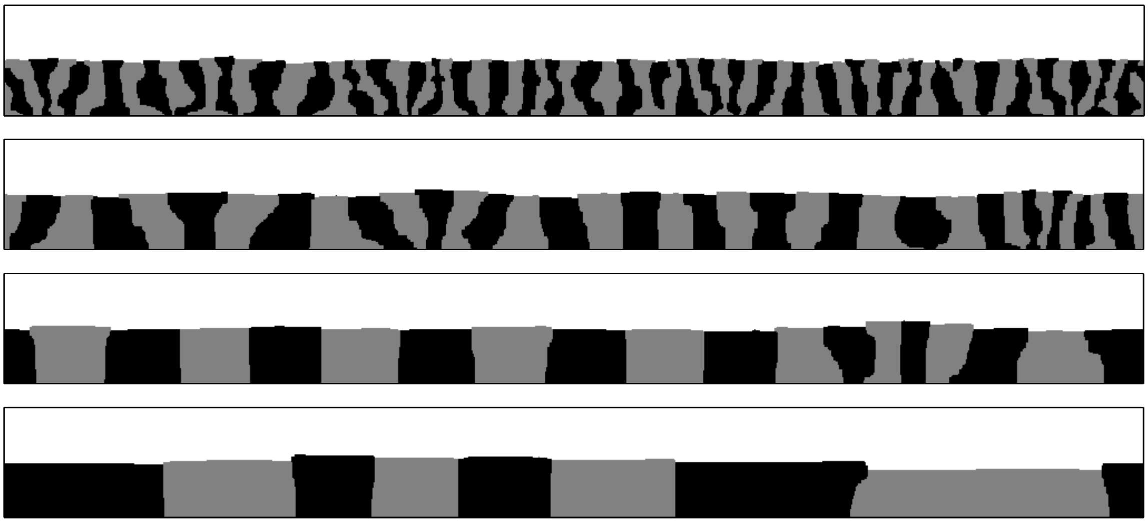

Figure 4.18: Surface snapshots at the end of simulation runs with NNN diffusion, $E^{\mathrm{AB}}/E^0 = 0.31$ and $F^{\mathrm{A}} = F^{\mathrm{B}} = 5 \times 10^{-3}\,\mathrm{ML\,s^{-1}}$ for $T = 350\,\mathrm{K}, 400\,\mathrm{K}, 450\,\mathrm{K}$ and $500\,\mathrm{K}$ (top to bottom). The system size is 1024×100 and the total coverage is $\theta = 0.5$.

In Fig. 4.19 we have plotted the average width λ of the A stripes on a logarithmic scale versus the inverse temperature (Arrhenius plot) which shows that in the range 325 K − 500 K the stripe width can be described by an Arrhenius law $\lambda \sim \exp\left[-E_a/(k_B T)\right]$ quite well (dashed line). As activation energy we obtain $E_a \approx 0.183\,\text{eV}$. This behavior agrees with experimental findings for lateral phase separation in epitaxial layers of binary [101] or ternary [102] systems where also an Arrhenius type temperature dependence of the domain sizes has been observed. In [102] the wavelength λ of the composition modulation is related to the surface diffusion coefficient D_s by $\lambda^2 \sim D_s$ which in turn yields $\lambda^2 \sim \exp\left[-E_s/(k_B T)\right]$ for the temperature dependence. Here, E_s is the activation energy for surface diffusion of the atomic constituent that is rate controlling. The above argument yields $E_s = 2\,E_a = 0.366\,\text{eV}$ which is indeed close to the diffusion barrier $B^0 = 0.37\,\text{eV}$ for free surface diffusion and diffusion at step edges in our model.

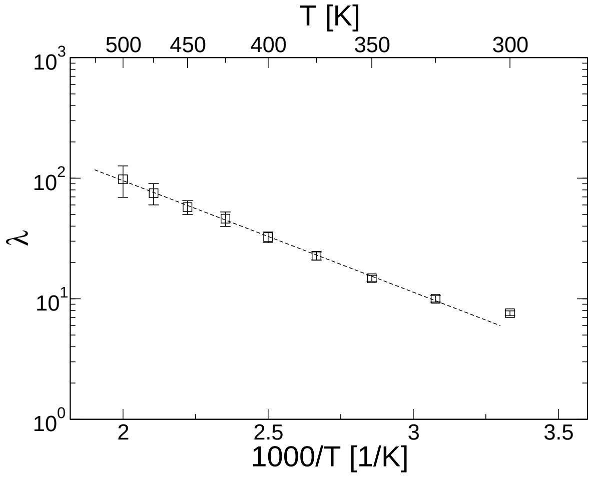

Figure 4.19: Temperature dependence of the stripe width for $E^{\text{AB}}/E^0 = 0.31$. Each data point is obtained by averaging over ten independent simulation runs. Errorbars are given by the standard deviation. The dashed line represents an Arrhenius fit to the data with $T > 300\,\text{K}$.

From the simulations with NNN diffusion we conclude that the average stripe width can be controlled by the inter-species binding energy E^{AB} as well as the two control parameters temperature and adsorbate particle concentration. In comparison with the simulations with only NN diffusion the film profiles are much smoother and the stripe interfaces are in general less rough. Hereby, a decrease of the binding energy between A and B particles and/or increase of the temperature yields a higher percentage of stripes with straight interfaces. Although the dependence of the *average* stripe width λ on the control parameters is clearly evident—e.g., increase of λ with increasing temperature—rather large fluctuations of λ indicate that both very thin and very thick stripes may coexist, see e.g. Fig. 4.18. The simulations with variable A particle flux showed that for low values of F^{A} the width distribution of the resulting A stripes is rather narrow. However, the distribution of their *distances*—which corresponds to the width of the B stripes—is rather broad, see Fig. 4.16 (top panel).

Simulations of a 1024×100 system at $T = 500\,\text{K}$ and $E^{\text{AB}}/E^0 = 0.31$ with a regular arrangement of alternating A and B stripes of m lattice constants width as initial state show that for $m = 32, 64$ and 128 their width remains almost constant during growth, see Fig. 4.20. A newly deposited particle of, say, A type will either arrive at an A section or B section of the step edge. In the first case, the A particle will sample the

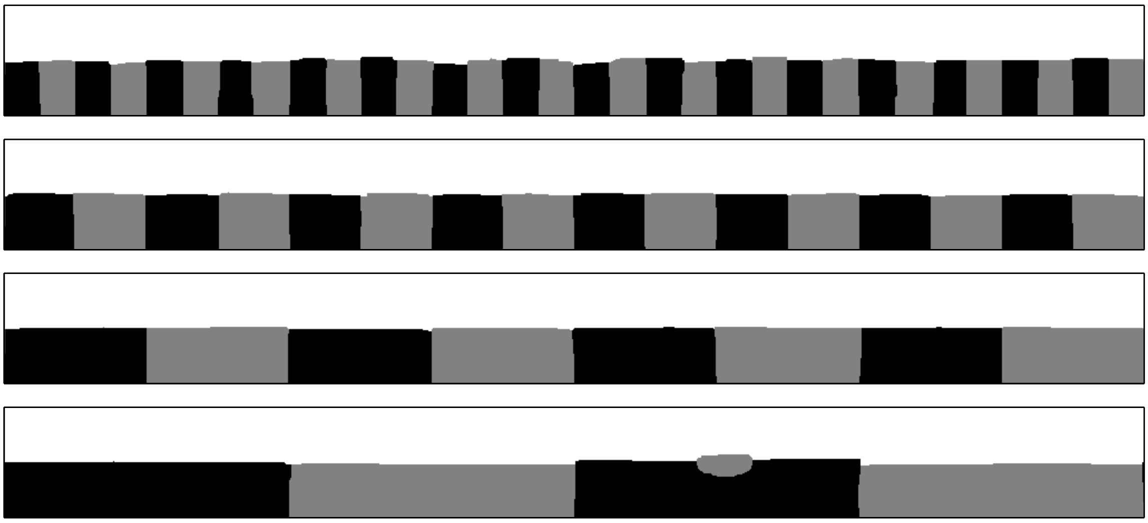

Figure 4.20: Simulation runs for $T = 500\,\mathrm{K}$, $E^{\mathrm{AB}}/E^0 = 0.31$ and alternating A and B stripes of m lattice constants width as initial state. $m = 32, 64, 128$ and 256 (top to bottom). The system size is 1024×100 and the total coverage is $\theta = 0.5$.

A region but is unlikely to detach or cross the A–B interface due to the high energy barriers. In the second case, the particle will diffuse within the B region until it reaches one of the adjacent A regions (there is no extra barrier for diffusion from an A to a B region). Here it will become trapped, again. A similar mechanism applies to the B particles. Thus, the density of A (B) particles in the B (A) regions is very low and both A (B) stripes grow preferentially by nucleation of new A (B) particles leaving their width constant. For $m \geq 256$ we observe nucleation of B particles within A regions and vice versa. In this case, it takes longer for particles to reach the "right" section of the step edge. Thus, the density of A particles in B regions is sufficient to form a stable nucleus as can be seen from the bottom panel of Fig. 4.20.

The results from above suggest that a very broad range of stripe widths is metastable under growth conditions and thus no sharp characteristic stripe width or wavelength emerged in the simulations. In order to obtain a narrow stripe width distribution for both A *and* B stripes additional size-limiting mechanisms are needed apart from the kinetic segregation of A and B particles. In the next section we will see that surface strain caused by the lattice mismatch of the different adsorbate species may serve as such a size-limiting process.

4.4 Off-Lattice Description

In our lattice gas simulations we have concentrated on the influence of different binding energies on the growing film structures, neglecting though all effects caused by elastic interactions. In the following we will also incorporate strain effects which arise from the lattice mismatch of the different material species involved. In order to account for strain effects in a simulation of epitaxial growth it is necessary to overcome the limitations of a pre-defined lattice [17, 103, 104]. This can be achieved, e.g., by means of an off-lattice model developed by Much [105] which has been shown to successfully describe a variety of phenomena observed in strained heteroepitaxial growth like, e.g., dislocation formation or wetting layer and island formation in the Stranski-Krastanov growth mode [105–107]. Here, we consider the application of this method to our studies of surface-confined alloying in multi-component growth. The off-lattice simulation results discussed in the following are provided by courtesy of F. Much [17].

4.4.1 Simulation Model

In the considered off-lattice model two particles which are separated by a *continuous* distance r interact via a simple pair-potential $U(r)$, an example being the Lennard-Jones (LJ) potential [39]

$$U_{\mathrm{LJ}}(r) = 4\,E\left[\left(\frac{\sigma}{r}\right)^{12} - \left(\frac{\sigma}{r}\right)^{6}\right], \tag{4.7}$$

where E determines the depth of the potential and the equilibrium distance between two isolated particles is given by $r_0 = \sqrt[6]{2}\,\sigma$. By appropriate choice of the parameters E and σ, different material properties may be specified in the model qualitatively. For example, interactions between two substrate or adsorbate particles are governed by the sets $\{E_{\mathrm{S}}, \sigma_{\mathrm{S}}\}$ and $\{E_{\mathrm{A}}, \sigma_{\mathrm{A}}\}$, respectively. To keep the number of parameters small the standard choice $E_{\mathrm{AS}} = \sqrt{E_{\mathrm{A}} E_{\mathrm{S}}}$, $\sigma_{\mathrm{AS}} = (\sigma_{\mathrm{A}} + \sigma_{\mathrm{S}})/2$ is used for the interaction between adsorbate and substrate particles [104]. Since the lattice spacing in a Lennard-Jones crystal is proportional to σ [39] the relative lattice misfit ε in the model may directly be controlled by the values of σ_{S} and σ_{A}:

$$\varepsilon = \frac{\sigma_{\mathrm{A}} - \sigma_{\mathrm{S}}}{\sigma_{\mathrm{S}}}. \tag{4.8}$$

In [105–107] rather fundamental aspects of heteroepitaxial growth were studied instead of focusing on specific material properties. In order to save computer time, the simulations therefore were done in $1 + 1$ dimensions. Here, the description of phenomena like the formation of alternating vein structures or ramified growth requires the adaptation of the simulation method to $2 + 1$ dimensions. To keep the computational effort acceptable a simple cubic (sc) symmetry is chosen for the simulations discussed in the following. The advantage is that due to the lower coordination number less particles have to be taken into account for energy calculations than in a closed-packed lattice. In order to stabilize the sc lattice the method proposed in [108] is adapted by choosing

$$V(r) = \left(0.1 + 8\left(\frac{x^2}{r^2} - \frac{1}{2}\right)\left(\frac{y^2}{r^2} - \frac{1}{2}\right)\left(\frac{z^2}{r^2} - \frac{1}{2}\right)\right)U(r) \tag{4.9}$$

as interaction potential between two particles separated by a distance r. Two kinds of pair-potentials $U(r)$ are used: the LJ potential given by Eq. (4.7) and the Morse potential [109]

$$U_{\mathrm{M}}(r) = E\, e^{a(\sigma-r)} \left(e^{a(\sigma-r)} - 2\right) . \tag{4.10}$$

Similar to the LJ potential, the depth of the Morse potential is given by E, and the equilibrium distance between two isolated particles becomes $r_0 = \sigma$. The additional parameter a in Eq. (4.10) determines the steepness of the Morse potential around its minimum. In the simulations, $a = 5.0$, 5.5 and 6.0 are used, corresponding to an increase of the steepness. In order to save computer time, $U(r)$ is cut off for particle distances greater than $r_{cut} = 2\,r_0$ during energy calculations, whereas for the calculation of diffusion barriers the cut-off distance is set to $3\,r_0$. These simplifications are absolutely reasonable since both the LJ and the Morse potential decline fast towards zero with increasing particle distance.

In the following we consider two different adsorbate types, called A and B, with negative and positive misfit, respectively, relative to a substrate S. The interaction strength between two substrate particles is given by E_{S} and $\sigma_{\mathrm{S}} = 1$ whereas E_{A}, σ_{A} and E_{B}, σ_{B} are chosen for A–A and B–B interactions, respectively. The interaction between adsorbate particles of type X $\in$ {A,B} and the substrate is set to $E_{\mathrm{XS}} = \sqrt{E_{\mathrm{X}} E_{\mathrm{S}}}$, $\sigma_{\mathrm{XS}} = (\sigma_{\mathrm{X}} + \sigma_{\mathrm{S}})/2$ whereas E_{AB} and $\sigma_{\mathrm{AB}} = (\sigma_{\mathrm{A}} + \sigma_{\mathrm{B}})/2$ hold for the interaction between A and B adsorbate particles. The misfit is assumed to be symmetric in the system:

$$\sigma_{\mathrm{A}} = 1 - \varepsilon \quad \text{and} \quad \sigma_{\mathrm{B}} = 1 + \varepsilon \tag{4.11}$$

with $\varepsilon > 0$. Although experimental systems fulfill this symmetry only approximately we do not expect this to be crucial and restrict ourselves to a single parameter ε.

The potential depths are chosen in such a way that they meet two demands: on the one hand the ratio between E_{S} and E_{A}, E_{B} is kept fixed for all potentials,

$$E_{\mathrm{A}} = E_{\mathrm{B}} = \frac{1}{6} E_{\mathrm{S}}, \tag{4.12}$$

and is chosen such that substrate particles are bound much more strongly and thus intermixing of adsorbate and substrate particles is suppressed. On the other hand, in the case of homoepitaxy ($\varepsilon = 0$) the diffusion barrier on plain substrate $E_{a,sub}$ should have roughly the same value for all used potentials to facilitate the comparison of the results. The substrate-substrate interaction strength E_{S} is chosen in such a way that in the homoepitaxial case the diffusion barrier for free adsorbate particles becomes $E_{a,sub} \approx 0.37\,\mathrm{eV}$ recovering the value of B^0 in the lattice gas simulations of Sec. 4.2. Table 4.1 shows the corresponding values of E_{S} for the different potentials.

4.4.2 Equilibrium Simulations

In order to determine the influence of the misfit and binding energy between A and B particles on the resulting surface patterns canonical equilibrium simulations with a fully

potential	E_S [eV]
LJ	3.0
$\mathrm{M}_{5.0}$	3.0
$\mathrm{M}_{5.5}$	2.814
$\mathrm{M}_{6.0}$	2.7

Table 4.1: The substrate-substrate interaction E_S used in the Lennard-Jones (LJ) potential and the Morse (M_a) potential with parameter a.

covered substrate and fixed concentrations η_A, η_B of A and B particles ($\eta_\mathrm{A} + \eta_\mathrm{B} = 1$) were carried out [17]. In these simulations the substrate is prepared as a six-layer-thick crystal with 100×100 particles in each layer and fixed particle positions in the bottom layer. Periodic boundary conditions are applied in the x- and y-direction. Since for the considered range of misfits ε even at full coverage no dislocations are observed each adsorbate particle can be allocated at a distinct site of the 100×100 square lattice [17].

At the beginning of each simulation run the substrate is randomly covered with adsorbate particles with a given ratio $\eta_\mathrm{A}/\eta_\mathrm{B}$. Then the system is driven towards thermal equilibrium at temperature T by means of an algorithm similar to the one used for the lattice gas equilibrium simulations in Sec. 4.2.2. The main difference here is that the system is fully covered. Thus, in each Monte Carlo step an A particle at site i of the square lattice exchanges its binding site with a B particle at site j according to the rate $R_{i\to j} = \exp\left[(\Delta H_i - \Delta H_j) \,/\, (2k_BT)\right]$ where $\Delta H_x = H_x(A) - H_x(B)$ gives the energy difference of the system with site x occupied with an A or B particle. Details of the simulation algorithm are described in [17]. In order to avoid accumulation of artificial strain due to the local relaxation for the calculation of ΔH_x, the system is globally relaxed after a fixed number of simulation steps (here 5000) and all rates are re-evaluated. The system's total energy is registered after each global relaxation. All simulation runs are halted after 20 global relaxation events, i.e. after 10^5 elementary simulation steps.

Figure 4.21 shows simulation results for the cubic Lennard-Jones potential [Eqs. (4.7), (4.9)] for two different values of the misfit ε and strengths of the A–B interaction

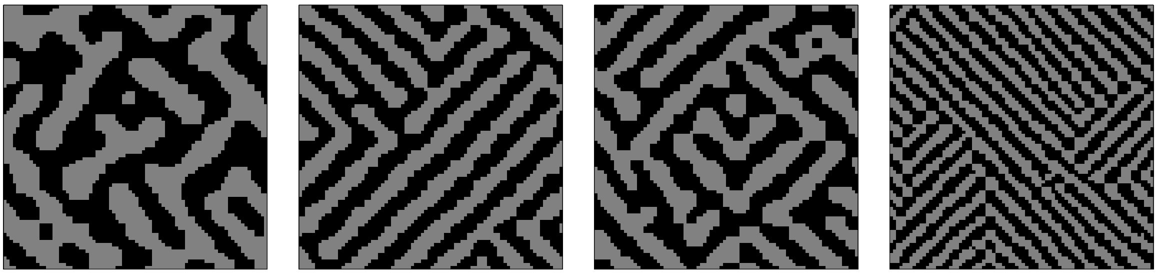

Figure 4.21: Snapshots for equilibrium simulations with the Lennard-Jones potential at $T = 250\,\mathrm{K}$. The results correspond to $E_\mathrm{AB} = 0.6E_\mathrm{A}$ with $\varepsilon = 4.5\%$, $\varepsilon = 5.5\%$, and to $E_\mathrm{AB} = 0.9E_\mathrm{A}$ with $\varepsilon = 4.5\%$, $\varepsilon = 5.5\%$ (from left to right). The particle concentrations are $\eta_\mathrm{A} = \eta_\mathrm{B} = 0.5$. The panels show 80×80 sections of the 100×100 system. The bigger B particles appear in light gray. Figures courtesy of F. Much [17].

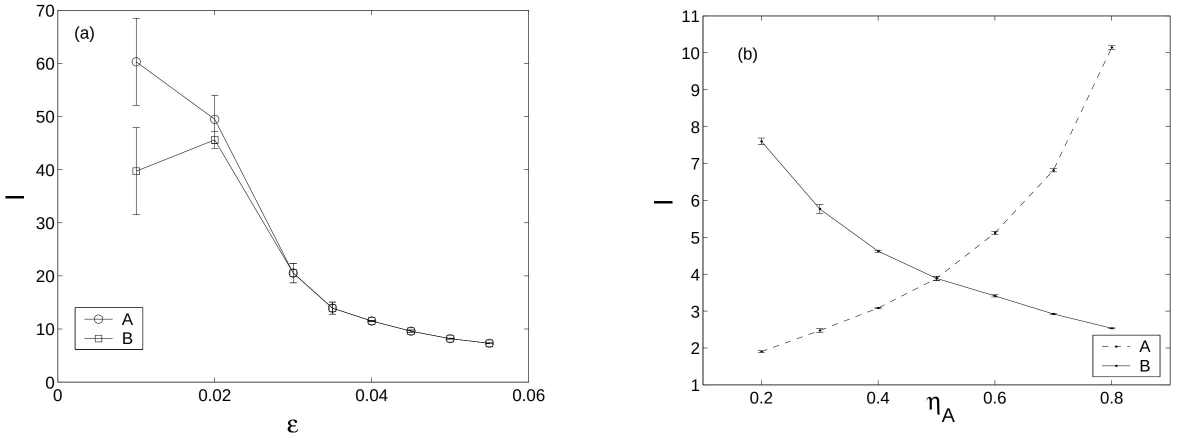

Figure 4.22: Equilibrium simulations with the Lennard-Jones potential at $T = 250\,\mathrm{K}$. (a) Misfit dependence of the stripe width for $E_{\mathrm{AB}} = 0.6E_{\mathrm{A}}$ and particle concentrations $\eta_{\mathrm{A}} = \eta_{\mathrm{B}} = 0.5$. Due to the onset of stripe formation along $\langle 10 \rangle$ the determination of the stripe width becomes inaccurate for misfits $\varepsilon \leq 0.01$. (b) Stripe width for $E_{\mathrm{AB}} = 0.9E_{\mathrm{A}}$, $\varepsilon = 5\%$ as a function of the A particle concentration η_{A} ($\eta_{\mathrm{B}} = 1 - \eta_{\mathrm{A}}$, consequently). Each value is obtained by averaging over three independent simulation runs. Errorbars are given by the standard deviation. Figures courtesy of F. Much [17].

E_{AB}. The particle concentrations are $\eta_{\mathrm{A}} = \eta_{\mathrm{B}} = 0.5$. For each parameter set a regular arrangement of alternating A and B stripes may be identified, which are oriented along the $\langle 11 \rangle$ directions, preferentially. As known from other atomistic models with size mismatch [88, 90] regular patterns may arise from the competition between binding energy of the particles and strain energy. As one can see in Fig. 4.21, with increasing E_{AB} and increasing ε the stripes become thinner and more regular in size and shape. For the case $E_{\mathrm{AB}} = E_{\mathrm{A}} = E_{\mathrm{B}}$ the system approaches a checkered state, i.e. a stripe width of one [17]. The alignment of the stripes along the $\langle 11 \rangle$ directions is due to the cubic symmetry of the potential: both particle types try to reach their preferred stripe width in each lattice direction (x and y). Note that the used cubic form of the potential [Eq. (4.9)] has only a weak interaction in the $\langle 11 \rangle$ direction [17].

Figure 4.22(a) shows the width l of A and B stripes for $E_{\mathrm{AB}} = 0.6\,E_{\mathrm{A}}$ in dependence on the misfit. Since the concentrations of A and B particles are equal the stripes have about the same width for both adsorbate types. For very small misfits the alignment of the stripes along $\langle 11 \rangle$ vanishes in favor of a $\langle 10 \rangle$ orientation which decreases the interfacial energy between A and B regions. This process is reflected in the large deviations of the stripe width at $\varepsilon = 0.01$ in Fig. 4.22(a). For $\varepsilon = 0$ one observes complete separation of A and B particles into two stripes of width $l = 50$ (half the system size) which wrap around the periodic boundaries. This is not surprising since in the homoepitaxial case the off-lattice model should behave like the lattice gas model from Sec. 4.1.1.

The situation changes completely for $\eta_{\mathrm{A}} \neq \eta_{\mathrm{B}}$. As Fig. 4.22(b) shows for $E_{\mathrm{AB}} =$

$0.9E_\mathrm{A}$ and $\varepsilon = 5\%$, the stripe width increases with increasing concentration of the particle type. It is noticeable that the bigger B particles form thinner stripes at high B concentration than the smaller A particles at high A concentration. This is due to the asymmetric pair-potential, which is steeper in compression than in tension and thus (compressed) B stripes are slightly more restricted in their width than A stripes.

Similar stripe patterns and stripe width dependencies are obtained for the $a = 6.0$ Morse potential which is steeper in both—compression and tension—than the Lennard-Jones potential. The main difference is that for the same misfit and $E_\mathrm{AB} \leq 0.6E_\mathrm{A}$ the stripes for the Morse potential are systematically thicker, whereas at higher values of E_AB the mean stripe width is nearly identical for both potentials at a given misfit. However, even at values $E_\mathrm{AB} \leq 0.6E_\mathrm{A}$ the deviations are small compared to the influence of the particle concentration on the stripe width [17].

In conclusion, the off-lattice simulations show that for the heteroepitaxial case ($\varepsilon > 0$) the equilibrium configurations are not characterized by complete separation of the two particle types as was the case in the lattice gas simulations. The combination of an attractive inter-species binding energy E_AB together with a non-vanishing misfit ε yields regular patterns of alternating stripes. This morphology is produced for a wide range of parameters and independently of the details of the interactions. The width of the stripes is controlled by the value of ε together with the binding energy.

4.4.3 Morphology under Non-Equilibrium Conditions

In the following we investigate how the system behaves under non-equilibrium growth conditions, and in particular how the grown structures compare to those observed in thermal equilibrium. To this end kinetic Monte Carlo simulations with the off-lattice model from Sec. 4.4.1 were done [17]. Like in the lattice gas simulations, random deposition and diffusion of adsorbate particles on the surface are included in these simulations whereas desorption and second layer nucleation are disregarded. Growth takes place on a 100×100 substrate of six layers height with fixed bottom layer and periodic boundary conditions in x- and y-direction. For all simulation runs the deposition rate for both types of particles is set to $5 \times 10^{-3}\,\mathrm{ML\,s^{-1}}$ resulting in an overall deposition rate of $R_d = 10^{-2}\,\mathrm{ML\,s^{-1}}$. The simulations are halted when half the substrate is covered with adsorbate particles. The diffusion of adatoms is described by thermally activated hopping processes between neighboring binding sites with Arrhenius rates $R = \nu_o \exp\left[-E_a/\left(k_B T\right)\right]$. Again, $\nu_o = 10^{12}\,\mathrm{s^{-1}}$ is used as common attempt frequency for all diffusion events. The activation energy E_a for a diffusion jump of a particle between two binding sites is given by $E_a = E_t - E_b$ where E_t and E_b are the potential energies of the particle at the transition state and the initial binding site, respectively. As mentioned in Sec. 4.4.2, in the misfit regime considered we do not have to worry about dislocations. Hence, E_b is readily determined by placing the particle on the perfect square lattice site and subsequent relaxation with respect to the precise, continuous particle positions [17]. The calculation of E_t implies searching for a first order saddle point in the potential energy surface (PES) generated by the superposition of all pair-interactions according to Eq. (4.9) [17].

The interaction strength between A and B particles is chosen to be

$$E_{\mathrm{AB}} = 0.6\, E_{\mathrm{A}}, \tag{4.13}$$

which—under equilibrium conditions—leads to the formation of rather thick stripes and for which the influence of the misfit should be clearly observable. Furthermore, on the basis of the equilibrium simulation results, one expects a noticeable dependence on the choice of the potential for this interaction strength. Note that $E_{\mathrm{A}} = E_{\mathrm{B}} = E_{\mathrm{S}}/6$ with the value of E_{S} given by Table 4.1 for the different potentials.

Note that this choice of the potential depths yields a higher barrier for edge diffusion than for diffusion on plain substrate. However, the edge diffusion barrier is still smaller than that for detachment from the edge. So particles attached to an island edge are more likely to diffuse there than to detach. This is of particular importance since we focus here on phenomena, where edge diffusion is supposed to have a strong impact, see the introduction of this chapter. Note also that for the cubic lattice [Eq. (4.9)] diagonal diffusion jumps can be neglected since they imply traversing a maximum in the PES [17].

The kinetic Monte Carlo simulations are carried out according to the standard scheme described in Sec. 1.5.2. Here, prior to the re-evaluation of the rates affected by a chosen event the system is locally relaxed around the location of this particular event. Similar to the equilibrium simulations, a relaxation of the entire system is performed after 4×10^5 steps in order to avoid strain accumulation.

We present now results on the influence of the misfit and the used potential at a temperature $T = 500\,\mathrm{K}$. Comparative simulation runs showed that under the same growth conditions both particle types form compact, rectangular islands if they are deposited alone onto the substrate. Additionally, one observes for the B particles with positive misfit that an island which becomes larger than a critical island size splits up into smaller islands [110]. This can be understood as relaxation of the accumulated compressive strain in the island. A similar effect has been observed experimentally for Cu/Ni(110) where copper islands undergo a shape transition when they exceed a critical island size [111].

In the case of co-deposition we observe a completely different situation. Figure 4.23 shows snapshots of simulation runs for the Morse potential [Eq. (4.10)] for various values of a and ε. These structures are exemplary for all simulation results: the B particles (shown in light gray) assemble into a few big clusters. With increasing misfit the branches of these clusters become thinner and of more uniform width. The A particles surround these branches without showing a similar shape. It is also seen from Fig. 4.23 that with increasing misfit the ramification of the structure as a whole increases. This is clearly related to the restricted width of the B stripes: a B particle rather attaches to the thin end of a stripe. This implies that thinner stripes of material B (light gray) grow outwards faster, leading to increasing ramification of the structure.

At a given misfit the B branches are the thinner the smaller the value of a in the Morse potential is. Consequently, at a given misfit the island ramification is more

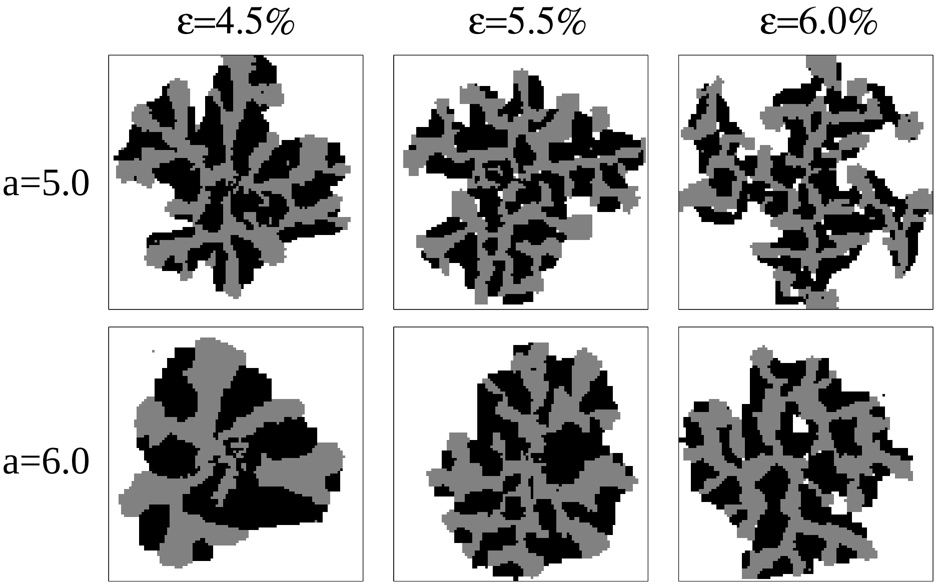

Figure 4.23: Exemplary surface configurations obtained by KMC simulations with the Morse potential [Eq. (4.10)] for different values of the parameter a and misfit ε. The bigger B particles are shown in light gray. Figures courtesy of F. Much [17].

pronounced for $a = 5.0$ than for $a = 6.0$. This is in agreement with the equilibrium simulations where a steeper potential yields thicker stripes.

In order to quantify the observations, for each connected cluster of B particles the ratio Λ between its perimeter length and its volume is calculated, in the same way as described in Sec. 4.2.4. Only the *backbone* of the structures is taken into account and smaller clusters (less than 700 particles) are neglected. Again, Λ gives a measure for the average thickness of the cluster, see Fig. 4.24(a).

In addition, the species-independent quantity Γ is measured, which is given by the number of particles in the system with less then 4 NN, divided by the square root of the total number of adatoms. Γ provides a measure for the length of the structure's perimeter and therefore the ramification, see Fig. 4.24(b). A single perfect quadratic island on the substrate corresponds to $\Gamma \approx 4$, whereas larger values of Γ indicate roughening of the island shape. The correlation between Λ and Γ is clearly observable for all used potentials: Λ increases with increasing misfit indicating thinner B clusters. Simultaneously the ramification increases. The formation of B branches of well-defined thickness is a common phenomenon for the used pair-potentials.

One might suspect that the observed ramification of the islands is merely due to temperature effects, i.e., the used temperature may be high enough for the formation of cubic clusters of a single species, but enlarged edge diffusion barriers in the case of mixed deposition might cause dendritic growth at the same temperature.

In order to investigate the temperature dependence of the island morphologies additional simulations were done for the Lennard-Jones potential with $\varepsilon = 5.0\%$ and the

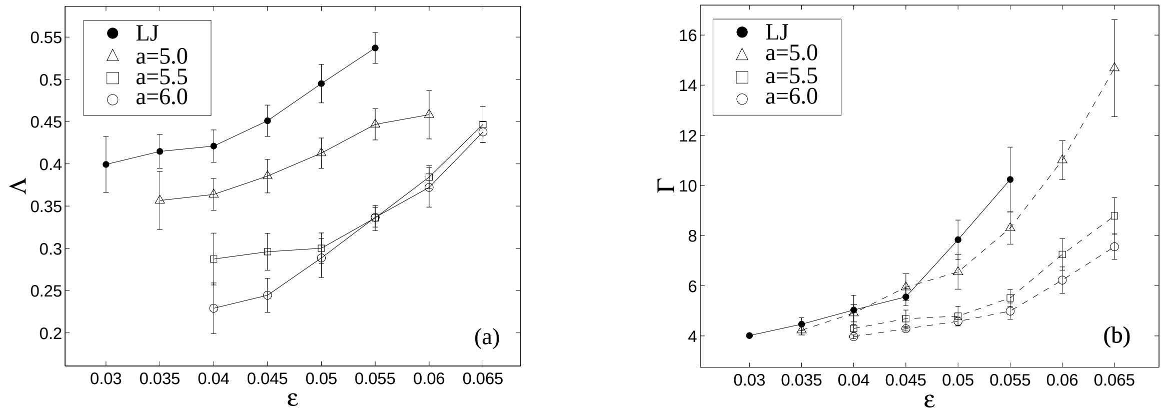

Figure 4.24: (a) Ratio Λ between perimeter particles and total number of particles in the big B clusters for the used potentials. (b) Number of perimeter particles divided by the square root of deposited particles Γ vs ε. Each value is obtained by averaging over ten independent simulation runs. The errorbars are given by the standard deviation. Figures courtesy of F. Much [17].

$a = 6.0$ Morse potential with $\varepsilon = 6.5\%$ for temperatures between 400 K and 550 K [17]. For the given parameters strongly ramified islands grow at $T = 500$ K. At low temperatures we observe multiple islands due to the reduced diffusion length. They exhibit frayed edges and rather thin and disordered B stripes. With increasing temperature the B stripes become wider and more regular in shape, the island edges become smoother. The observations are reflected in the temperature dependence of Λ and Γ as shown in Figs. 4.25(a) and (b). Note that the ramification Γ does not decrease monotonously with increasing temperature (as one might expect). For both potentials it exhibits a minimum at $T \approx 475$ K and then slowly increases with T for higher temperatures. This observation clearly rules out that the observed ramification is merely an artefact of the low growth temperature.

The enhanced mobility of the particles causes a more distinct separation of the two particle types, resulting in more regular B stripes. As Fig. 4.25(a) shows the width of the B stripes approaches a constant value for the high temperature region. Note that for high enough temperatures nearly all B clusters are aligned in the $\langle 11 \rangle$ directions in order to achieve the energetically most favorable arrangement of particles like in the equilibrium simulations (see [17]).

In conclusion, we have seen that in the off-lattice model the combination of both strain and binding energy effects leads to stripe formation *and*—under non-equilibrium growth conditions—to island ramification. However, it is not yet completely clear to what extent each of the two parts (strain and binding interaction) is responsible for the observed structures. For instance, the different sign of the misfits causes different diffusion barriers for A and B particles, respectively, the substrate diffusion of the bigger B particles being always faster than that of the smaller A particles [17,108]. Furthermore the barriers for edge diffusion are higher than the substrate diffusion barriers. This could

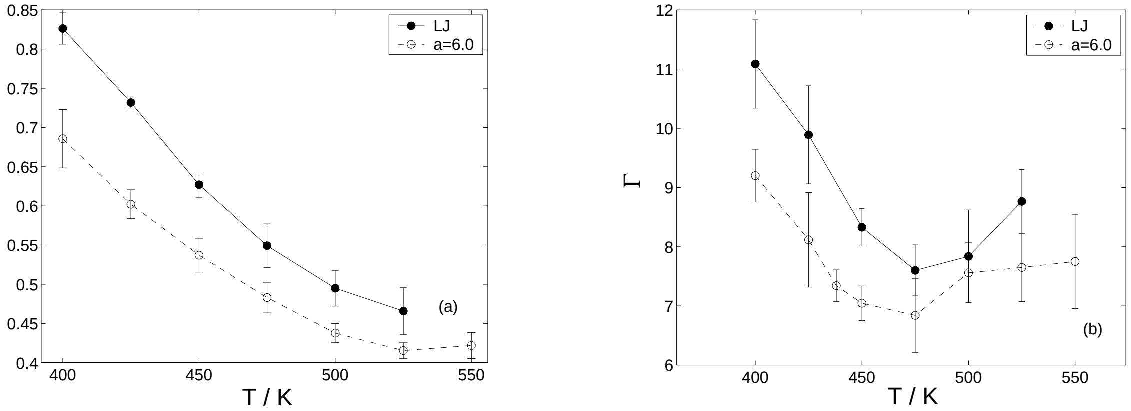

Figure 4.25: Temperature dependence of (a) Λ and (b) Γ for the Lennard-Jones potential with $\varepsilon = 5.0\%$ (filled circles) and the Morse $a = 6.0$ potential with $\varepsilon = 6.5\%$ (open circles). Figures courtesy of F. Much [17].

also give rise to a ramified island morphology.

4.5 Enhanced Lattice Gas

The lattice gas simulations of Sec. 4.2 showed that a weaker binding energy E^{AB} between A and B particles causes stripe formation. Similar to the off-lattice equilibrium simulations the stripe width can be controlled by adjusting E^{AB}. However, neither asymmetries between A and B clusters nor island ramification were observed under growth conditions (cf. Fig. 4.3) which is not surprising since A and B particles were treated in in a symmetric way apart from the weaker binding energy E^{AB} between them.

The symmetric parameter set certainly oversimplifies matters since A and B particles have different diffusion barriers which depend on the misfit, see above. In the following we will investigate whether the incorporation of such misfit dependent diffusion barriers suffices to reproduce the observed structures as, e.g., island ramification, within a lattice based method. Therefore we use the lattice gas model from Sec. 4.1.1 together with an enhanced parameter set which is fitted to reproduce the barriers of characteristic diffusion processes in the off-lattice model.

For the parameter fitting we extract the diffusion barriers of free A and B particles on the substrate as well as averaged values for edge diffusion and detachment for a *fixed* island size. These barriers are then used to determine E^{AA}, E^{BB} and E^{AB} as well as the B_i and B_f for the different diffusion processes [cf. Eq. (4.3)] in our lattice gas model. From the fitting procedure which is described in detail in App. A.3 we obtain six characteristic B's of type B^{XY}. Here X $\in$ {A,B} denotes the type of the diffusing particle at a given site and Y $\in$ {A,B,S} indicates whether the particle at this site is bound to an A or B particle or has no NN, see Fig. A.2(a). For example, B^{AB} corresponds to an A particle located at a step edge made up of B particles. The

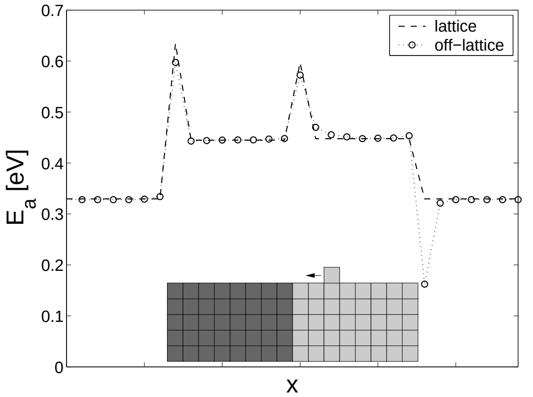

Figure 4.26: Barriers for diffusion of a B particle (light gray) from right to left nearby a small A–B cluster. The panel shows values obtained from the off-lattice model (open circles) using the Lennard-Jones potential and $\varepsilon = 4\%$, and the corresponding lattice gas approximation (dashed line).

barriers for particles with more than one NN are derived through averaging over all corresponding B^{XY}.

Figure 4.26 shows the diffusion barriers for a B particle diffusing from right to left nearby a small A–B cluster. Open circles denote off-lattice barriers for the Lennard-Jones potential with $\varepsilon = 4\%$ and the dashed line gives the lattice gas approximation with the fitted parameter set, cf. Table A.2. Note that although the lattice gas barrier for crossing the B–A interface is not a free parameter but derived from Eq. (4.3) it agrees well with the off-lattice barrier which is given by the potential energy difference of binding and transition state. Note also the reduced barrier for jumps towards the island in the off-lattice case which is due to the range of the potential. Furthermore, a slight modulation of the barrier at the step edge results from strain relaxation in the cluster [17]. These effects have to be neglected in the lattice gas model with NN interactions only.

Figure 4.27 shows a comparison between off-lattice simulations with the Lennard-Jones potential and lattice gas simulations with the fitted parameter set given by Table A.2. Similar results are obtained for the Morse potential. As expected, the islands for both models look very much alike in the case of zero misfit. However, for $\varepsilon = 5\%$ the results for both models seem to have little in common. In the case of the lattice

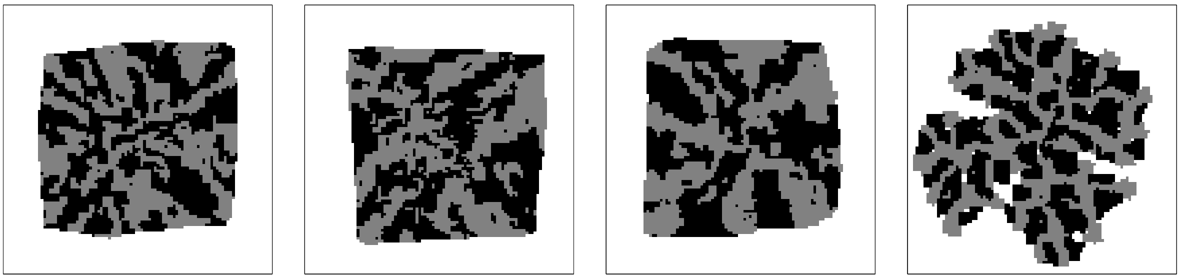

Figure 4.27: Comparison of snapshots for the enhanced lattice and the off-lattice model in the case of the Lennard-Jones potential. The panels show (from left to right) lattice/off-lattice results for $\varepsilon = 0$ and lattice/off-lattice results for $\varepsilon = 5\%$. Off-lattice results courtesy of F. Much [17].

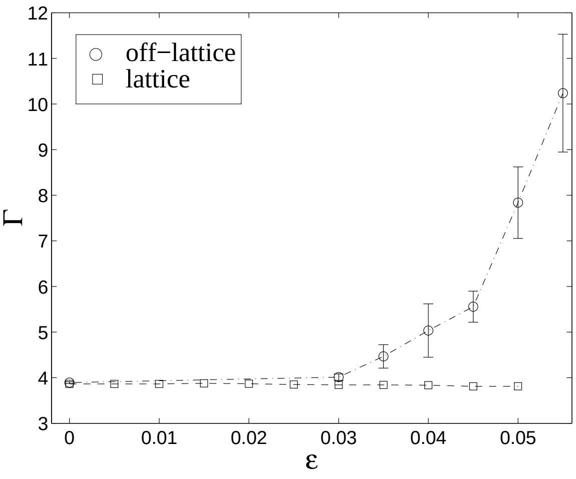

Figure 4.28: Island ramification for lattice and off-lattice simulations corresponding to the Lennard-Jones potential. Each value is obtained by averaging over ten independent simulation runs. For the off-lattice simulations errorbars are given by the standard deviation. For the lattice gas simulations errorbars are smaller than the symbol size.

model, the separation of A and B regions is more pronounced as for $\varepsilon = 0$ but neither size limitation of the stripes nor island ramification is observable here. To confirm this we have measured the ramification Γ for both lattice and off-lattice simulations results. Figure 4.28 shows Γ for various values of the misfit ε. For $\varepsilon = 0$ the islands are roughly quadratic in both types of simulations and thus the curves coincide at $\Gamma \approx 4$. With increasing misfit the islands in the off-lattice simulations become more and more ramified leading to a significant increase of Γ for $\varepsilon > 3\%$. For the lattice simulations though Γ remains constant, i.e. no ramification is observed.

Additional off-lattice simulations, where the reduced barrier for jumps towards an island (cf. Fig. 4.26) is eliminated *by hand* show that the resulting islands are less ramified whereas the width of the B branches remains unchanged [17]. The reduced island ramification can be traced back to a higher mobility of the particles: once a particle detaches from an island it has the same probability for jumps towards the island as away from it. The capturing of diffusing adatoms by islands is therefore less pronounced and the particles are more uniformly distributed around the island [17].

In conclusion, our examinations clearly demonstrate that species-dependent diffusion barriers at edges alone are not sufficient to explain the width restriction of the B branches or the ramification of the islands with increasing misfit. Our enhanced lattice gas model with fitted diffusion barriers thus lacks important features observed in both experiment and off-lattice simulations. The considerations in Sec. 4.2.6 suggest that the instability due the reduced corner rounding may eventually lead to some sort of island ramification in the lattice gas simulations as well. However, this effect will probably be much weaker and occur on much larger length scales than the ramification observed in the off-lattice simulations.

A more successful lattice based simulation would have to incorporate further, nonlocal effects. Diffusion barriers can depend on quite large neighborhoods in the off-lattice model. As an example, the above mentioned breaking up of pure B clusters at a characteristic size indicates that the misfit yields island size dependent barriers for attachment or detachment. Such effective long range interactions can be mediated through elastic deformation of the substrate, for instance. Clearly, an explicit incorporation of cluster size dependent barriers is beyond the scope of a simple lattice gas model and would destroy its conceptional advantages. Alternative routes, e.g. the evaluation of the strain energy for a given lattice configuration, have been suggested and used in the literature, see for instance [112].

4.6 Summary and Discussion

In this chapter we have studied a model ternary material system with adsorbates A and B on a substrate S of intermediate lattice spacing by complementary simulations with lattice gas and off-lattice growth models.

The systems display the formation of nanometer-scale stripes in a first layer of mixed A–B adsorbate in kinetic and equilibrium Monte Carlo simulations. The models incorporate the two main features that have been discussed as the driving force of stripe formation: (a) A weaker inter-species binding energy influences the barriers relevant for adatom diffusion along edges and results in kinetic segregation of the elements. (b) The presence of positive and negative misfit in the adsorbate favors an alternating arrangement of the species leading to strain relaxation in the system.

Simulations with a simple cubic lattice gas model which completely neglects the atomic size mismatch show that stripe patterns may arise under growth conditions as consequence of the weaker binding energy alone. The pattern formation is a purely kinetic effect as was demonstrated by equilibrium simulations where complete demixing occurs. The stripe width is found to increase with decreasing inter-species binding energy or with increasing temperature. For the temperature dependence, an Arrhenius law behavior is observed, consistent with experimental results for lateral phase separation in epitaxial layers of binary or ternary systems (e.g. [101, 102]).

In an off-lattice model, we allow for continuous particle positions and specify interactions by means of simple pair-potentials which favor a simple cubic lattice structure. Equilibrium simulations of a completely filled monolayer show that the adsorbate materials segregate and form nanoscale stripes, the width of which depending on the relative misfits and the inter-species binding energy.

Under non-equilibrium growth conditions we have observed the formation of highly ramified monolayer islands which consist of both adsorbate materials arranged in alternating stripes. A pronounced asymmetry is observed in the sense that the bigger B particles form a backbone of ramified branches, with the smaller A particles filling in the gaps.

Within the limitations of our lattice gas model we have tried to represent the features of the off-lattice model as faithful as possible by using an enhanced parameter set which has been fitted to characteristic diffusion barriers in the off-lattice model. However, it turns out that an explicit treatment of misfit effects is hardly possible within this framework: simulation results obtained with the enhanced lattice gas have shown that the model still lacks characteristic features observed both experimentally and in the off-lattice simulations. We conclude that indeed both above mentioned mechanisms, (a) and (b), are relevant and crucial for a satisfactory explanation of essential features observed in experiment as, e.g., island ramification.

On the one hand, kinetic segregation and stripe formation can be observed in a mixed system with zero misfits and sufficiently weak inter-species interaction under non-equilibrium growth conditions. However, close-to-equilibrium configurations display segregation into very large domains. No stable characteristic length is selected, whereas far-from-equilibrium growing islands lack the characteristic ramification and asymmetry of species.

On the other hand, a system with nonzero misfits but otherwise equivalent particle species would display a checkerboard like mixing of species without the formation of stripes in the whole range of considered misfits. In conclusion, only the interplay of kinetic effects and misfit induced strain effects can explain experimental observations as reported, e.g., by Hwang [83] qualitatively.

Our considerations show that a satisfactory treatment within the framework of a lattice gas model will only be possible, if it incorporates effectively long range elastic interactions. For instance, barriers for diffusion along an island edge should depend explicitly on the island size in a more faithful lattice gas picture.

Several interesting questions still remain: for example, the dependence of the adsorbate structure on the growth parameters should be studied in greater detail. In particular, it is an open question, whether the model displays the concentration dependent competition between alloying and dislocation formation in island growth, which was reported, for instance, in [82] for CoAg/Ru(0001).

In order to obtain a closer comparison with experiments the extension of the model to more realistic lattice geometries [e.g. fcc(111) surfaces] is currently under consideration [113]. In this context, a more realistic description of specific material systems would also require the use of more sophisticated many-body-potentials, like, e.g., tight-binding potentials [114]. This would clearly increase the computational effort significantly.

A case of particular interest is that of an anisotropic substrate which favors the self-assembly of aligned stripes [81]. Such nanostructures exhibit anomalous magnetic properties [115] which are expected to be relevant in the development of novel storage devices.

Finally, it will be highly interesting to study how the submonolayer structures persist in subsequent adsorbate layers (see e.g. [81]). To this end co-deposition of several monolayers of material has to be simulated within the growth model.

Appendix A

Supplementary Topics

A.1 Canonical Monte Carlo Simulations

In order to determine the equilibrium shape of adsorbate islands in the lattice gas model from Sec. 4.1.1 we carry out canonical Monte Carlo simulations with a fixed coverage of adsorbate particles. In each Monte Carlo step a particle jumps from its initial site to another site which is empty, that is the states of the two sites are exchanged and the number of particles remains the same. We apply a rejection-free non-local dynamics where the range of particle jumps is unlimited [11, 61]. This yields considerably faster equilibration than a local Kawasaki dynamics with nearest neighbor diffusion only [36]. For simplicity, we permit only jumps to a site where the binding energy of the particle is independent of the state of the initial site, that is we forbid jumps to nearest neighbor sites. Note that this does not violate the ergodicity condition as nearest neighbor exchanges can still be realized in appropriate sequences of the considered long distance processes. If now an A or B particle jumps from site i to site j, the energy difference between the final and the initial state is $\Delta H = \Delta H_j - \Delta H_i$, where ΔH_x is the energy difference of the system with site x occupied with a particle and empty. The rates

$$R_{i \to j} = \exp\left(\frac{\Delta H_i - \Delta H_j}{2k_B T}\right) \tag{A.1}$$

fulfill the detailed balance condition. Then, the probability for a jump from site i to site j factorizes, i.e.

$$p_{i \to j} = p_i^- \cdot p_j^+ \quad \text{where} \quad p_x^\pm = \frac{R_x^\pm}{\sum_x R_x^\pm}. \tag{A.2}$$

Here, R_x^+ and R_x^- denote the rates for deposition and removal of a particle at site x, respectively. $R_x^+ = \exp\left[-\Delta H_x/(2k_B T)\right]$ if site x is empty and zero otherwise. Conversely, $R_x^- = \exp\left[\Delta H_x/(2k_B T)\right]$ on occupied sites and zero on empty sites. This factorization property allows for proceeding in two steps: in the first step the site i from which the particle starts is selected with p_i^-, using a binary search tree. Then, the site j where the

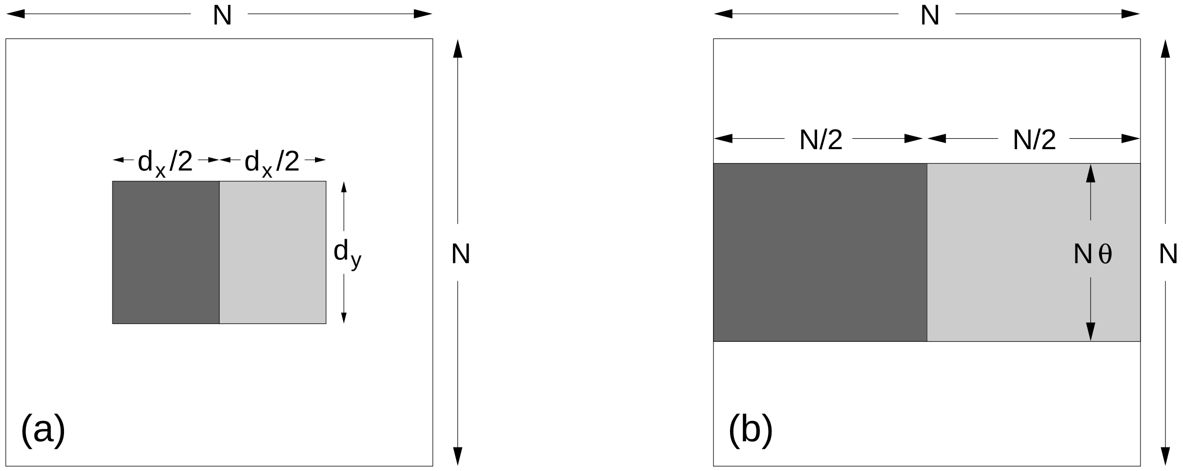

Figure A.1: Configurations which minimize the total energy of the $N \times N$ system with adsorbate coverage θ. (a) $\theta < \theta_c$: rectangular island with $d_x\, d_y = N^2\theta$ and d_x,d_y determined by Eqs. (A.4). (b) $\theta > \theta_c$: band of width $N\theta$ which wraps around the periodic boundary conditions. θ_c is given by Eq. (A.7).

particle is landing is selected with probability p_j^+ from a different search tree. If i and j are not nearest neighbors the particle is moved and the rates of all affected events are updated. Otherwise, the event is rejected and the system remains unchanged. Since the number of rejected events is small for large systems, the loss of speed can be neglected.

A.2 Minimum Energy Configurations

In Sec. 4.2.2 we determine the shape of mixed A–B adsorbate islands corresponding to the equilibrium configuration of the lattice gas model from Sec. 4.1.1 with binding energies E^0, E^{AB} and equal adsorbate concentrations. It is known from basic thermodynamics [36] that the equilibrium state of the system corresponds to the minimum of the free energy $F = E - TS$ at temperature T. Here E and S denote the internal energy and the entropy of the system, respectively. For $T = 0$ the entropic contribution vanishes and the minimum of F is given by the system configuration which minimizes E. For temperatures $T > 0$, but well below the melting temperature, the equilibrium configuration is expected to be similar to the minimum energy configuration.

In case of a vanishing binding energy E^{AB} between A and B particles the minimum energy configuration of the lattice gas model would be given by two square islands of equal size, one of which made up of only A particles, the other made up of B particles. For $E^{\mathrm{AB}} > 0$ we expect a merging of the two islands such that a rectangular island forms which consists of an A and B region with equal sizes and a straight interface inbetween, see Fig. A.1(a). Note however, that due to the periodic boundary conditions only for adsorbate coverages $\theta < \theta_c$ is the system's total energy minimized by such a rectangular island. For $\theta > \theta_c$ a band of width θN with two straight A–B interfaces which stretches across the whole system and wraps around the boundary conditions has a lower total energy, see Fig. A.1(b).

The value θ_c which separates the two regimes depends on the ratio $\alpha = E^{\mathrm{AB}}/E^0$ of the binding energies and may be obtained by the following considerations: Assume a rectangular island with side lengths d_x, d_y and $n = d_x\, d_y = N^2\theta$ particles made up of an A and B area with a straight interface of length d_y in-between, cf. Fig. A.1(a). The total binding energy per particle $\epsilon = E/n = E/(N^2\theta)$ as function of the interface length d_y is given by

$$\frac{\epsilon}{E^0} = -2 + (1-\alpha)\,\frac{d_y}{N^2\theta} + \left(\frac{d_y}{N^2\theta} + \frac{1}{d_y}\right). \tag{A.3}$$

The first term on the right-hand side of Eq. (A.3) corresponds to an infinite A or B island with two nearest neighbor bonds per particle whereas the second and third term mark the energy increase due to the A–B interface and the island boundary, respectively. Minimizing ϵ with respect to d_y yields

$$d_y = \frac{1}{\sqrt{2-\alpha}}\,N\sqrt{\theta} \quad \text{and} \quad d_x = \frac{N^2\theta}{d_y} = \sqrt{2-\alpha}\,N\sqrt{\theta} \tag{A.4}$$

for the side lengths and by combining Eqs. (A.4) and (A.3) we obtain

$$\frac{\epsilon}{E^0} = -2 + \frac{2\sqrt{2-\alpha}}{N\sqrt{\theta}} \tag{A.5}$$

for the minimum of the total binding energy per particle. Note that for a vanishing binding energy E^{AB} between A and B particles (i.e. $\alpha = 0$) one obtains $d_x = 2\,d_y$ from Eqs. (A.4) which implies that both A and B particles form square islands of equal size confirming the consideration from above. Conversely, $E^{\mathrm{AB}} = E^0$ ($\alpha = 1$) results in $d_x = d_y$: A and B particles are indistinguishable in this case and thus form a single square island.

A similar calculation for the band configuration [cf. Fig. A.1(b)] with length N and width $N\theta$ yields

$$\frac{\epsilon}{E^0} = -2 + \frac{2(1-\alpha)}{N} + \frac{1}{N\theta} \tag{A.6}$$

for the binding energy ϵ per particle. Again, the first term on the r.h.s. of Eq. (A.6) corresponds to an infinite island and the other two account for the A–B interface and the boundary. Note the factor of 2 in the second contribution which is due to the two A–B interfaces.

By equating Eqs. (A.5) and (A.6) we obtain the coverage θ_c where island and band configuration have the same energy as function of the ratio $\alpha = E^{\mathrm{AB}}/E^0$:

$$\theta_c = \frac{1-\sqrt{\alpha(2-\alpha)}}{2(1-\alpha)^2}. \tag{A.7}$$

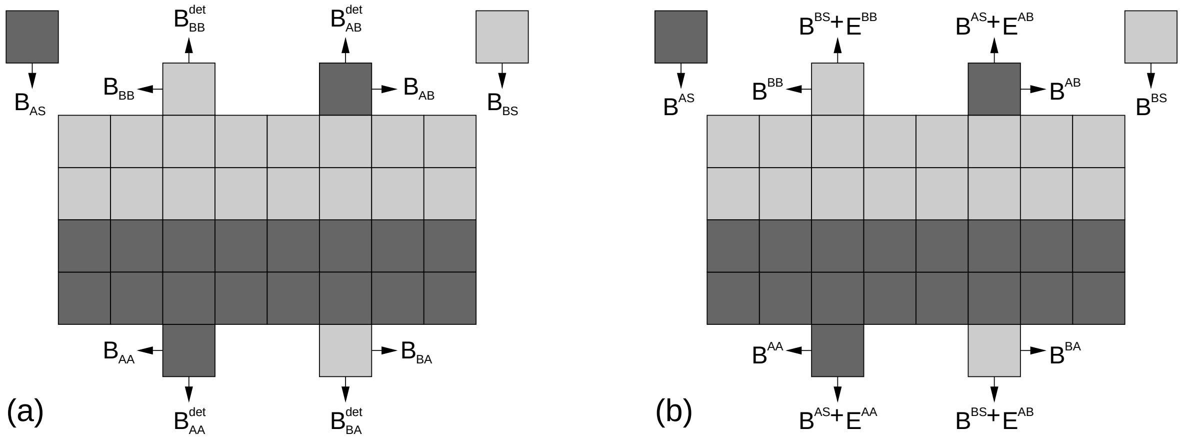

Figure A.2: Diffusion barriers for free adsorbate particles as well as for step edge diffusion and detachment from step edges. (a) Barriers obtained from the off-lattice model. (b) The same barriers expressed by the lattice gas parameters. A particles appear dark gray, B particles are light gray.

For $\theta < \theta_c$ the minimum energy state of the system is given by the island configuration [Fig. A.1(a)] with the energy derived from Eq. (A.5) whereas for $\theta > \theta_c$ the arrangement of the particles as band [Fig. A.1(b)] with the energy given by Eq. (A.6) is preferred. θ_c decreases monotonously from $\theta_c = 1/2$ at $\alpha = 0$ to $\theta_c = 1/4$ for $\alpha \to 1$.

A.3 Fitting of Lattice Gas Parameters

In Sec. 4.5 the parameters of the lattice gas model from Sec. 4.1.1 are fitted to the off-lattice energy barriers. Therefore, diffusion barriers for the following characteristic diffusion processes of A and B adsorbate particles are extracted from the off-lattice model as a function of the misfit ε [see Fig. A.2(a)]:

- diffusion of free A or B particles on the substrate $\to B_{\mathrm{AS}}, B_{\mathrm{BS}}$
- diffusion of an A (B) particle along a step edge made up of A (B) particles $\to B_{\mathrm{AA}}, B_{\mathrm{BB}}$
- diffusion of an A (B) particle along a step edge made up of B (A) particles $\to B_{\mathrm{AB}}, B_{\mathrm{BA}}$
- detachment of an A (B) particle from a step edge made up of A (B) particles $\to B_{\mathrm{AA}}^{det}, B_{\mathrm{BB}}^{det}$
- detachment of an A (B) particle from a step edge made up of B (A) particles $\to B_{\mathrm{AB}}^{det}, B_{\mathrm{BA}}^{det}$

The determination of B_{AS} and B_{BS} is done straightforwardly by putting a single A or B test particle on the (large enough) empty substrate S and calculating the energy difference between two adjacent transition and binding states. For the determination of $B_{\mathrm{XY}}, B_{\mathrm{XY}}^{det}$ (with X,Y $\in \{\mathrm{A}, \mathrm{B}\}$) a test particle of type X is put at a step edge of a square island which is made up of Y particles. The barriers for step edge diffusion and detachment are then again given by the energy difference between corresponding transition and binding states for all combinations of X and Y. Here, one has to consider that $B_{\mathrm{XY}}, B_{\mathrm{XY}}^{det}$ depend both on the island size and the position of the particle at the step edge, though not very strongly. Since for conceptual reasons these dependencies cannot easily be implemented in the lattice gas formulation anyway, $B_{\mathrm{XY}}, B_{\mathrm{XY}}^{det}$ are determined for a *fixed* island size of 20 × 20 lattice constants squared, averaging though over all positions of the test particle at the step edge.

The set of diffusion barriers determined from the off-lattice model is then mapped to the lattice gas model by adjusting the parameters E^{AA}, E^{BB}, E^{AB} for the nearest neighbor interactions as well as the $B's$ from Eq. (4.3), see Fig. A.2 as illustration. The assumption that the lattice gas barriers for free diffusion on the substrate shall coincide with those of the off-lattice model immediately yields

$$B^{\mathrm{AS}} = B_{\mathrm{AS}} \tag{A.8}$$

$$B^{\mathrm{BS}} = B_{\mathrm{BS}}. \tag{A.9}$$

Also, the barriers for step edge diffusion shall be the same in both models. Thus, one obtains four different $B's$ corresponding to the four characteristic configurations:

$$B^{\mathrm{AA}} = B_{\mathrm{AA}} \tag{A.10}$$

$$B^{\mathrm{BB}} = B_{\mathrm{BB}} \tag{A.11}$$

$$B^{\mathrm{AB}} = B_{\mathrm{AB}} \tag{A.12}$$

$$B^{\mathrm{BA}} = B_{\mathrm{BA}}. \tag{A.13}$$

Finally, as a consequence of the chosen lattice gas dynamics, each step edge detachment barrier from the off-lattice model has to be represented by a combination of *two* lattice gas parameters, see Fig. A.2. This leads to the following system of equations for the determination of E^{AA}, E^{BB} and E^{AB}:

$$B^{\mathrm{AS}} + E^{\mathrm{AA}} = B_{\mathrm{AA}}^{det} \tag{A.14}$$

$$B^{\mathrm{BS}} + E^{\mathrm{BB}} = B_{\mathrm{BB}}^{det} \tag{A.15}$$

$$B^{\mathrm{AS}} + E^{\mathrm{AB}} = B_{\mathrm{AB}}^{det} \tag{A.16}$$

$$B^{\mathrm{BS}} + E^{\mathrm{AB}} = B_{\mathrm{BA}}^{det} \tag{A.17}$$

which is overdetermined since there are only three different nearest neighbor interactions in the lattice gas model. This is due to the constraint that the total energy of the system given by Eq. (4.1) has to be well-defined. Thus, the same parameter E^{AB} for the interaction between A and B particles appears in Eqs. (A.16) and (A.17) instead of two independent parameters. Now, combining Eqs. (A.8),(A.9) with Eqs. (A.16), (A.17) yields

$$B^{det}_{\rm AB} - B^{det}_{\rm BA} = B_{\rm AS} - B_{\rm BS}. \tag{A.18}$$

If this condition is fulfilled an exact mapping between off-lattice barriers and lattice gas parameters is possible. Equation (A.18) holds for the homoepitaxial case ($\varepsilon = 0$) where from the symmetry of the off-lattice interactions [see Eq. (4.12)] follows $B_{\rm AS} = B_{\rm BS}$, $B^{det}_{\rm AB} = B^{det}_{\rm BA}$, and also $B_{\rm AA} = B_{\rm BB}$, $B_{\rm AB} = B_{\rm BA}$, $B^{det}_{\rm AA} = B^{det}_{\rm BB}$. Then the original set of ten equations reduces to a set of five equations which can be solved exactly, yielding

$$\begin{aligned}
B^{\rm AS} &= B^{\rm BS} = B_{\rm AS} && \text{(A.19)}\\
B^{\rm AA} &= B^{\rm BB} = B_{\rm AA} && \text{(A.20)}\\
B^{\rm AB} &= B^{\rm BA} = B_{\rm AB} && \text{(A.21)}\\
E^{\rm AA} &= E^{\rm BB} = B^{det}_{\rm AA} - B_{\rm AS} && \text{(A.22)}\\
E^{\rm AB} &= B^{det}_{\rm AB} - B_{\rm AS} && \text{(A.23)}
\end{aligned}$$

as values for the lattice gas parameters.

For the heteroepitaxial case ($\varepsilon > 0$) Eq. (A.18) in general does not hold. Consequently, at least one of the off-lattice barriers can only be approximated by the lattice gas parameters. Given the values of all other lattice gas parameters, $E^{\rm AB}$ can be chosen such that one of the two Eqs. (A.16), (A.17) is satisfied. Hence, one of the off-lattice barriers $B^{det}_{\rm AB}$, $B^{det}_{\rm BA}$ would be matched exactly in the lattice gas whereas the representation of the other one would be inaccurate. To avoid this asymmetric distribution of the error in the fitted parameter set, $E^{\rm AB}$ is chosen such that both $B^{det}_{\rm AB}$ and $B^{det}_{\rm BA}$ are approximated. The value of $E^{\rm AB}$ follows from the condition that the relative errors of the lattice gas representation with respect to the off-lattice values shall cancel each other, i.e.

$$\frac{(B^{\rm AS} + E^{\rm AB}) - B^{det}_{\rm AB}}{B^{det}_{\rm AB}} + \frac{(B^{\rm BS} + E^{\rm AB}) - B^{det}_{\rm BA}}{B^{det}_{\rm BA}} = 0. \tag{A.24}$$

Combining Eqs. (A.24) and (A.8),(A.9), one obtains

$$E^{\rm AB} = \frac{B^{det}_{\rm AB}\, B^{det}_{\rm BA}}{B^{det}_{\rm BA} - B^{det}_{\rm AB}} \left(2 - \frac{B_{\rm AS}}{B^{det}_{\rm AB}} - \frac{B_{\rm BS}}{B^{det}_{\rm BA}} \right) \tag{A.25}$$

for the interaction between A and B particles in the lattice gas. Note that the right-hand side in Eq. (A.25) is positive for all used potentials and values of the misfit. This is due to the fact that in the off-lattice model the barrier for detachment of a B particle from an A step edge is always larger than that for detachment of an A particle from a B step edge, thus leading to $B^{det}_{\rm BA} - B^{det}_{\rm AB} > 0$ in Eq. (A.25). Also the term in parentheses is positive since the barrier for detachment of a particle from a step edge is always larger than that for diffusion on the substrate.

With the value of $E^{\rm AB}$ given by Eq. (A.25) the deviations from the off-lattice detachment barriers $B^{det}_{\rm AB}$ and $B^{det}_{\rm BA}$ become less than 2.5% for all considered potentials

ε	B_{AS}	B_{BS}	B_{AA}	B_{BB}	B_{AB}	B_{BA}	B^{det}_{AA}	B^{det}_{BB}	B^{det}_{AB}	B^{det}_{BA}
0%	0.3771	0.3771	0.5705	0.5705	0.4949	0.4949	0.8783	0.8783	0.6756	0.6756
1%	0.3878	0.3659	0.5950	0.5413	0.5051	0.4834	0.8936	0.8579	0.6837	0.6662
2%	0.3983	0.3542	0.6146	0.5094	0.5138	0.4711	0.9038	0.8342	0.6905	0.6561
3%	0.4083	0.3421	0.6302	0.4775	0.5213	0.4582	0.9093	0.8100	0.6959	0.6456
4%	0.4179	0.3295	0.6430	0.4476	0.5279	0.4448	0.9106	0.7871	0.6999	0.6346
5%	0.4271	0.3167	0.6538	0.4215	0.5347	0.4310	0.9080	0.7646	0.7023	0.6232

Table A.1: Diffusion barriers [eV] in the off-lattice model [see Fig. A.2(a)] with the Lennard-Jones potential for various values of the misfit ε.

ε	B^{AS}	B^{BS}	B^{AA}	B^{BB}	B^{AB}	B^{BA}	E^{AA}	E^{BB}	E^{AB}	$\lvert\delta\rvert$
0%	0.3771	0.3771	0.5705	0.5705	0.4949	0.4949	0.5012	0.5012	0.2985	0
1%	0.3878	0.3659	0.5950	0.5413	0.5051	0.4834	0.5058	0.4920	0.2981	0.33%
2%	0.3983	0.3542	0.6146	0.5094	0.5138	0.4711	0.5055	0.4800	0.2972	0.72%
3%	0.4083	0.3421	0.6302	0.4775	0.5213	0.4582	0.5010	0.4679	0.2958	1.19%
4%	0.4179	0.3295	0.6430	0.4476	0.5279	0.4448	0.4927	0.4576	0.2941	1.73%
5%	0.4271	0.3167	0.6538	0.4215	0.5347	0.4310	0.4809	0.4479	0.2918	2.36%

Table A.2: Lattice gas parameters [eV] [see Fig. A.2(b)] fitted to the off-lattice diffusion barriers from Table A.1 according to Eqs. (A.8)–(A.17) and (A.25). Note that the barriers for substrate diffusion and diffusion along step edges coincide with the corresponding off-lattice values from Table A.1. The last column contains the absolute value of the relative errors obtained by the approximation of the off-lattice detachment barriers B^{det}_{AB} and B^{det}_{BA}.

and values of the misfit ε. Table A.1 shows the diffusion barriers as determined from the off-lattice model for the Lennard-Jones potential and several values of ε. The corresponding lattice gas parameters which are obtained by Eqs. (A.8)–(A.17) and (A.25) are listed in Table A.2. The last column contains the absolute value of the relative errors obtained by the approximation of the off-lattice barriers B^{det}_{AB} and B^{det}_{BA}, cf. Eq. (A.24).

Bibliography

[1] M. A. Herman, W. Richter, and H. Sitter. *Epitaxy – Physical Principles and Technical Implementation.* Springer, Berlin, 2004.

[2] M. A. Herman and H. Sitter. *Molecular Beam Epitaxy – Fundamentals and Current Status.* Springer, Berlin, 2nd edition, 1996.

[3] A. Pimpinelli and J. Villain. *Physics of Crystal Growth.* Cambridge University Press, Cambridge, 1998.

[4] A.-L. Barabási and H. E. Stanley. *Fractal Concepts in Surface Growth.* Cambridge University Press, Cambridge, 1995.

[5] M. Kotrla. Numerical simulations in the theory of crystal growth. *Comput. Phys. Commun.* 97, 82–100, 1996.

[6] T. Michely and J. Krug. *Islands, Mounds and Atoms – Patterns and Processes in Crystal Growth Far from Equilibrium.* Springer, Berlin, 2004.

[7] A. Zangwill. *Physics at Surfaces.* Cambridge University Press, Cambridge, 1988.

[8] J. W. Evans, D. E. Sanders, P. A. Thiel, and A. E. DePristo. Low-temperature epitaxial growth of thin metal films. *Phys. Rev. B* 41 (8), 5410–5413, 1990.

[9] J. W. Evans. Factors mediating smoothness in epitaxial thin-film growth. *Phys. Rev. B* 43 (5), 3897–3905, 1991.

[10] S. Schinzer. *Kinetic Monte-Carlo Simulations of Crystal Surfaces: Applications to II-VI Semiconductors.* Ph.D. thesis, Bayerische Julius-Maximilians-Universität Würzburg, Würzburg, 1999.

[11] M. Ahr. *Surface properties of epitaxially grown crystals.* Ph.D. thesis, Bayerische Julius-Maximilians-Universität Würzburg, Würzburg, 2002.

[12] C. M. Gilmore and J. A. Sprague. Molecular-dynamics simulation of the energetic deposition of Ag thin films. *Phys. Rev. B* 44 (16), 8950–8957, 1991.

[13] D. E. Sanders, D. M. Halstead, and A. E. DePristo. Metal/metal homoepitaxy on fcc(111) and fcc(001) surfaces: Deposition and scattering from small islands. *J. Vac. Sci. Technol. A* 10 (4), 1986–1992, 1992.

[14] Y. Yue, Y. K. Ho, and Z. Y. Pan. Molecular-dynamics study of transient-diffusion mechanisms in low-temperature epitaxial growth. *Phys. Rev. B* 57 (11), 6685–6688, 1998.

[15] J. D. Wrigley and G. Ehrlich. Surface Diffusion by an Atomic Exchange Mechanism. *Phys. Rev. Lett.* 44 (10), 661–663, 1980.

[16] P. Politi, G. Grenet, A. Marty, A. Ponchet, and J. Villain. Instabilities in crystal growth by atomic or molecular beams. *Physics Reports* 324 (5–6), 271–405, 2000.

[17] F. Much. *Modeling and Simulation of Strained Heteroepitaxial Growth.* Ph.D. thesis, Bayerische Julius-Maximilians-Universität Würzburg, Würzburg, 2003.

[18] M. Biehl. Lattice gas models and Kinetic Monte Carlo simulations of epitaxial growth. In *International Series in Numerical Mathematics.* Birkhäuser, 2004.

[19] R. M. Dreizler and E. K. U. Gross. *Density Functional Theory – An Approach to the Quantum Many-Body Problem.* Springer, Berlin, 1990.

[20] C. H. Park and D. J. Chadi. First-principles study of the atomic reconstructions of ZnSe(100) surfaces. *Phys. Rev. B* 49 (23), 16467–16473, 1994.

[21] A. García and J. E. Northrup. First-principles study of Zn- and Se-stabilized ZnSe(100) surface reconstructions. *J. Vac. Sci. Technol. B* 12 (4), 2678–2683, 1994.

[22] S. Gundel, A. Fleszar, W. Faschinger, and W. Hanke. Atomic and electronic structure of the CdTe(001) surface: LDA and GW calculations. *Phys. Rev. B* 59 (23), 15261–15269, 1999.

[23] S. Gundel. *ab initio simulations of II-VI semiconductors: bulk properties, surfaces, and implications for crystal growth.* Ph.D. thesis, Bayerische Julius-Maximilians-Universität Würzburg, Würzburg, 2001.

[24] G. Brocks, P. J. Kelly, and R. Car. Binding and Diffusion of a Si Adatom on the Si(100) Surface. *Phys. Rev. Lett.* 66 (13), 1729–1732, 1991.

[25] P. Kratzer and M. Scheffler. Reaction-Limited Island Nucleation in Molecular Beam Epitaxy of Compound Semiconductors. *Phys. Rev. Lett.* 88 (3), 036102, 2002.

[26] P. Kratzer, E. Penev, and M. Scheffler. First-principles studies of kinetics in epitaxial growth of III-V semiconductors. *Appl. Phys. A* 75, 79–88, 2002.

[27] P. Kratzer and M. Scheffler. Surface Knowledge Toward a Predictive Theory of Materials. *Comp. Sci. Eng.* 3 (6), 16–25, 2001.

[28] C. Ratsch and M. Scheffler. Density-functional theory calculations of hopping rates of surface diffusion. *Phys. Rev. B* 58 (19), 13163–13166, 1998.

[29] P. Hänggi, P. Talkner, and M. Borkovec. Reaction-rate theory: fifty years after Kramers. *Rev. Mod. Phys.* 62 (2), 251–341, 1990.

[30] F. Grosse, W. Barvosa-Carter, J. Zinck, M. Wheeler, and M. F. Gyure. Arsenic Flux Dependence of Island Nucleation on InAs(001). *Phys. Rev. Lett.* 89 (11), 116102, 2002.

[31] D. C. Rapaport. *The Art of Molecular Dynamics Simulation.* Cambridge University Press, Cambridge, 2nd edition, 2004.

[32] R. Car and M. Parrinello. Unified Approach for Molecular Dynamics and Density-Functional Theory. *Phys. Rev. Lett.* 55 (22), 2471–2474, 1985.

[33] O. S. Trushin, M. Kotrla, and F. Máca. Energy barriers on stepped Ir/Ir(111) surfaces: a molecular statics calculation. *Surf. Sci.* 389, 55–65, 1997.

[34] J. Tersoff. New empirical approach for the structure and energy of covalent systems. *Phys. Rev. B* 37 (12), 6991–7000, 1988.

[35] F. H. Stillinger and T. A. Weber. Computer simulation of local order in condensed phases of silicon. *Phys. Rev. B* 31 (8), 5262–5271, 1985.

[36] M. E. J. Newman and G. T. Barkema. *Monte Carlo Methods in Statistical Physics.* Oxford University Press, Oxford, 1999.

[37] A. F. Voter, F. Montalenti, and T. C. Germann. Extending the Time Scale in Atomistic Simulation of Materials. *Annu. Rev. Mater. Res.* 32, 321–346, 2002.

[38] F. Jensen. *Introduction to Computational Chemistry.* Wiley, New York, 1999.

[39] N. W. Ashcroft and N. D. Mermin. *Solid State Physics.* Saunders College Publishing, Philadelphia, 1976.

[40] C. Busse, C. Polop, M. Müller, K. Albe, U. Linke, and T. Michely. Stacking-Fault Nucleation on Ir(111). *Phys. Rev. Lett.* 91 (5), 056103, 2003.

[41] M. Biehl, W. Kinzel, and S. Schinzer. A simple model of epitaxial growth. *Europhys. Lett.* 41 (4), 443–448, 1998.

[42] S. Schinzer, M. Kinne, M. Biehl, and W. Kinzel. The role of step edge diffusion in epitaxial crystal growth. *Surf. Sci.* 439, 191–198, 1999.

[43] M. Ahr, M. Biehl, M. Kinne, and W. Kinzel. The influence of the crystal lattice on coarsening in unstable epitaxial growth. *Surf. Sci.* 465, 339–346, 2000.

[44] F. Máca, M. Kotrla, and O. S. Trushin. Energy barriers for diffusion on stepped Rh(111) surfaces. *Surf. Sci.* 454–456, 579–583, 2000.

[45] G. T. Barkema and N. Mousseau. Event-Based Relaxation of Continuous Disordered Systems. *Phys. Rev. Lett.* 77 (21), 4358–4361, 1996.

[46] K. A. Fichthorn and W. H. Weinberg. Theoretical foundations of dynamical Monte Carlo simulations. *J. Chem. Phys.* 95 (2), 1090–1096, 1991.

[47] M. Muñoz, M. Tamargo, J. K. Furdyna, and H. Luo (editors). *Proceedings of the 11th International Conference on II-VI Compounds*, volume 1 of *Phys. Status Solidi C.* 2004.

[48] T. Litz, H. J. Lugauer, F. Fischer, U. Zehnder, U. Lunz, T. Gerhard, H. Ress, A. Waag, and G. Landwehr. Molecular beam epitaxy of Be-related II–VI compounds. *Mater. Sci. Eng. B* 43, 83–87, 1997.

[49] C. Barglik-Chory, D. Buchold, M. Schmitt, W. Kiefer, C. Heske, C. Kumpf, O. Fuchs, L. Weinhardt, A. Stahl, E. Umbach, M. Lentze, J. Geurts, and G. Müller. Synthesis, structure and spectroscopic characterization of water-soluble CdS nanoparticles. *Chem. Phys. Lett.* 379, 443–451, 2003.

[50] R. Fiederling, M. Keim, G. Reuscher, W. Ossau, G. Schmidt, A. Waag, and L. W. Molenkamp. Injection and detection of a spin-polarized current in a light-emitting diode. *Nature* 402, 787–790, 1999.

[51] S. Tatarenko, B. Daudin, D. Brun, V. H. Etgens, and M. B. Veron. Cd and Te desorption from (001), (111)B, and (110) CdTe surfaces. *Phys. Rev. B* 50 (24), 18479–18488, 1994.

[52] B. Daudin, S. Tatarenko, and D. Brun-Le Cunff. Surface stoichiometry determination using reflection high-energy electron diffraction and atomic-layer epitaxy: The case of ZnTe(100). *Phys. Rev. B* 52 (11), 7822–7825, 1995.

[53] H. Neureiter, S. Spranger, M. Schneider, U. Winkler, M. Sokolowski, and E. Umbach. Reconstruction, morphology, and stoichiometry of CdTe(001) and $Cd_{0.96}Zn_{0.04}Te(001)$ surfaces. *Surf. Sci.* 388, 186–200, 1997.

[54] H. Neureiter, S. Tatarenko, S. Spranger, and M. Sokolowski. Domain wall formation at the $c(2 \times 2)$-(2×1) phase transition of the CdTe(001) surface. *Phys. Rev. B* 62 (4), 2542–2545, 2000.

[55] B. Daudin, D. Brun-Le Cunff, and S. Tatarenko. Stoichiometry determination of the Te-rich (100) CdTe and (100) ZnTe surfaces. *Surf. Sci.* 352–354, 99–104, 1996.

[56] D. Wolfframm, D. A. Evans, D. I. Westwood, and J. Riley. A detailed surface phase diagram for ZnSe MBE growth and ZnSe/GaAs(001) interface studies. *J. Cryst. Growth* 216, 119–126, 2000.

[57] J. Cibert and S. Tatarenko. The Surface Structure of a II-VI Compound: CdTe. *Defect and Diffusion Forum* 150–151, 1–34, 1997.

[58] K. Saminadayar, S. Tatarenko, K. Kheng, V. Huard, and D. Martrou. Growth and doping of Te-based II–VI layers and quantum structures by molecular beam epitaxy. In H. S. Nalwa (editor), *Handbook of Advanced Electronic and Photonic Materials and Devices*, volume 1, chapter 1, pages 1–80. Academic Press, London, 2001.

[59] S. Gundel. *ab initio–Simulationen von II-VI-Halbleitern und ZnSe-Oberflächen.* Master's thesis, Bayerische Julius-Maximilians-Universität Würzburg, Würzburg, 1997.

[60] M. Biehl, M. Ahr, W. Kinzel, M. Sokolowski, and T. Volkmann. A lattice gas model of II-VI(001) semiconductor surfaces. *Europhys. Lett.* 53 (2), 169–175, 2001.

[61] M. Ahr and M. Biehl. Flat (001) surfaces of II–VI semiconductors: a lattice gas model. *Surf. Sci.* 505, 124–136, 2002.

[62] L. Seehofer, G. Falkenberg, R. L. Johnson, V. H. Etgens, S. Tatarenko, D. Brun, and B. Daudin. Scanning tunneling microscopy study of CdTe(001). *Appl. Phys. Lett.* 67 (12), 1680–1682, 1995.

[63] M. D. Pashley. Electron counting model and its application to island structures on molecular-beam epitaxy grown GaAs(001) and ZnSe(001). *Phys. Rev. B* 40 (15), 10481–10487, 1989.

[64] L. Seehofer, V. H. Etgens, G. Falkenberg, M. B. Veron, D. Brun, B. Daudin, S. Tatarenko, and R. L. Johnson. Atomic motion on the CdTe(001) surface observed with scanning tunneling microscopy. *Surf. Sci.* 347, L55–L60, 1996.

[65] D. Martrou, J. Eymery, and N. Magnea. Equilibrium Shape of Steps and Islands on Polar II-VI Semiconductors Surfaces. *Phys. Rev. Lett.* 83 (12), 2366–2369, 1999.

[66] W. Faschinger and H. Sitter. Atomic-layer epitaxy of (100) CdTe on GaAs substrates. *J. Cryst. Growth* 99, 566–571, 1990.

[67] J. M. Hartmann, G. Feuillet, M. Charleux, and H. Mariette. Atomic layer epitaxy of CdTe and MnTe. *J. Appl. Phys.* 79 (6), 3035–3041, 1996.

[68] S. A. Barnett and A. Rockett. Monte Carlo simulations of Si(001) growth and reconstruction during molecular beam epitaxy. *Surf. Sci.* 198, 133–150, 1988.

[69] A. Rockett. The influence of surface structure on growth of Si(001)2×1 from the vapor phase. *Surf. Sci.* 227, 208–218, 1990.

[70] M. Ahr, M. Biehl, and T. Volkmann. Modeling (001) surfaces of II–VI semiconductors. *Comput. Phys. Commun.* 147, 107–110, 2002.

[71] M. Itoh. Atomic-scale homoepitaxial growth simulations of reconstructed III–VI surfaces. *Prog. Surf. Sci.* 66, 53–153, 2001.

[72] H. Neureiter, S. Schinzer, W. Kinzel, S. Tatarenko, and M. Sokolowski. Simultaneous layer-by-layer and step-flow sublimation on the CdTe(001) surface derived from a diffraction analysis. *Phys. Rev. B* 61 (8), 5408–5415, 2000.

[73] T. Suntola and J. Hyvarinen. Atomic layer epitaxy. *Annu. Rev. Mater. Sci.* 15, 177–195, 1985.

[74] A. Ohtake, T. Hanada, T. Yasuda, K. Arai, and T. Yao. Structure and composition of the ZnSe(001) surface during atomic-layer epitaxy. *Phys. Rev. B* 60 (11), 8326–8332, 1999.

[75] W. Faschinger, F. Hauzenberger, P. Juza, H. Sitter, A. Pesek, H. Zajicek, and K. Lischka. Short period CdTe–ZnTe and CdTe–MnTe superlattices. *Mater. Sci. Eng. B* 16, 79–82, 1993.

[76] M. Ahr and M. Biehl. Modelling sublimation and atomic layer epitaxy in the presence of competing surface reconstructions. *Surf. Sci.* 488, L553–L560, 2001.

[77] F. Grosse and M. F. Gyure. Ab initio based modeling of III-V semiconductor surfaces: Thermodynamic equilibrium and growth kinetics on atomic scales. *Phys. Rev. B* 66, 075320, 2002.

[78] C. G. Morgan, P. Kratzer, and M. Scheffler. Arsenic Dimer Dynamics during MBE Growth: Theoretical Evidence for a Novel Chemisorption State of As_2 Molecules on GaAs Surfaces. *Phys. Rev. Lett.* 82 (24), 4886–4889, 1999.

[79] B. Joyce, P. Kelires, A. Naumovets, and D. D. Vvedensky (editors). *Quantum Dots: Fundamentals, Applications, and Frontiers.* Kluwer, in press.

[80] R. Plass, N. C. Bartelt, and G. L. Kellogg. Dynamic observations of nanoscale self-assembly on solid surfaces. *J. Phys.: Condens. Matter* 14, 4227–4240, 2002.

[81] E. D. Tober, R. F. C. Farrow, R. F. Marks, G. Witte, K. Kalki, and D. D. Chambliss. Self-Assembled Lateral Multilayers from Thin Film Alloys of Immiscible Metals. *Phys. Rev. Lett.* 81 (9), 1897–1900, 1998.

[82] G. E. Thayer, V. Ozoliņš, A. K. Schmid, N. C. Bartelt, M. Asta, J. J. Hoyt, S. Chiang, and R. Q. Hwang. Role of Stress in Thin Film Alloy Thermodynamics: Competition between Alloying and Dislocation Formation. *Phys. Rev. Lett.* 86 (4), 660–663, 2001.

[83] R. Q. Hwang. Chemically Induced Step Edge Diffusion Barriers: Dendritic Growth in 2D Alloys. *Phys. Rev. Lett.* 76 (25), 4757–4760, 1996.

[84] R. Q. Hwang and M. C. Bartelt. Scanning Tunneling Microscopy Studies of Metal on Metal Epitaxy. *Chem. Rev.* 97, 1063–1082, 1997.

[85] G. E. Thayer, N. C. Bartelt, V. Ozoliņš, A. K. Schmid, S. Chiang, and R. Q. Hwang. Linking Surface Stress to Surface Structure: Measurement of Atomic Strain in a Surface Alloy using Scanning Tunneling Microscopy. *Phys. Rev. Lett.* 89 (3), 036101, 2002.

[86] B. Sadigh, M. Asta, V. Ozoliņš, A. K. Schmid, N. C. Bartelt, A. A. Quong, and R. Q. Hwang. Short-Range Order and Phase Stability of Surface Alloys: PdAu on Ru(0001). *Phys. Rev. Lett.* 83 (7), 1379–1382, 1999.

[87] J. L. Stevens and R. Q. Hwang. Strain Stabilized Alloying of Immiscible Metals in Thin Films. *Phys. Rev. Lett.* 74 (11), 2078–2081, 1995.

[88] J. Tersoff. Surface-Confined Alloy Formation in Immiscible Systems. *Phys. Rev. Lett.* 74 (3), 434–437, 1995.

[89] I. Daruka and J. C. Hamilton. A two-component Frenkel–Kontorowa model for surface alloy formation. *J. Phys.: Condens. Matter* 15, 1827–1836, 2003.

[90] B. D. Krack, V. Ozoliņš, M. Asta, and I. Daruka. "Devil's Staircases" in Bulk-Immiscible Ultrathin Alloy Films. *Phys. Rev. Lett.* 88 (18), 186101, 2002.

[91] F. Máca, M. Kotrla, and O. S. Trushin. Energy barriers for diffusion on stepped Pt(111) surface. *Vacuum* 54, 113–117, 1999.

[92] G. S. Bales and A. Zangwill. Morphological instability of a terrace edge during step-flow growth. *Phys. Rev. B* 41 (9), 5500–5508, 1990.

[93] M. V. R. Murty and B. H. Cooper. Instability in Molecular Beam Epitaxy due to Fast Edge Diffusion and Corner Diffusion Barriers. *Phys. Rev. Lett.* 83 (2), 352–355, 1999.

[94] H. Brune, H. Röder, K. Bromann, K. Kern, J. Jacobsen, P. Stoltze, K. Jacobsen, and J. Nørskov. Anisotropic corner diffusion as origin for dendritic growth on hexagonal substrates. *Surf. Sci.* 349, L115–L122, 1996.

[95] A. Bogicevic, J. Strömquist, and B. I. Lundqvist. Low-Symmetry Diffusion Barriers in Homoepitaxial Growth of Al(111). *Phys. Rev. Lett.* 81 (3), 637–640, 1998.

[96] S. Ovesson, A. Bogicevic, and B. I. Lundqvist. Origin of Compact Triangular Islands in Metal-on-Metal Growth. *Phys. Rev. Lett.* 83 (13), 2608–2611, 1999.

[97] T.-Y. Fu and T. T. Tsong. Determination of atomic potential energy around step corner sites of the Ir(111) surface. *Phys. Rev. B* 61 (7), 4511–4513, 2000.

[98] L. Hansen, P. Stoltze, K. W. Jacobsen, and J. K. Nørskov. Self-diffusion on copper surfaces. *Phys. Rev. B* 44 (12), 6523–6526, 1991.

[99] J. G. Amar. Mechanisms of mound coarsening in unstable epitaxial growth. *Phys. Rev. B* 60 (16), R11317–R11320, 1999.

[100] Y. Saito. Two-Dimensional Nucleation with Edge and Corner Diffusions. *J. Phys. Soc. Jpn.* 72 (8), 2008–2014, 2003.

[101] C. D. Adams, M. Atzmon, Y.-T. Cheng, and D. J. Srolovitz. Phase separation during co-deposition of Al–Ge thin films. *J. Mater. Res.* 7 (3), 653–666, 1991.

[102] T. L. McDevitt, S. Mahajan, D. E. Laughlin, W. A. Bonner, and V. G. Keramidas. Two-dimensional phase separation in $\mathrm{In}_{1-x}\mathrm{Ga}_x\mathrm{As}_y\mathrm{P}_{1-y}$ epitaxial layers. *Phys. Rev. B* 45 (12), 6614–6622, 1992.

[103] A. Schindler. *Theoretical aspects of growth on one and two dimensional strained crystal surfaces.* Ph.D. thesis, Gerhard-Mercator-Universität Duisburg, Duisburg, 1999.

[104] M. Biehl, F. Much, and C. Vey. Off-lattice Kinetic Monte Carlo simulations of strained heteroepitaxial growth. In *International Series in Numerical Mathematics.* Birkhäuser, 2004.

[105] F. Much, M. Ahr, M. Biehl, and W. Kinzel. Kinetic Monte Carlo simulations of dislocations in heteroepitaxial growth. *Europhys. Lett.* 56 (6), 791–796, 2001.

[106] F. Much, M. Ahr, M. Biehl, and W. Kinzel. A Kinetic Monte Carlo method for the simulation of heteroepitaxial growth. *Comput. Phys. Commun.* 147, 226–229, 2002.

[107] F. Much and M. Biehl. Simulation of wetting-layer and island formation in heteroepitaxial growth. *Europhys. Lett.* 63 (1), 14–20, 2003.

[108] M. Schroeder and D. E. Wolf. Diffusion on strained surfaces. *Surf. Sci.* 375, 129–140, 1997.

[109] P. M. Morse. Diatomic Molecules According to the Wave Mechanics. II. Vibrational Levels. *Phys. Rev.* 34, 57–64, 1929.

[110] F. Much. Private communication.

[111] B. Müller, L. Nedelmann, B. Fischer, H. Brune, J. V. Barth, and K. Kern. Island Shape Transition in Heteroepitaxial Metal Growth on Square Lattices. *Phys. Rev. Lett.* 80 (12), 2642–2645, 1998.

[112] M. Meixner, E. Schöll, V. A. Shchukin, and D. Bimberg. Self-Assembled Quantum Dots: Crossover from Kinetically Controlled to Thermodynamically Limited Growth. *Phys. Rev. Lett.* 87 (23), 236101, 2001.

[113] S. Weber. Ph.D. thesis, Bayerische Julius-Maximilians-Universität Würzburg, Würzburg, 2006.

[114] F. Cleri and V. Rosato. Tight-binding potentials for transition metals and alloys. *Phys. Rev. B* 48 (1), 22–33, 1993.

[115] E. D. Tober, R. F. Marks, D. D. Chambliss, K. P. Roche, M. F. Toney, A. J. Kellock, and R. F. C. Farrow. Magnetoresistance of self-assembled lateral multilayers. *Appl. Phys. Lett.* 77 (17), 2728–2730, 2000.

Danksagungen

Allen, die zum Gelingen dieser Arbeit beigetragen haben, möchte ich an dieser Stelle meinen herzlichen Dank aussprechen. Insbesondere bedanke ich mich bei

- Priv. Doz. Dr. Michael Biehl für die ausgezeichnete Betreuung der Arbeit, vielfache Anregungen und Ideen sowie die stete Bereitschaft auf Fragen einzugehen.
- Prof. Dr. Wolfgang Kinzel für die Möglichkeit, die vorliegende Arbeit an seinem Lehrstuhl anzufertigen.
- Dr. Martin Ahr, Priv. Doz. Dr. Michael Biehl, Dr. Miroslav Kotrla und Dr. Florian Much für die fruchtbare Zusammenarbeit, deren Ergebnisse wir gemeinsam veröffentlicht haben.
- Dr. Miroslav Kotrla für die Gastfreundschaft an der Tschechischen Akademie der Wissenschaften in Prag.
- Dr. Florian Much für das gründliche Korrekturlesen dieser Arbeit.
- Dr. Martin Ahr, Ansgar Freking, Dr. Florian Much und Andreas Ruttor für viele Anregungen und Diskussionen.
- den Systembetreuern Ansgar Freking, Andreas Klein, Georg Reents, Andreas Ruttor, Andreas Vetter und Alexander Wagner für den störungsfreien Betrieb des Computersystems.
- allen Mitgliedern unserer Arbeitsgruppe für das freundliche und kreative Arbeitsklima.
- der Deutschen Forschungsgemeinschaft für die Finanzierung dieser Arbeit durch den Sonderforschungsbereich 410.
- meiner Familie und meiner Freundin Dagmar für die Unterstützung während des Studiums und der Anfertigungszeit dieser Arbeit.

Lebenslauf

Angaben zur Person

Thorsten Volkmann
geboren am 21. 10. 1974 in Göttingen
Staatsangehörigkeit: deutsch
Familienstand: ledig

Schulbildung

08/1981–06/1987	Grundschule und Orientierungsstufe, Gaußschule Bremerhaven
08/1987–06/1991	Gymnasiale Mittelstufe, Lessingschule Bremerhaven
08/1991–06/1994	Gymnasiale Oberstufe, Schulzentrum Geschwister-Scholl Bremerhaven Allgemeine Hochschulreife

Zivildienst

08/1994–10/1995	Krankenpflege in der Klinik für Radio-Onkologie des Zentralkrankenhaus Reinkenheide, Bremerhaven

Studium

11/1995–07/1998	Studium der Physik an der Bayerischen Julius-Maximilians-Universität Würzburg
10/1997	Vordiplom im Fach Physik
08/1998–05/1999	Studium der Physik an der University of Texas at Austin
06/1999–12/2000	Fortsetzung des Studiums der Physik an der Universität Würzburg
03/2000–12/2000	Diplomarbeit „Anisotropie-Effekte an Halbleiteroberflächen“ am Institut für Theoretische Physik und Astrophysik der Universität Würzburg Betreuer: Priv. Doz. Dr. Michael Biehl
02/2001	Verleihung des Diploms im Fach Physik

Promotion

01/2001–12/2004	Wissenschaftlicher Mitarbeiter am Institut für Theoretische Physik und Astrophysik der Universität Würzburg
08/2003	Forschungsaufenthalt bei Dr. Miroslav Kotrla an der Tschechischen Akademie der Wissenschaften in Prag